11-13-2013

Investigation of Water Droplet Dynamics in PEM Cell Gas Channels

Preethi Gopalan

R·I·T

INVESTIGATION OF WATER DROPLET DYNAMICS IN PEM FUEL CELL GAS CHANNELS

by

Preethi Gopalan

A dissertation submitted in partial fulfillment of the requirements
for the degree of Doctorate of Philosophy in Microsystems Engineering

Microsystems Engineering Program
Kate Gleason College of Engineering

Rochester Institute of Technology
Rochester, New York
November 13, 2013

INVESTIGATION OF WATER DROPLET DYNAMICS IN PEM FUEL CELL GAS CHANNELS

by

Preethi Gopalan

Committee Approval:

We, the undersigned committee members, certify that we have advised and/or supervised the candidate on the work described in this dissertation. We further certify that we have reviewed the dissertation manuscript and approve it in partial fulfillment of the requirements of the degree of Doctor of Philosophy in Microsystems Engineering.

Dr. Satish G. Kandlikar Date
James E. Gleason Professor, Mechanical Engineering (Advisor)

Dr. Steven J. Weinstein Date
Department Head, Biomedical and Chemical Engineering

Dr. Denis Cormier Date
Earl W. Brinkman Professor, Industrial and Systems Engineering

Dr. Steven W. Day Date
Professor, Mechanical Engineering

Certified by:

Dr. Bruce W. Smith Date
Director, Microsystems Engineering Program

Dr. Harvey J. Palmer Date
Dean, Kate Gleason College of Engineering

ABSTRACT

Kate Gleason College of Engineering
Rochester Institute of Technology

Degree: Doctor of Philosophy **Program:** Microsystems Engineering

Authors Name: Preethi Gopalan

Advisors Name: Satish G. Kandlikar

Dissertation Title: Investigation of Water Droplet Dynamics in PEM Fuel Cell Gas Channels

Water management in Proton Exchange Membrane Fuel Cell (PEMFC) has remained one of the most important issues that need to be addressed before its commercialization in automotive applications. Accumulation of water on the gas diffusion layer (GDL) surface in a PEMFC introduces a barrier for transport of reactant gases through the GDL to the catalyst layer. Despite the fact that the channel geometry is one of the key design parameters of a fluidic system, very limited research is available to study the effect of microchannel geometry on the two–phase flow structure. In this study, the droplet–wall dynamics and two–phase pressure drop across the water droplet present in a typical PEMFC channel, were examined in auto–competitive gas channel designs (0.4 x 0.7 mm channel cross section). The liquid water flow pattern inside the gas channel was analyzed for different air velocities. Experimental data was analyzed using the Concus–Finn condition to determine the wettability characteristics in the corner region. It was confirmed that the channel angle along with the air velocity and the channel material influences the water distribution and holdup within the channel. Dynamic contact angle emerged as an important parameter in controlling the droplet–wall interaction. Experiments were also performed to understand how the inlet location of the liquid droplet on the GDL surface affects the droplet dynamic behavior in the system. It was found that droplets emerging near the channel wall or under the land lead to corner filling of the channel. Improvements in the channel design has been proposed based on the artificial channel roughness created to act as capillary grooves to transport the liquid water away from the land area. For droplets emerging near the center of the channel, beside the filling and no-filling behavior reported in the literature, a new droplet jumping behavior was observed. As droplets grew and touched the sidewalls, they jumped off to the sidewall leaving the whole GDL exposed for gases to diffuse to the catalyst layer. A theoretical model was developed and a criterion was proposed to predict the droplet jumping behavior in the gas channel. A theoretical force balance model was proposed to predict the pressure force and air velocity required to remove the droplet from the channel to avoid complete channel blockage. The overall goal of this work was to identify the gas channel configuration that provides efficient water removal with a lower pressure drop in the system efficiency while meeting the US Department of Energy's specifications for a PEMFC for automotive application.

ACKNOWLEDGMENTS

First and foremost, I would like to express my gratitude to my advisor, Dr. Satish G. Kandlikar for providing me with this wonderful opportunity to conduct research and for his generous support, guidance and constant encouragement throughout my graduate studies at RIT. I thank him for providing me the wonderful opportunity of being a part of Thermal Analysis, Microfluidics and Fuel Cell Laboratory (TAμFL), which actually became my second home in the due course. His wholehearted, enthusiastic personality along with interminable patience has made it an immense pleasure for me to conduct research with him. His distinguished ability to envision complex problems from an elegant and intuitive touch has shaped the way I approach any problem.

I am very much grateful to Dr. Steven Weinstein, Dr. Denis Cormier, Dr. Steven W. Day and Professor Bruce W. Smith for being a part of my dissertation committee and for their generous support in sharing their ideas and all sorts of facility resources for the maximum good of my research. I would also like to thank Lisa Zimmerman for taking care of all my administrative responsibilities and keeping me on track with my progress.

I would like to acknowledge the support received from the US Department of Energy under contract number DE-EE0000470. I would also like to thank Jon Owejan and Jeffery Gagliardo of the General Motors Electrochemical Energy Research Laboratory for providing guidance and materials for the research. This work could not have been completed without their support.

I would like to acknowledge the staff at the Mechanical Engineering Machine Shop for their unrestrained help and willingness to teach me every time I go there. In particular, I would like to thank Mr. Dave Hathaway, Mr. Robert Kraynik and Mr. Jan Maneti for their knowledge, willingness and readiness to help on almost everything related to microfabrications at any time. I would also like to thank Sean O'Brien and John Nash at Semiconductor and Microsystems Fabrication Laboratory (SMFL) for training and helping me with the tools. I also want to acknowledge the staff at the Mechanical Engineering Department Office for all their support and willingness to go an extra mile to help me every time I go there for anything.

I am indebted to former group members especially Dr. Guangsheng Zhang, Mr. Cody Rath and Dr. Carlos Rubio for guiding me in conducting simulations, experiments and taking measurements. I am extremely grateful to all my lab members especially Rupak Banerjee, Mihir Shah, Zhonghua Yao, Ankit Kalani and Chinmay Patil for the

support and help they provided me throughout my doctoral studies. I would like to thank Mustafa Koz, Valentina Mejia Jeet Mehta and for all the technical discussions we had and for making my stay in Rochester a very pleasant and treasured one. I also want to express my greatest gratitude to Dr. Madusudanan Sathianarayanan for his valuable support and encouragement, which made my doctoral studies enjoyable and successful. I would also like to thank Tarun Mudgal, Amanpreet Kaur and Mihir Bohra who were the ones who really made my journey throughout my PhD the most memorable one. I cherish all the memories during the innumerable fun trips and late night chats we had together. I wish all of them the best of luck all the way with their studies, careers and personal lives.

Finally, I would like to acknowledge and thank the source of life and my eternal support – my family. I would like to dedicate this work to my parents, Mr. Vedagiri Gopalan and Mrs. Vidya Gopalan, and my sister, Nanditha Gopalan. Without their love, dedication and sacrifice I would not be where I am now. They constantly motivated and supported me from the beginning, and cherished my growth and achievements, especially while I was away from home. Thank you for everything.

TABLE OF CONTENTS

LIST OF FIGURES

LIST OF TABLES

NOMENCLATURE

English

P_{Wheel}	Power delivered to the wheel of the vehicle
P_{Cell}	Power generated by the fuel cell stack
$P_{Auxiliary}$	Power required for powering the auxiliary units
r	Roughness factor
f_i	Area fraction of material 'i'
B_o	Bond number
D	Diameter of a pipe
g	Gravity
Re	Reynolds number
v	Air velocity
i	Current density
S	Scaling factor
H	Height of the grooves
W	Width of the grooves
R_{C_1}	Maximum radius of the droplet before touching the sidewall

R_{C_2}	Maximum radius of the droplet before touching the base while hanging from the sidewall
R_2	Actual droplet radius as it hangs from the sidewall
a	Droplet emergence location from the channel corner
x	Distance from the channel corner where droplet contacts the sidewall
V_1	Volume of the droplet before jumping to the sidewall
V_2	Volume of the droplet right after it jumps to the sidewall
G_o	Gibbs free energy when droplet sits on the base
$E_{Gravity}$	Energy required by the droplet to move against gravity (Potential energy)
ΔP	Pressure drop
M	Mach number
F_D	Drag force
F_S	Surface tension force
A	Area of the droplet
C_D	Drag coefficient
$2d$	Width of the contact line of the droplet
K	Rectification factor

RH	Relative humidity
n	Number of moles of a molecule
F	Faraday's constant
Q_g	Water generation rate
MW	Molecular weight of a substance
$\dot{Q}$	Airflow rate
U	Uncertainty
L_w	Land width
C_w	Channel width
L_C	Channel length

Greek

σ	Surface tension
θ	Equilibrium contact angle
$\Delta\theta$	Contact angle hysteresis
2α	Channel open angle or corner angle
ρ	Fluid density

Subscripts

L	Liquid phase of a droplet
S	Solid phase of substrate
V	Vapor/gas phase of a substrate
LV	Liquid-vapor interface
SV	Solid-vapor interface
SL	Solid-liquid interface
B	Channel Base
W	Channel sidewall
A	Advancing
R	Receding
r	Rough surface
c	Composite surface
C	Channel

Abbreviations

OECD	Organization for economic co–operation and development
PEMFC	Proton exchange membrane fuel cell
IC	Internal combustion
NMR	Nuclear magnetic resonance
MRI	Magnetic resonance imaging
GDL	Gas diffusion layer
SGL	Sigracet
MRC	Mitsubishi rayon corporation carbon paper
TGP	Toray paper (Teflon coated carbon fiber)
GDM	Gas diffusion media
CL	Contact line
CF	Carbon fiber
MEA	Membrane electrode assembly
MPL	Microporous layer
CB	Cassie–Baxter
CW	Cassie–Wenzel transition
NIST	National institute of standards and technology

PTFE	Polytetrafluoroethylene
CFD	Computational fluid dynamics
CLSM	Confocal laser scanning microscope
LCL	Lower contact line
ICL	Inner contact line
UCL	Upper contact line
IDCA	Instantaneous dynamic contact angle
CFL	Concus–Finn limit

Chapter 1 Introduction

According to the Organization for Economic Co–operation and Development (OECD), an international organization of 34 countries, 30% of the carbon dioxide emissions are mainly due to the transportation sector [1, 2]. Figure 1.1 shows an image of an IC engine car and the pollution caused by it. Transportation is one of the major sectors, which uses large amount of fossil fuel according to their 2010 annual report [3]. In addition, internal combustion (IC) engines, which are the main workhorse for vehicles, have an overall efficiency of only about 18% – 20% [4]. Different losses associated with an IC engine vehicle are shown in Figure 1.2. Hence, depletion of the fossil fuels and ever increasing environmental pollution have driven the need for developing alternative renewable energy sources in the transportation sector [5]. For example, solar, wind, and hydrogen (H_2) are being considered as serious alternatives to conventional energy sources.

Figure 1.1: Environmental pollution caused by an IC engine vehicle during operation [6]

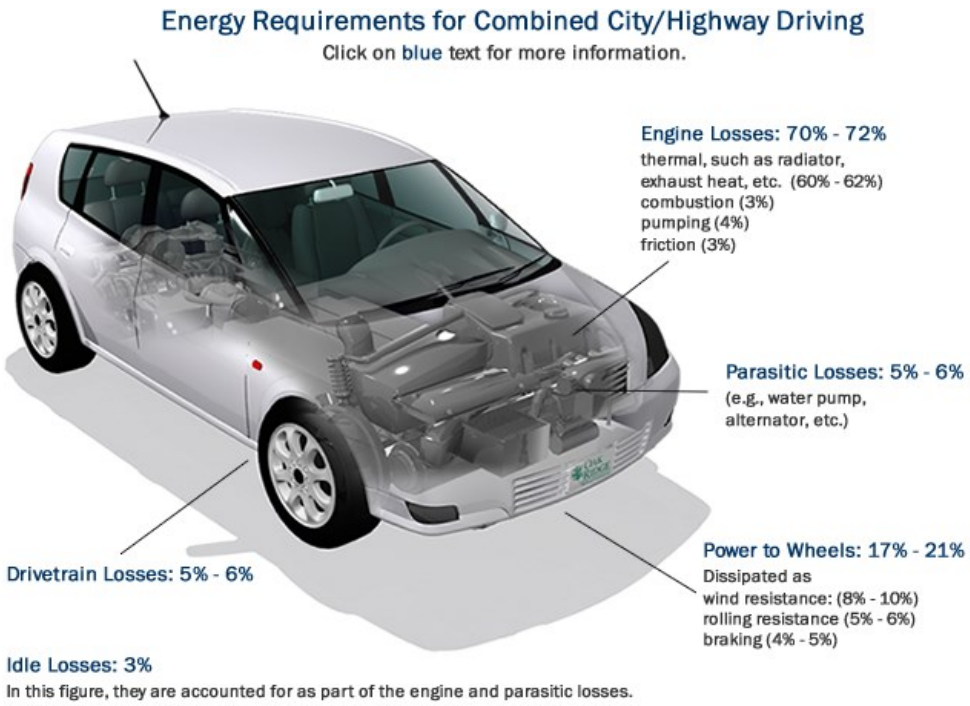

Figure 1.2: Different types of energy losses associated with the drive cycle of a vehicle with IC engine [5].

From the several choices available, hydrogen is an attractive option because it can be produced from various other forms of energy, including nuclear, solar, and wind [1]. Though several forms of hydrogen-powered technologies exist and have been well researched, the most preferred approach is fuel cells [7, 8]. The process by which fuel cells create energy is the reverse reaction of electrolysis, which combines hydrogen and oxygen in the presence of a catalyst. Among various types of fuel cells that exist, the Proton Exchange Membrane Fuel Cell (PEMFC) appears to be the most promising candidate for powering commercial and private automobiles due to its simplicity in design and its low temperature operating condition [9].

On the other hand, compared to IC engines and batteries, PEMFCs are significantly more expensive. Commercialization of PEMFCs requires reduction in cost and increase in power density through engineering optimization, which is dependent on the understanding of the PEMFC operation. It is seen that General Motors, one of the leading automobile company, is trying to optimize the PEMFC stack configuration that can go in the automobile in the place of IC engine over the course of time (Figure 1.3).

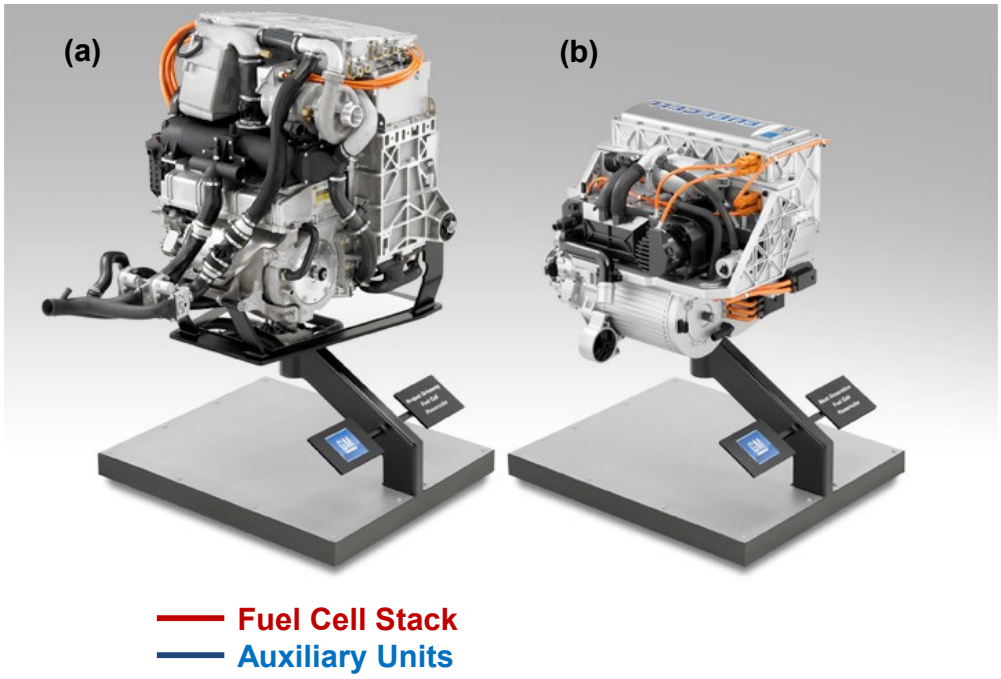

Figure 1.3: (a) PEM fuel cell stack and auxiliary unit configuration of previous generation and (b) an improved fuel cell system that still needs further improvement in terms of size and efficiency. Image courtesy to General Motors.

The maximum theoretical energy efficiency of a fuel cell is 80%, operating at low power density and using pure hydrogen and oxygen as the reactants [10], whereas the tank–to–wheel efficiency of a fuel cell vehicle is less than 60% at low loads [11]. The energy delivered to the wheel of a fuel cell vehicle is calculated using Eq. 1.1

$$P_{Wheel} = P_{Cell} - P_{Auxiliary} \quad [1.1]$$

where, P_{Wheel}— Power delivered to the wheel of the vehicle

P_{Cell}— Power generated by the fuel cell stack

$P_{Auxiliary}$ — Power required for powering the auxiliary units

A fuel cell auxiliary unit is comprised of pumps, blowers, controllers, and compressors. Therefore, to design fuel cells with high efficiency, the internal processes must be optimized. Some of the key parameters include the fluid flow distribution, the local current density, reduction in the excess air required to remove the liquid water in the gas channel and so forth. To get into more detail, one needs to first understand the basic functioning of the PEMFC.

1.1 Proton Exchange Membrane Fuel Cells

A fuel cell in general consists of three main parts – anode, cathode and membrane – as shown in Figure 1.4. The anode, where the electrons are produced, is mainly responsible for the oxidation reaction of the hydrogen molecules and release of protons and electrons. The humidified hydrogen gas (H_2 and water vapor) enters the anode channel and the hydrogen diffuses through the porous anode Gas Diffusion Layer (GDL) to the catalyst layer where it splits into protons and electrons. At the anode catalyst layer, the following electrochemical reaction takes place:

$$H_2 \rightarrow 2H^+ + 2e^- \quad [1.2]$$

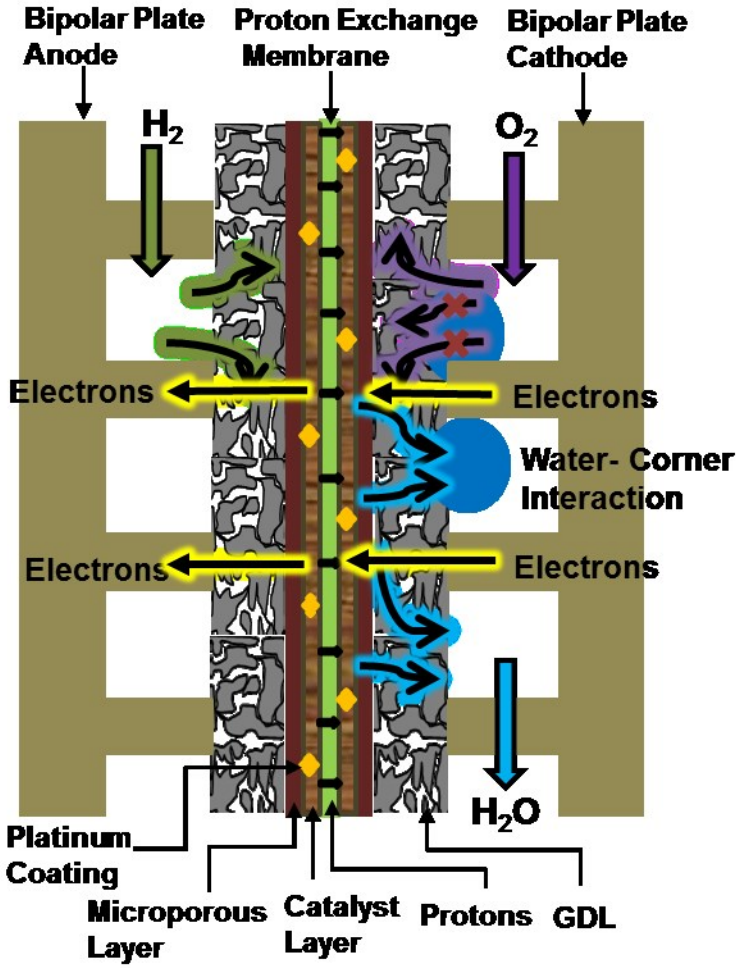

Figure 1.4: Schematic of a proton exchange membrane fuel cell (PEMFC). Adapted from [12].

The membrane located between the cathode and the anode allows only proton conduction to occur, while the electrons are blocked from crossing over, and hence it is called a Proton Exchange Membrane (PEM). The protons move through the membrane to the cathode side while the electrons move through the outer circuit to generate power. The cathode end also has a bipolar plate that has gas channels etched on it for effective distribution of oxygen molecules over the catalyst surface. At this end, humidified air enters the cathode channel and the oxygen diffuses through the porous cathode GDL to

the reaction sites (cathode catalyst layer). A reduction reaction takes place at the cathode catalyst layer producing water and heat as a byproduct that needs to be removed. Eq. 1.3 gives the reduction reaction.

$$\frac{1}{2}O_2 + 2H^+ + 2e^- \rightarrow H_2O + Heat \quad [1.3]$$

The PEM needs to be hydrated for the conduction of positively charged ions, in this case the protons to the cathode. In addition, the special membrane is coated with a catalyst which allows the oxygen and hydrogen reaction to take place in the fuel cell. The catalyst layer contains platinum nanoparticles lightly coated onto the carbon membrane and is rough and porous so that the maximum surface area of the platinum can be exposed to the hydrogen or oxygen [11, 13, 14].

A detailed description of each component of the PEMFC is given in the following sections to understand the system better. The innermost layer of the PEMFC is a proton exchange membrane. Next to the membrane where all the reduction and oxidation reactions occur is the catalyst layer.

1.1.1 **Catalyst Layer**

Although the catalyst layer is the thinnest part of a PEMFC, it is the key component for the fuel cell energy conversion. This is the layer where the fuel and the oxidant react electrochemically to produce electrical work. The electrochemical reactions in PEMFCs occur slowly, especially on the cathode side. In order to increase the reaction rates, the catalyst, usually consisting of small particles of platinum supported on larger

carbon particles, must be coated either on the surfaces of the carbon support media or directly on the surfaces of the membrane [14]. These carbon particles have to be mixed with some electrolyte material to ensure that the proton can migrate towards the reaction site. The composition, morphology, and thickness of catalyst layer are key parameters in optimizing the fuel cell performance and reducing the cost. The next layer adjacent to the catalyst is the gas diffusion media.

1.1.2 **Gas Diffusion Media (GDM)**

The GDM consists of the gas transport substrate that serves the purposes of current collection and gas transport medium. It is most commonly known as the Gas Diffusion Layer (GDL). GDLs are characterized mainly by their thickness (between 100 μm and 300 μm) and their porosity. A microporous layer (MPL) is added to one side of the GDL (facing the catalyst layer, to achieve better water management. The assembly of the membrane, the catalyst layer and the GDL is termed as the Membrane Electrode Assembly (MEA).

Different GDL materials that are available are carbon fiber (CF) paper, CF non–woven felt, and CF woven cloth as shown in Figure 1.5, each with different characteristics. The CF paper has a random carbon fiber network, where the fibers are aligned in the direction that the machine draws them. An example of which is the Toray GDL (TGP) named after the company producing it. The fiber thickness is in the range of 0.15 – 0.30 mm. CF non–woven felt, also known as “SGL” is a fleece fiber mat, which has randomly dispersed fiber network with a thickness of around 150 μm. A hydro–

entangling process in which a jet of water with a spacing of 15 – 50 jets/cm is impinged onto the moving mat, bonding the fibers together. This makes the fibers orient in the through plane direction and form a non–woven fiber. Carbon cloth GDL is woven from carbon fiber yarn with a normal thickness of 150 – 200 μm. These exhibit a highly integrated fiber structure and high strength, as the yarns are tied together to form a double layer fiber with a regular interlace at right angles. A plain weave is used as it increases the dimensional stability of the fiber.

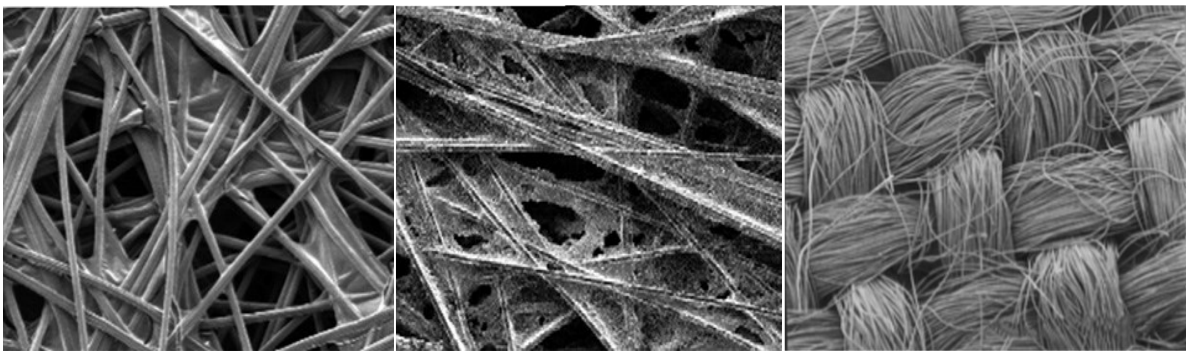

(a) **(b)** **(c)**

Figure 1.5: Different GDL sample material a) Carbon paper (Toray), b) Carbon fiber (SGL), c) Carbon cloth. Adapted from [15]

The main functionality of the GDL layer in a PEMFC is to distribute the reactant gases, air (containing oxygen) and hydrogen, more uniformly on the catalyst layer and help in the removal of the byproduct water. GDLs are very hydrophobic in nature and allow reactant gases to diffuse to the catalyst layer for electrochemical reactions to take place. The pathway for reactant gases to the catalyst layer of the PEMFC and liquid water removal are through the same network of GDL fibers. However, multiple water transport mechanisms co–exist in the GDL, which introduces tremendous challenges in fuel cell

engineering, since a proper water balance must be maintained under complicated operating conditions. Accumulation of liquid water on the GDL surface in a channel hinders reactant flow toward the reaction sites. Inefficient removal of liquid water leads to flooding of the catalyst layer. This causes localized fuel starvation, which in turn adversely affects the efficiency of the system [15]. Under freezing conditions, the accumulated liquid water leads to channel blockage and GDL degradation, which lowers the system output. However, the PEM also needs to be hydrated to conduct protons from the anode to the cathode side. Starvation of water in the system also leads to loss of performance [16]. Hence, efficient water management in fuel cells is one of the major requirements to ensure proper operation and improved performance of the system, which forms the major motivation for our work.

The component that comes after the GDL is the bipolar plate. This plate acts as a compression plate over the GDL.

1.1.3 **Bipolar Plates**

The purpose of the bipolar plate is to provide electrical connectivity between neighboring cells and to feed reactant gases to the gas diffusion electrodes. It also acts as a layer that separates different cells in a fuel cell stack. It is called a unipolar plate for a single cell [16]. Besides maintaining a good electrical contact between the bipolar plates and the GDL, a very important parameter to improve the fuel cell performance is to minimize the electrical contact resistance, which leads to the ohmic losses. As the fuel cell industry is growing, the materials used for the bipolar plates are progressively

changing according to the need desired. Different materials used for bipolar plates are gold plated copper, graphite and more recently, stainless steel.

As we have discussed the different components of a PEMFC and its working, the next section will highlight the PEMFC performance when all the above components are packaged together and run as an electricity generating device. This section will discuss some of the major losses that occur during PEMFC operation.

1.1.4 **PEMFC Performance**

The I–V curve, or polarization curve, as shown in Figure 1.6 gives the performance of a low temperature PEMFC. The electric potential of the PEMFC at open circuit (no load connected) is termed as the reversible cell potential. This is the maximum theoretical electrical potential that could be achieved for the PEMFC. Reversible cell potential is mathematically described by the Nernst Eq. under the condition of thermodynamic equilibrium [17]. However, the electric potential achieved when the load is connected is always less than the reversible cell potential. This reduction in the potential can be attributed to the different losses that occur during the operation. These losses are explained in detail below.

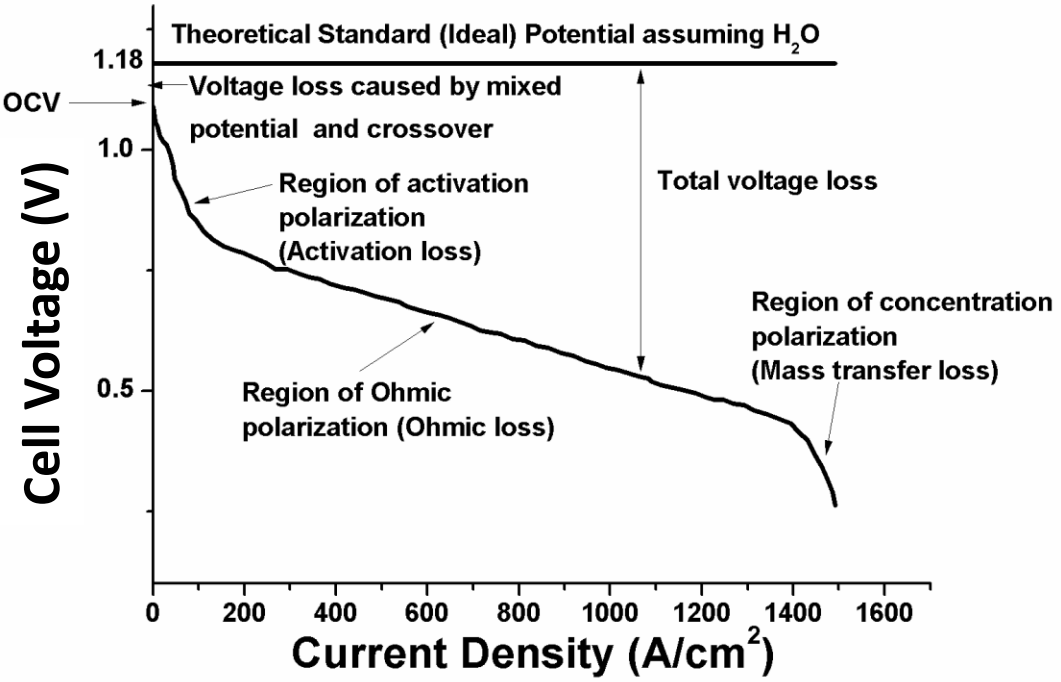

Figure 1.6: I–V Curve of a PEMFC showing the different losses that occur during the working cycle that affect the fuel cell's performance. Adapted from [18].

1) Fuel Crossover – The PEM ideally allows only protons to pass through it. However, the hydrogen species at the anode side diffuses across the membrane and combines with the oxygen at the cathode side. This is known as fuel crossover and this fuel is consumed without producing any useful electrical power.

2) Activation Loss – Activation losses in a system are mainly due to the slow reactions on the surface of the electrode. In a PEMFC, the activation losses occur mainly on the cathode side since the exchange current density of the anode reaction is several orders of magnitude higher than that of the cathode reaction.

3) Ohmic Loss – Resistance posed by the membrane to proton transport and sometimes the electrical resistances of the assembly are termed as ohmic losses.

4) Mass Transport Loss – Mass transport or concentration losses are caused by the reduction of the reactant concentration at the electrode surface due to consumption of the reactants. Usually, these losses are significant when the cell is working at a relatively high current density.

Some of these losses in the cell are due to poor water and heat management in the fuel cell. In order to increase the fuel cell's performance, an in depth understanding of these aspects is required. As this dissertation mainly deals with the water management aspect of the fuel cell, issues in the water management of PEMFC are described in detail in the next section.

1.2 Water Management in PEMFC

Intertwined with each of the challenges mentioned above is the issue of water management in PEMFCs. The presence of water inside the fuel cell is necessary to hydrate the PEM. Various alternatives to Nafion that may be cheaper, more durable, or thinner still require hydration to operate well [19]. Working of the fuel cell is by the conduction of protons through the membrane from the anode side to the cathode while driving electrons through the external circuit. Useful work done by the cell depends on the amount of electron flow in the system. The flow of electrons around the circuit is equivalent to the conduction of protons through the membrane. However, the conduction of protons is dependent on the water activity in the membrane. A highly hydrated

membrane causes too much water generation at the cathode side that leads to the gas channel flooding if not removed efficiently. To achieve efficient removal of the liquid from the gas channel, more power is supplied to the blowers to provide excess gas flow in the cathode channel. In contrast, when a fuel cell is designed to run at operating conditions that remove too much water from the system, external humidification feed is necessary to keep the membrane hydrated, which increases the cost and complexity of the system [20]. With more careful system designs, the membrane can absorb the water produced by the electrochemical reaction and extra humidification may not be needed.

However, under normal operating conditions, water production can be substantial enough to saturate the fuel cell and cause accumulation of liquid water. The liquid water is problematic, as it can block the reactants from reaching the catalyst and hurt the fuel cells performance. Furthermore, very high potential gradients can be created with areas of local reactant starvation caused by liquid water blockages, and the degradation of the catalyst material can also be accelerated.

The most common solution for removing the excess water is to increase the flow rates of the gas and simply blow the liquid out of the channels. In order to do this, the reactant supply needs to be increased, which complicates the problem, as it requires extra pumping, fuel recycling, and humidification. This increases the system cost and complexity along with the consumption of extra power for the auxiliary systems and the overall size of the cell.

Engineering the fuel cell for effective removal of liquid from the gas channels is a much better approach to resolve these issues. Lower gas flow could be used to eliminate the need for excess gas flow in the channel and the external humidification and recycling unit. The ability to make significant improvements over the conventional fuel cell gas channel designs requires (1) a thorough understanding of the fundamental physics of liquid behavior on the GDL and the channel surface at different operating conditions and (2) understanding the effect of channel geometry on the water removal from the gas channel. This forms the major motivation of this dissertation.

1.3 Document Overview

The remainder of the dissertation is organized as follows. Chapter 2 provides a detailed literature review of past research that relates to the water management aspects of a fuel cell. This section also describes the physical theories involved in the liquid water behavior on a given surface. In addition, some of the designs for different gas channel geometry and their effect on fuel cell efficiency are presented in this chapter. Chapter 3 defines the objectives of this dissertation along with the description of the experimental setup and the equipment used to conduct the experiments. This section also describes the manufacturing process and the different test conditions used to perform the experiments. Subsequently, Chapter 4 presents the experimental results to illustrate the effect of different parameters analyzed on the liquid water behavior in the PEMFC gas channels. Chapter 5 describes the theoretical models explaining the results obtained with the experiments in Chapter 4 and provides a correlation to understand the droplet dynamics

in the absence and presence of airflow in the gas channels. Chapter 6 provides a conclusion and key points of the research work performed for this dissertation. Finally, Chapter 7 brings out the different areas this research work can be extended to help in understanding fuel cell performance and improves it.

Chapter 2 Literature Review and Motivation

Water management is an important performance limiting concern for the operation and optimization of the PEMFCs. Efficiency of the PEMFC system depends upon various factors that affect the cathodic reaction rate [12, 21-25] such as

(a) The proton permeation from anode to cathode

(b) Liquid water presence in the GDL and the gas channels

(c) Blockage of the reactant gas flow to the catalyst sites by liquid water.

Figure 2.1 shows the blockage of a gas channel by water and its effect on the PEMFC's efficiency. One of the main reasons for liquid flooding in the gas channel and high pressure drop in the system are the surface tension forces acting in the channel [26]. Apart from this, liquid water hold up in the gas channel is also dependent on the gas channel geometry and the material used for the gas channel and the GDL. Previously, many researchers have worked on the water management issue in the gas channel of PEMFC in both *in situ* and *ex situ* to understand the main reasons for channel flooding and high pressure drop in the cell. Yet the optimal design of the gas channel needs further understanding in terms of the effect of surface tension forces on liquid water, channel geometry's effect on gas transport resistance, and the water interaction pattern with the channel walls in the presence of gas flow. Therefore, the work presented in this dissertation uses experimental and theoretical methods to study the physics of droplet behavior in geometries common to practical fuel cells, which is critical to their performance.

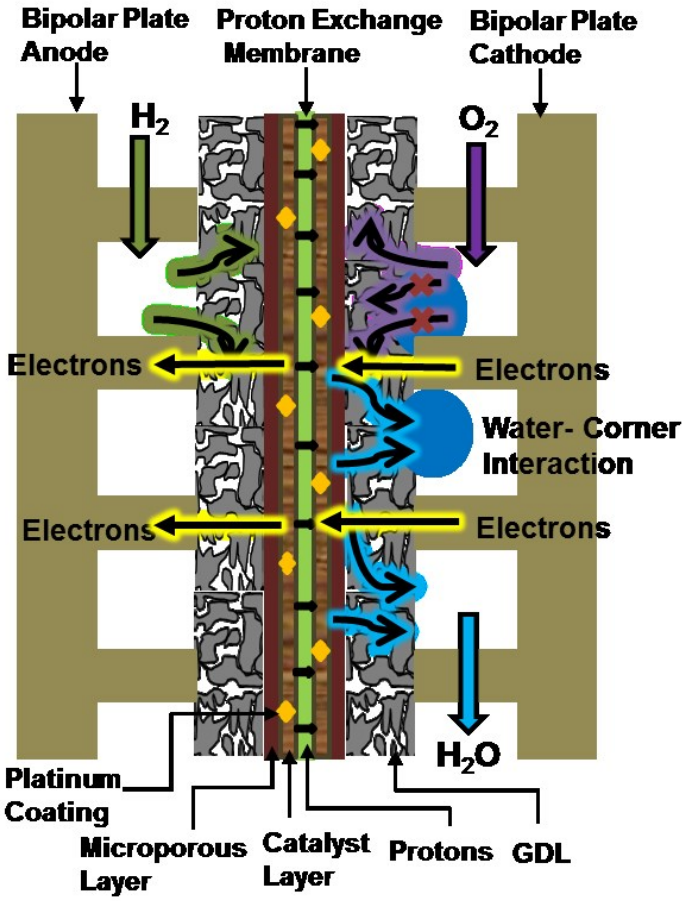

Figure 2.1: Water accumulation on the GDL and leading to flooding of the channel, which hinders the reactant gas diffusion to the catalyst layer. Adapted from [12].

A critical factor in the water management of PEMFCs is the droplet stagnation on the GDL surface and the channel sidewall. The basic phenomenon determining the droplet behavior inside the microchannel is the surface tension force, which holds the droplet on a given surface. The surface forces with which the droplet is held on a surface are defined by the static contact angle, advancing and receding contact angles, contact angle hysteresis ($\Delta\theta$), and the roughness of the surface. The following section will elaborate more on these parameters.

2.1 Contact Angle

Contact angle is a quantitative measure of the wetting of a solid surface by a liquid. The theoretical prediction of the contact angle arises from the consideration of a thermodynamic equilibrium between the three phases: the liquid phase of the droplet (L), the solid phase of the substrate (S), and the gas/vapor phase of the atmosphere (V). The gas phase could also be another (immiscible) liquid phase. At equilibrium, the net forces due to the three phases should be zero. Figure 2.2 shows a graphical representation of a droplet on a smooth solid surface.

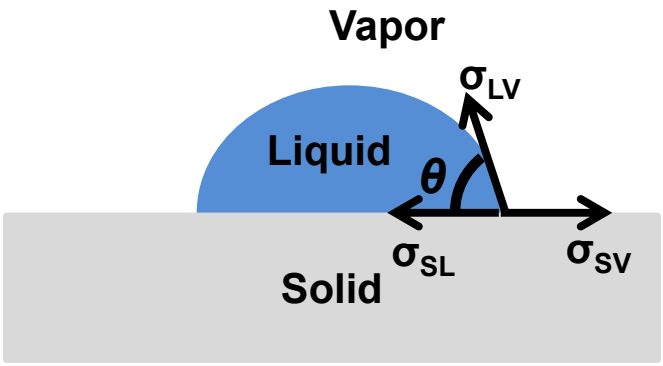

Figure 2.2: Graphical representation of a droplet on a smooth surface and the different forces acting on it

At the thermodynamic equilibrium of the three phases, the force balance along the contact line (CL) determines the contact angle of the droplet on that surface. The contact angle value on a given surface is determined using Young's Eq.

$$\sigma_{SL} + \sigma_{LV} \cos\theta - \sigma_{SV} = 0 \qquad [2.1]$$

$$\cos\theta = \frac{\sigma_{SV} - \sigma_{SL}}{\sigma_{LV}} \qquad [2.2]$$

where θ is the equilibrium contact angle, σ_{SV} is the solid–vapor surface tension, σ_{SL} is the solid–liquid surface tension, and σ_{LV} is the liquid–vapor surface tension. Based on this equilibrium angle, the surfaces can be classified as hydrophilic and hydrophobic [27]. For a hydrophilic surface, the contact angle θ, is small, i.e. less than 90°, which means that the droplet would spread on the surface as shown in Figure 2.3(a). If θ is larger than 90° then the water droplet would repel the surface and form a spherical shape as shown in Figure 2.3(b). Such surfaces are known as hydrophobic surfaces. In addition, surfaces having contact angles between 0° – 20° are classified as superhydrophilic whereas surfaces with contact angles between 150° – 180° are known as superhydrophobic.

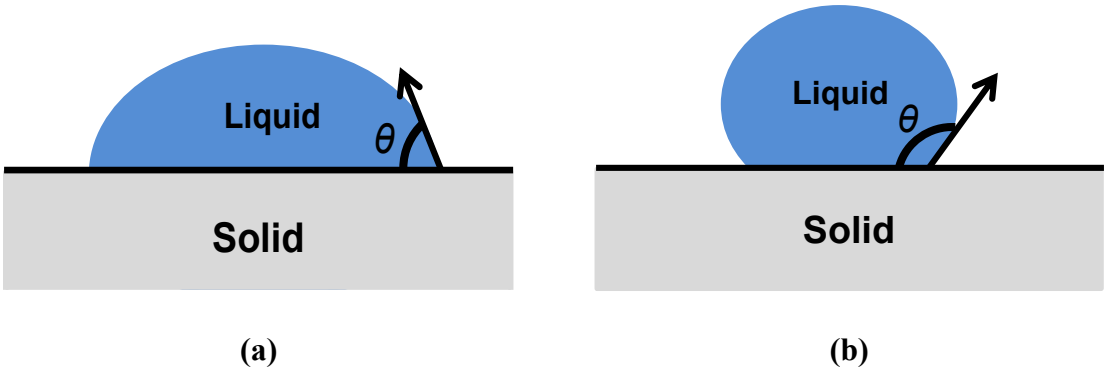

Figure 2.3: Graphical representation of a droplet on different surfaces (a) Hydrophilic surface and (b) Hydrophobic surface

2.2 Contact Angle Hysteresis

Equilibrium contact angle does not give much information about the droplet behavior of a given surface. In order to quantify the droplet behavior on a given surface,

the contact angle made by the CL of the droplet when it is about to move is required. The angles made by the droplet when it is in advancing equilibrium are shown in Figure 2.4. The advancing contact angle, θ_A, is the maximum contact angle that the droplet can have before it starts to move on the given surface. The receding contact angle, θ_R, is the minimum angle that the droplet can have before it gets de–pinned from the surface and starts to move. Therefore, the CL on any given surface can take the shape of any angle such that $\theta_R < \theta < \theta_A$. The difference between the advancing and receding contact angles is known as the contact angle hysteresis and is denoted by $\Delta\theta$ [28].

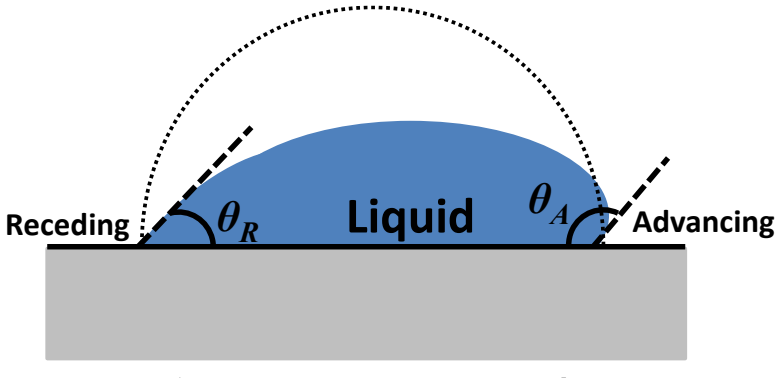

Figure 2.4: Different contact angles made by the droplet just before it moves on a surface. Advancing and receding contact angles are shown by θ_A and θ_R

$\Delta\theta$ describes the ability of a liquid to stick to a solid surface. Superhydrophobic surfaces are characterized by low $\Delta\theta$ as a droplet can roll off a surface very easily, and vice–versa for superhydrophilic surfaces. $\Delta\theta$ has a major effect on the buildup of water in the microchannel due to sharp corners or roughness [29]. Roughness on a surface affects the $\Delta\theta$ as well as the apparent contact angle of the surface. Therefore, to understand the wetting characteristic of a surface, the roughness of the surface also needs to be taken into account.

2.3 Roughness Effect on Contact Angle

The hydrophobicity and the hydrophilicity of the surface are also affected by the surface roughness. In the case of a PEMFC, the GDL is made up of entangled carbon fibers, which make the surface of the GDL rough. If the size of the water droplet present on the GDL is in the same order as the actual surface roughness, then the roughness factor has to be considered while calculating the contact angle. However, the contact angle of a droplet on a rough surface is very difficult to measure because of the irregularities as shown in Figure 2.5. In the Figure 2.5, it can be seen that the surface has depressions and peaks. Hence, when the droplet sits on such a surface, the contact angle measurement becomes difficult and can be wrong depending upon from where it is being measured.

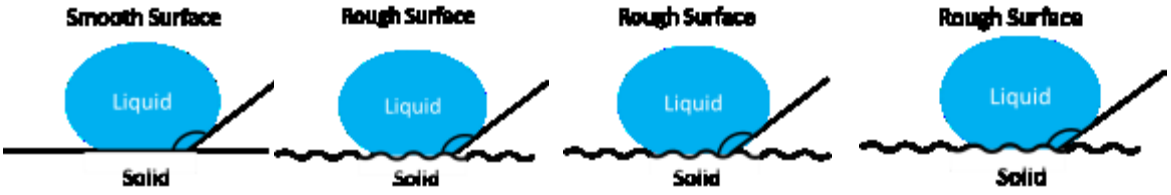

Figure 2.5: Discrepancy in the contact angle measurement due to the roughness features on a rough surface.

To account for the surface roughness, Wenzel proposed a model to calculate the contact angle as a function of the surface roughness parameter [30]. According to his proposition, the contact angle for a rough surface of a material can be determined by

knowing the contact angle of a liquid droplet on the same material but with a smooth surface by using Eq. 2.3

$$\cos\theta_r = r\ \cos\theta \qquad [2.3]$$

where, θ_r – contact angle on a rough surface, θ – equilibrium contact angle on a smooth surface, r – roughness factor; r is always greater than 1 for a rough surface.

According to this model, a droplet placed on a rough surface would spread until it finds an equilibrium position given by the contact angle θ_r. It also predicts that the roughness on a surface enhances its wettability if a surface is hydrophilic, and the roughness causes it to become more hydrophilic (or more hydrophobic if the surface is initially hydrophobic) [31-33].

For porous surfaces, Cassie–Baxter (CB) developed a model which includes the material heterogeneity, f_i , for calculating the apparent contact angle, given by Eq. 2.4 [34].

$$\cos\theta_r = \sum f_i\ cos\ \theta_i\ = \mathrm{f}_1\cos\theta_1 + \mathrm{f}_2\cos\theta_2 \qquad [2.4]$$

where f_1 and f_2 are the area fractions of the material 1 and 2 respectively and θ_1 and θ_2 are the static contact angles for material 1 and 2 respectively.

Similarly, the CB Eq. was modified further considering that the droplet is formed on a peak of the roughened surface and there is an air gap in between the material and the liquid. An illustration for such a condition is shown in Figure 2.6. In this case, the Eq. 2.4 is modified and is described by Eq. 2.5

$$\cos\theta_r = f\ (\cos\theta - 1) \qquad [2.5]$$

where, f is the area fraction of the material

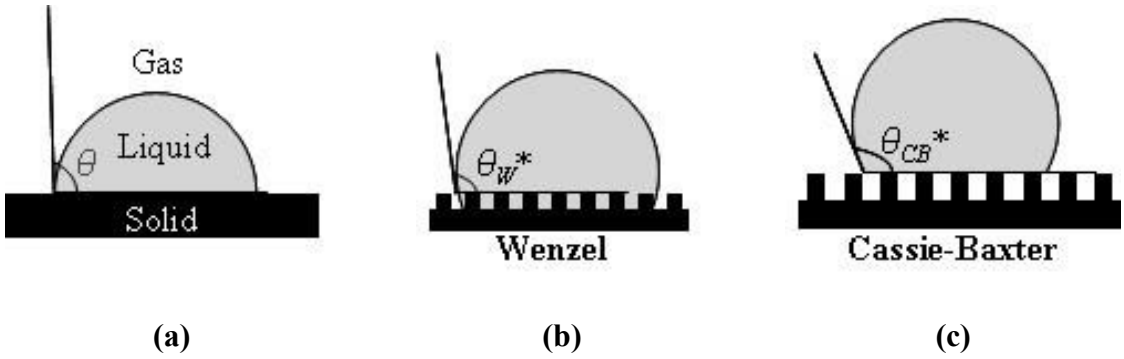

Figure 2.6: Different wetting behaviors of the droplet on smooth and rough surfaces. a) Droplet on a smooth surface b) Wenzel type droplet wetting on rough surface c) Cassie–Baxter type droplet wetting on a rough surface. Adapted from [35].

The volume of the air trapped inside a liquid droplet, provided the surface roughness of the material is non–negligible, affects the contact angle drastically. Hence, the volume of the liquid is important to determine the resulting contact angle [36]. Secondly, the material surface wettability can be enhanced by having a double roughness on the surface. Double roughness is the integration of a nanoscale texture on microscale pillar like structures [37]. As with normal surface roughness, double roughness patterns also tend to increase the hydrophobicity and hydrophilicity characteristics of the surface and random roughness tends to have a greater effect on the contact angle [38, 39]. Thirdly, surface roughness affects the $\Delta\theta$ due to the droplet pinning on the material. Droplet pinning means that the droplet is stuck on a material either due to higher surface tension forces or due to the roughness. If a droplet on a rough surface tends to obey the Wenzel model, then the $\Delta\theta$ is higher compared to the CB model of droplet wetting. These studies

aid in realizing the significance of the roughness on the material behavior and act as a building block for complete understanding of the droplet pinning phenomenon – a critical factor in the water stagnation inside the gas channels of a PEMFC.

The CB model also suggests that a textured surface enhances the hydrophobicity of a given surface. In literature, it has been shown that textured surfaces of different sizes (10 – 100 nm) act as superhydrophobic surfaces that are very useful in manufacturing and chemical industries [40-45]. Some recent experiments have also shown that surfaces with texture sizes in the range 1 – 20 nm can exhibit superhydrophobicity [43, 44, 46]. Both the Wenzel and CB models are extensively used to predict the apparent contact angle on rough and porous surfaces respectively. However, the fact that these models take into account the total contact area of the droplet on the surface is still a controversial and much debated topic by various groups [40, 46-48]. Consequently, modification of the classical model based on the contact line length has been proposed [40, 46-50]. It was also shown that both the Wenzel and CB models are not valid when the droplet size is comparable to the roughness height [32, 51-54]. In 2007, Nosonovsky derived the following Eq. 2.6 to determine the contact angle on a rough surface at the triple line.

$$\cos \theta_r = r(x,y) \cos \theta \qquad [2.6]$$

and for a composite surface, the CB Eq. was modified to use the contact line of the droplet as shown in Eq. 2.7.

$$\cos \theta_C = f_1(x,y) \cos \theta_1 + f_2(x,y) \cos \theta_2 \qquad [2.7]$$

There have also been further studies to understand the effect of apparent contact angle for a given surface on the wetting characteristics as well as analyzing the Cassie–Wenzel (CW) wetting regimes transition which is critical[38, 40-42, 47, 50, 55-75]. Understanding the mechanism of wetting transitions is very essential for designing highly stable superhydrophobic surfaces. Different microstructure surfaces have been developed to achieve a superhydrophobic state. It has been observed that the droplets on these surfaces are in a Cassie state rather than in a Wenzel state [76]. This is mainly because the droplets in the Wenzel state are pinned more strongly on the textured surface than in the Cassie state and lead to a larger $\Delta\theta$. Therefore, the Cassie state is preferred over the Wenzel state to obtain superhydrophobicity. It has also been established that for highly rough surfaces, the Cassie state is more prevalent than the Wenzel state. Accordingly, various mechanisms used previously to promote the wetting transitions such as depositing the droplet from a higher position [77, 78], applying external pressure [79], application of voltage – electrowetting [80], and vibrating the substrate in the horizontal and vertical directions [81-84], corroborate with this fact. But on the basis of very few attempts that were made to understand the wetting transition on a pillar structure [32, 76], it was confirmed that smaller and more densely packed structures lead to better stability of the droplet which acts as a Cassie droplet. However, to achieve maximum roll off over superhydrophobic surfaces, a large separation between the structures is required, which may lead to droplet instability and result in CW transition[79]. Furthermore, there is a lack of relevant work examining the transition of wettability on a groove structure and analyzing the effects of geometric and structural parameters of the wetting transition on a surface. It is therefore essential to gain an in–depth understanding of the droplet behavior

under different scenarios in order to optimize the surface characteristics for a specific application.

2.4 Droplet Behavior Touching Two Surfaces

The above mentioned phenomena give an understanding of the droplet behavior on a given surface. However, when there are two surfaces in contact with each other and the liquid is placed on these surfaces such that it touches both the surfaces, then its behavior is completely different. Concus and Finn in 1969 analyzed liquid behavior on a wedge surface and proposed a model which predicts the rise height of a fluid in a wedge shaped domain [85]. Eq. 2.8 gives the condition such that if this condition is satisfied the liquid with rise otherwise it will not rise near the wedge.

$$\alpha + \theta \geq \pi/2 \qquad [2.8]$$

where α is the half the open angle of the wedge and θ is the contact angle of the surface.

This condition was later modified by Concus and Finn for two different surfaces contacting the liquid and the modified Eq. is given by Eq. 2.9 [86, 87].

$$2\alpha + \theta_1 + \theta_2 \geq \pi \qquad [2.9]$$

where θ_1 and θ_2 are the contact angles of the two surfaces 1 and 2 as shown in Figure 2.7(a). They also represented the condition graphically as shown in Figure 2.7(b). In this plot, the contact angle values for the two surfaces are plotted against each other and when the data point falls in the shaded region, the Concus–Finn condition is valid and a

solution exists, i.e. the liquid will rise in the channel. On the contrary, if the contact angle point falls in the D^+ or D^- region, then there exists no solution.

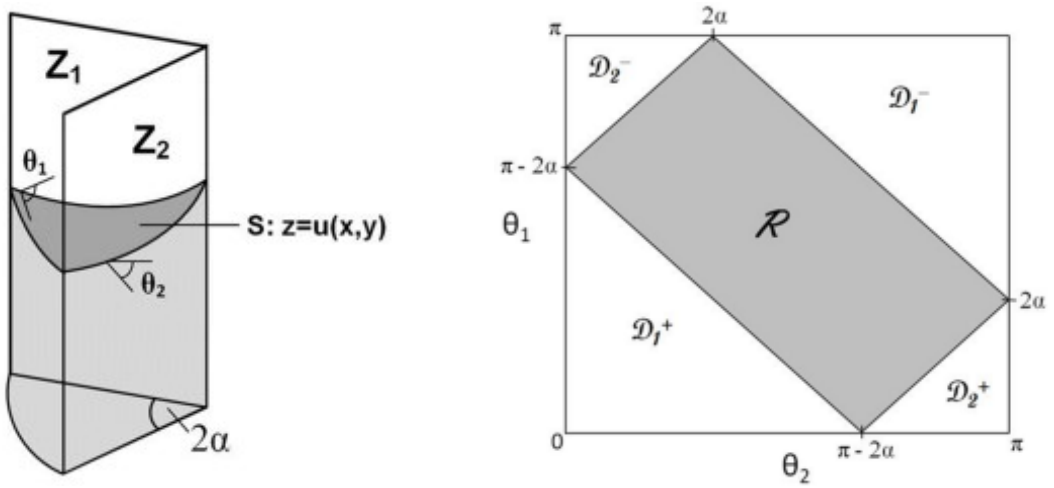

Figure 2.7: (a) Model showing the angles made by the liquid with the wedge surface (b) Plot representing the Concus-Finn condition for wedge surface where the plot represents the contact angle made by the liquid on the wedge surfaces. Points that fall in the shaded region R have solution for the Concus–Finn condition. For the points falling in the D_1^+, D_1^-, $D_2^+$and D_2^- no solution exists. Adapted from [86].

This model was further extended to understand how the droplet interacts with the surfaces near a wedge or channel corner. It was found that the droplet could lead to two different kinds of behavior, i.e. filling (water sucked into the channel corner) or non–filling (droplet remains at a finite distance from the corner, referred to as an "enclosure effect") the channel corner. Enclosure effect is shown in the Figure 2.8(a). Corner filling and non–filling behaviors could also be explained using the graphical 2D plot as shown in Figure 2.8(b). The plot shows that when the point falls in the shaded region, the droplet will fill the channel corners. When the points fall on D^+ or D^- region, the droplet will lead

to no filling of the channel corners also, known as enclosure condition. Many researchers have used this for understanding the droplet behavior in the gas channels of PEMFCs and are discussed in Section 2.6 [88-96].

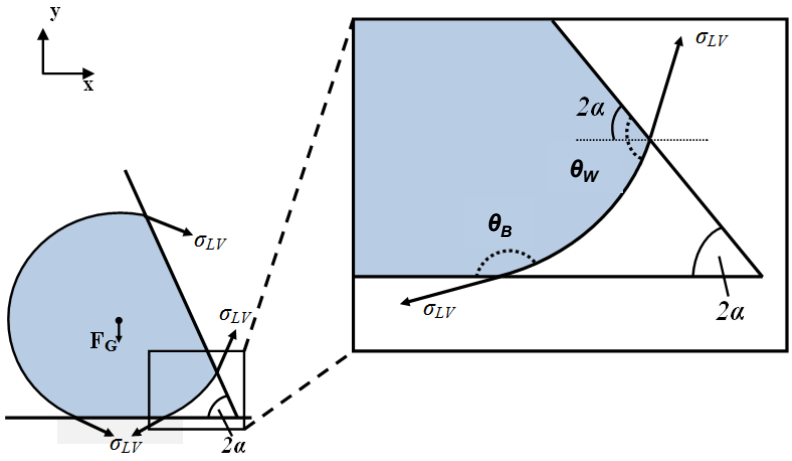

(a)

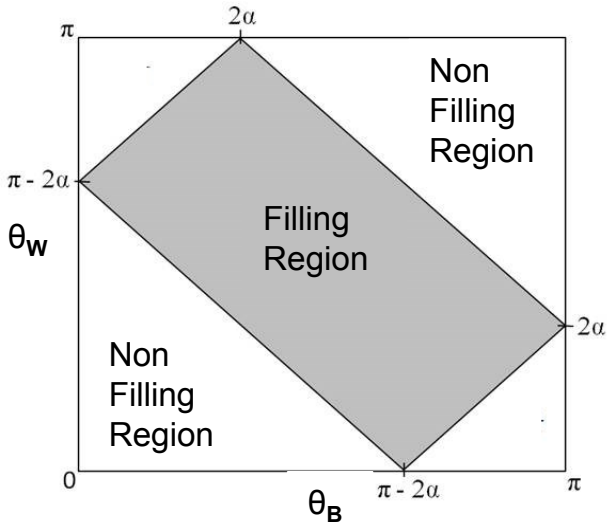

(b)

Figure 2.8: (a) Model showing the angles made by the droplet near the channel corner wedge and (b) 2D plot representing the Concus-Finn condition for wedge surface. When the contact angle of the wedge material falls in the shaded region, then the corner of the channel would be filled. If the contact angle point falls in the non–shaded region then the channel corners would remain non–filled. This is also known as enclosure effect. Adapted from [94].

2.5 *Ex situ* and *In situ* Water Visualization Techniques

Exploration of two-phase transport inside a porous GDL is not an easy task, either by performing experiments or numerical simulations. There have been several methods that have been used to visualize the liquid water removal from PEMFCs by performing *ex situ* as well as *in situ* experiments. Some of the imaging techniques that have been explicitly used are neutron radiography [88, 97-99], X–ray radiography [100], fluorescence microscopy [101], nuclear magnetic resonance (NMR) microscopy [102], and magnetic resonance imaging (MRI) [103-106]. Litster *et al.* in 2006 conducted an *ex situ* experiment to visualize liquid water transport through the reactant gas channel using a fluorescence microscopy technique [106]. For this work, fluorescein dye solution was pumped through the GDL and imaged using fluorescence microscopy. It was found that the liquid moved through the GDL pores through a certain defined path, which forms finger like structure between two droplets that emerges as shown in Figure 2.9(a). On the contrary, Pasaogullari and Wang in 2004 predicted that water transport through the GDL to the channel region follows an "upside down tree" network as shown in Figure 2.9(b) [107]. Manke *et al.* in 2007 reported that liquid water generated at the catalyst layer travels through the GDL layer to the rib or land region [100]. Water from under the land region is drained into the channel region as shown in Figure 2.9(c).

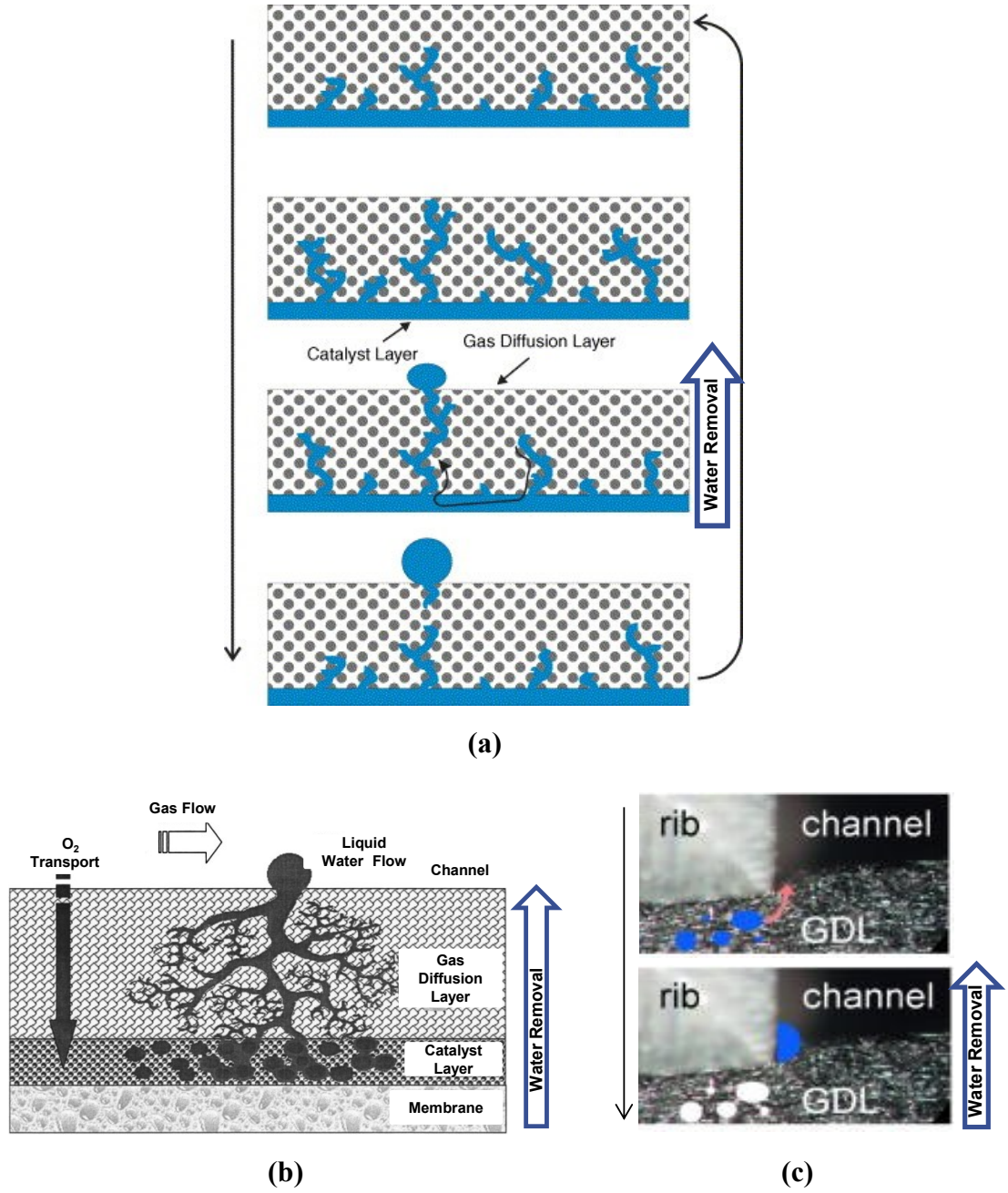

Figure 2.9: Different theories proposed for understanding the droplet movement from the catalyst layer to the channel region. (a) Droplet movement from the catalyst layer to a channel through the GDL by fingering and channeling pathway. Adapted from [106], (b) The upside down tree model for water removal from the catalyst layer to GDL surface. Adapted from [107]. (c) Liquid water generated in the catalyst layer travels through the GDL layer from under the rib region and erupts or drains into the channel region. Adapted from [100].

Later on, other techniques such as X–ray radiography, ultrasound, NMR and MRI microscopy techniques became popular for the visualization of water in PEMFCs. In 1999, researchers from the National Institute of Standards and Technology (NIST) developed neutron imaging technologies to investigate water transport in PEMFCs [98]. Satija *et al.* in 2004 designed their PEMFC such that they could visualize liquid water production, transportation and removal from the fuel cell using neutron imaging techniques [97]. Owejan *et al.* in 2006 also performed *in situ* testing on an interdigitated cathode flow field to quantify the amount of liquid water transport through the porous GDL in a PEMFC [96]. The results showed that the water accumulated in certain regions of the porous media while there were few regions where the reactant gases established a consistent in-plane transport path through the porous media. Neutron imaging has the capability to image the diffusion media easily. For *in situ* experiments of water quantification, neutron radiography and MRI microscopy techniques [97, 99, 102-104] have been very promising due to their non–intrusive nature and their ability to visualize the liquid inside a porous GDL. However, their extensive application is restricted by high cost, limited availability and complex modification to the system[108].

There have been several other methods used to investigate water management issues in a cost effective way. One of the methodologies uses transparent materials to visualize the gas channel[88, 109-114]. Tuber *et al.* first studied the effect of GDL material on water management using transparent material for the fuel cell assembly. They visualized the water emergence using optical imaging technique. It was experimentally verified that the hydrophobic coating (PTFE) applied on the GDL fibers affects the water

transport in the cell. It was observed that the water distribution was much more random within the channel and not a continuous process. Esposito *et al.* used a fluorescent die and transparent *ex situ* setup to visualize the droplet deformation when it was exposed to the gas flow in the channel [114]. They were able to visualize the advancing and receding contact angle made by the droplet due to the shear force exerted by the airflow in the channel.

Kandlikar *et al.* have performed extensive work by using visually accessible fuel cell [109, 115-119]. Sapphire windows, which are transparent, have been used to visualize the gas channel to study the effect of GDL, channel geometry and flow maldistribution in the PEMFCs. They were able to classify the water flow pattern as a function of the water and the superficial air velocities in the channel. They also found that water emergence on the GDL was a more dynamic and discrete process when compared to the continuous water eruption mechanism suggested by the previous researchers. The water emergence follows a mechanism similar to the Haines Jump process, shown in Figure 2.10, observed in geological studies. Haines Jump mechanism is described as the liquid movement through a porous material. Here the liquid would emerge to the surface of the porous material at one location and drain all the liquid there. The next pore location where the liquid has filled the pores completely would drain out on the surface and the process continues. Hence, the liquid emergence on the surface of the porous material is a discontinuous process. Studies were also conducted to understand the GDL intrusion effect into the gas channels, and it was observed that the channel area was

reduced due to uneven compression of the GDL and an increase in the pressure drop due to intrusion in the channels.

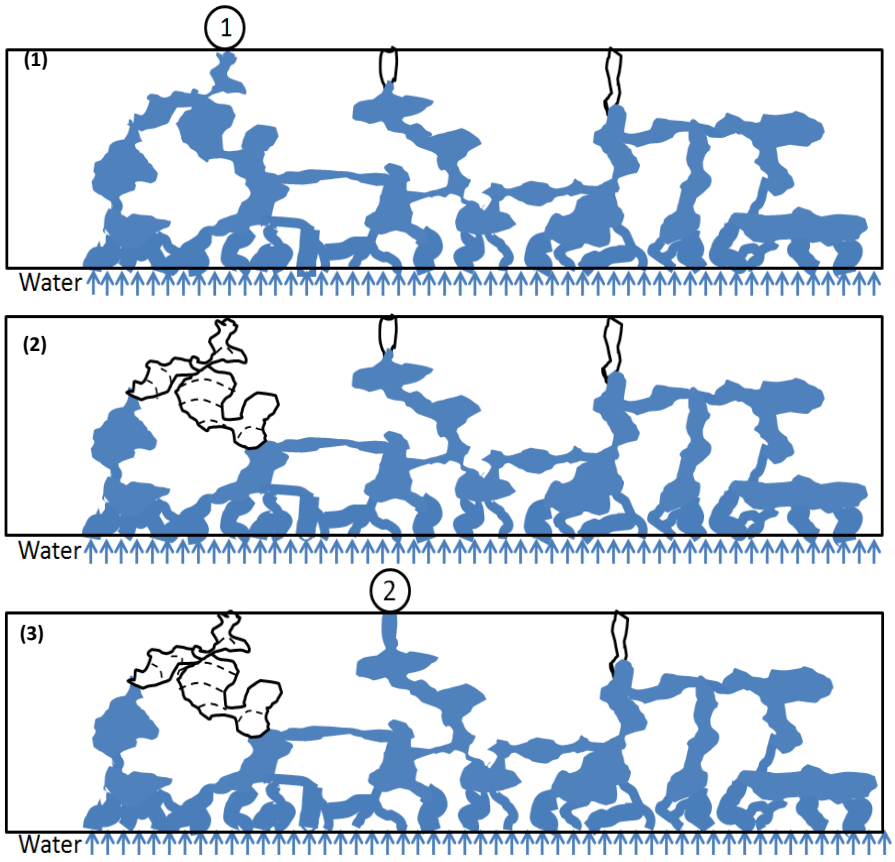

Figure 2.10: Water emergence from the GDL into the gas channel follows Haines Jump Mechanism. Adapted from [118].

Visualization of the gas channel has provided valuable information about the droplet dynamics in the gas channel of PEMFC's. However, fundamental understanding of the different phenomena and different forces affecting the water removal process from the gas channel is essential.

2.6 Different Phenomena Affecting the Water Removal from Gas Channels

It was revealed from the literature that the water accumulation at the corners where the GDL and the channel walls of the gas channel meet leads to increased pressure drop in the channels [91, 92]. Water stagnation in the gas channels hinders the reactant gas flow to the catalyst layer where the reaction occurs, and lowers the overall efficiency of the cell [120, 121]. Water removal from the gas channel is dependent on several factors such as gas velocity, contact angle on the GDL and channel wall surfaces, $\Delta\theta$, droplet emergence location, and the cross sectional geometry of the channel [88, 89, 91-94, 117-133]. Gas flow in the channel can exert a pressure force on the droplet modifying its shape, detaching it from the GDL and the channel wall surfaces, and removing it from the gas channel [128-131].

2.6.1 Forces Affecting Droplet Removal

A droplet or a slug (elongated droplet touching the sidewalls) experiences different forces that act on it and determine its movement in the gas channel. Figure 2.11 shows the different forces acting on a droplet which include gravity (F_g), surface tension (F_σ) and the drag force (F_D) applied due to the gas flow in the channel [134, 135]. It is seen that the droplet moves in the gas channel when the gravity and drag forces overcome the surface tension force holding the droplet in the channel.

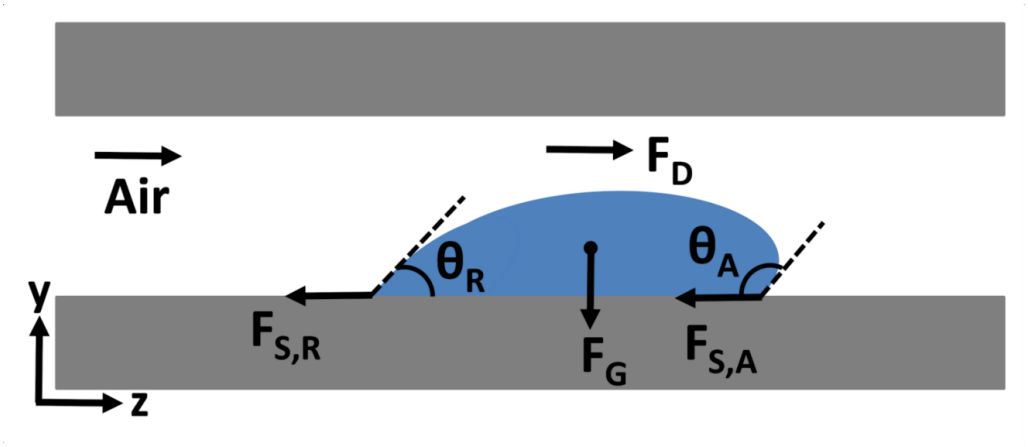

Figure 2.11: Different forces acting on a droplet in the PEMFC gas channel.

The effect of gravity on the droplet (or slug) depends on the size of the droplet. This is generally governed by the Bond number, $B_o = \frac{\rho g D^2}{\sigma}$, which is the ratio of the gravity force to the surface tension force. It is reported that if $B_o \sim 0.1$ or lower, the surface tension forces are dominant in the system and the gravity forces can be neglected [120, 136]. Since the channel size used for gas channels is smaller than about 1 mm, the droplet sizes in the channel are also quite small. Hence, most of the studies in PEMFCs neglect the gravity effect on the droplet. However, it is also seen in few studies that gravity does have an effect on the droplets in the PEMFC gas channels [119, 132, 134, 137-139].

Kimball *et al.* performed a study to understand the effect of gravity on water movement in the gas channel [134]. They mentioned that the motion of the slug in the gas channel is gravity dependent when the fuel cell is placed vertically. The reactant gas channels are blocked and the current density fluctuates when the slug has to move against gravity. They also found that the gravity effects were amplified when the large pore for

droplet emergence was under the channel region. However, when the large pore was under the land region, the gravity effects diminished [137]. Yi *et al.* also studied the effect of gravity on fuel cell performance and concluded that at an optimized gravitational angle for cell orientation, the output power of PEMFC stack can be enhanced greatly [138]. Chen and Wu studied the effect of gravity on water discharge in PEMFC gas channels [139]. They concluded that the excess water present in the cathode channel is easily removed from the cell when the anode channel orientation is upwards. They also suggested that the placement of the anode and the cathode is very important for the performance of the PEMFC. Lu *et al.* studied the effect of the orientation of the cell on water distribution and flow patterns in the gas channels and also found that the vertical orientation of the cell was beneficial for the water flow pattern and the two phase flow in the gas channels as compared to a horizontal cell [119]. Cheah *et al.* performed experiments to understand the effect of gravity and surface wettability on the liquid behavior in the PEMFC gas channels [140]. They suggested that the selection of channel geometry, surface wettability, and orientation for the fuel cell flow channel should not be made in isolation. Horizontally mounted hydrophilic square channels would produce large slugs that would require lower energy for removal. However, these large slugs would produce large mass transport resistances for the reactant gas to diffuse to the catalyst layer. On the other hand, a hydrophobic square channel would produce smaller slug and require more energy for its removal. However, the smaller slugs would minimize the problems of reactant transport. Das *et al.* studied the effect of adhesion force on the liquid water removal from the GDL [132]. They reported that for droplets smaller than 1.5 mm in diameter, the gravity effect could be neglected. However, when

the droplet size is above 2 mm or B_o is above 0.14, gravity has a significant effect on their removal. Therefore, it can be concluded from these studies that the gravity effect in the PEMFC gas channel can be neglected only when the droplet diameter is smaller than 1 mm or B_o less than 0.1, otherwise it needs to be considered in the analysis.

The surface tension forces also play a major role in the droplet removal process. The adhesion force exerted by the surface tension on the droplet is a function of the surface wettability defined by the contact angle (θ) and the contact angle hysteresis ($\Delta\theta$) [27]. When $\Delta\theta$ of a material is high, a larger drag force is required from the airflow in the channel to remove the droplet. When a droplet interface has an angle $\theta < 90°$, it is called a hydrophilic surface and the liquid would spread. In an interface with $\theta > 90°$, known as a hydrophobic surface, the liquid repels the surface and tries to attain a spherical shape. Droplet removal from a hydrophobic surface is easier as the force required to remove the droplet is less than a hydrophilic surface for a given $\Delta\theta$. The GDL being a hydrophobic surface allows droplet removal relatively easily as compared to a hydrophilic channel surface.

There have been many analytical models proposed in the past to understand the effect of different forces acting on a droplet growing on the base of a microchannel [124, 125, 127, 128, 141-144]. These models generally employ force balance or torque balance to evaluate the effect of different parameters and membrane properties on droplet formation and its removal. Luca *et al.* tried to validate these two models with experimental data available in literature and found that the force balance model yields better results when wall shear stress is above 7 Pa and membrane pore diameter is below

1.5μm [144]. On a similar note, Chen *et al.* presented a simplified model based on macroscopic force balance and droplet geometry approximation for predicting the instability in the droplet which leads to its removal from the GDL surface [128]. Zhang *et al.* performed experimental and analytical studies and developed a correlation for the droplet detachment diameter from the GDL surface in terms of velocity and Reynolds Number (Re) [120]. Similarly, Ha *et al.* performed experimental study to understand the droplet detachment characteristic from the GDL and complimented it with a simplified model [145]. The model was used as a criterion to estimate the droplet instability and removal tendency in the gas channel.

Hao and Cheng performed numerical simulations using the Lattice Boltzmann method to understand the influence of gas flow velocity and GDL surface wettability on droplet detachment size and droplet removal time from a gas channel [141, 142]. They also developed analytical models based on force balance to predict the droplet detachment size and the shear force required to move the droplet on a hydrophobic wall in terms of dynamic contact angles for a steady velocity profile. Similarly, Cho *et al.* investigated the dynamics of liquid water in PEMFC gas channels through numerical and analytical studies [124, 125]. They used CFD simulations to determine the droplet detachment velocity by comparing the wall adhesion and drag force. They found that the viscous force has a significant impact on smaller droplets at lower air velocities, whereas the pressure drag is dominant for larger droplets. Golpaygan and Ashgriz conducted a numerical study to understand the effect of gas flow properties and liquid droplet on the droplet mobility in the gas channel. It was observed that surface tension has the greatest

influence among the parameters affecting the droplet mobility [129]. The higher the surface tension, the more difficult it is to remove the droplet from the microchannel. Theodorakakos *et al*. numerically investigated the detachment of a liquid droplet from the GDL surface under the influence of air in cross flow [130]. They provided a correlation to find the critical air velocity, for a given droplet size, at which the droplet is removed from the GDL. This data was compared with the experimental results, and the adhesion force between the liquid droplet and the solid surface was estimated. From all these works, the GDL and channel wall surfaces are seen to have a major influence on the liquid water removal from the gas channels.

2.6.1.1 Effect of GDL Surface on Droplet Removal

Surface forces depend mainly on the advancing contact angle, receding contact angle, and the $\Delta\theta$ on the material surface. In general, different GDL materials used in PEMFCs possess different surface characteristics, and thus, differ in their droplet accumulation characteristics within the gas channel [24, 25, 111, 131, 146, 147]. Droplet pinning on the GDL surface is considered by many researchers as a principal issue in the water removal process on a surface [88, 90, 101, 112, 113, 117, 118, 130, 133]. Clearly, pinning of the droplet on the GDL is not preferred for efficient PEMFC operation. The effect of contact angle of the GDL on droplet pinning and its removal was investigated without considering the effect of sidewall in a PEMFC gas channel. It was found that the forces with which the droplet is held on the GDL surface depend completely on the advancing contact angle of the droplet on the GDL [148]. For the droplet to be removed from the GDL surface, the airflow in the channel has to overcome the surface forces with

which the droplet is held on the GDL. The airflow in the channel changes the contact angle of the droplet when it starts to move. The airflow rate required to remove a droplet depends on the $\Delta\theta$ of that GDL [130]. Therefore, the advancing and receding contact angle information for evaluating the droplet pinning on the GDL surface would be beneficial.

Polverino *et al.* developed a numerical model of a droplet growing on the GDL surface to describe its behavior on the GDL surface [149]. Using a force balance, they found that droplet pinning on the GDL and oscillations of the droplet caused by the airflow in the channel affect its behavior in the PEMFC gas channel. Wang *et al.* modeled a single phase as well as a two–phase fluid flow in the gas channel [150]. They proposed that the water accumulation in the GDL is dependent on the capillary action and the molecular diffusion taking place in the through plane direction. They also mentioned that the surface tension forces acting on the droplet determines the water removal from the gas channel. In minichannels, as in the PEMFC, droplet removal from the gas channel is not only dependent on the contact angle the droplet makes with the GDL but it also depends on the advancing and receding contact angle it makes with the sidewall. Depending on the surface wettability and the airflow rate in the gas channel, different water flow patterns are observed in the PEMFC gas channels. Different flow patterns observed are droplet flow, mist flow, film flow and slug flow and are shown in Figure 2.12. It was seen that the droplet is the initial stage of water when it emerges on the GDL. It then combines with the other nearby droplets to form film or slug flow. Slug flows are more dominant at lower air and water velocities whereas film flow is most prominent

during higher air and water velocities as shown in Figure 2.13. Avoiding slug flow at lower air velocities is one of the important issues that need to be addressed to improve the PEMFC efficiency.

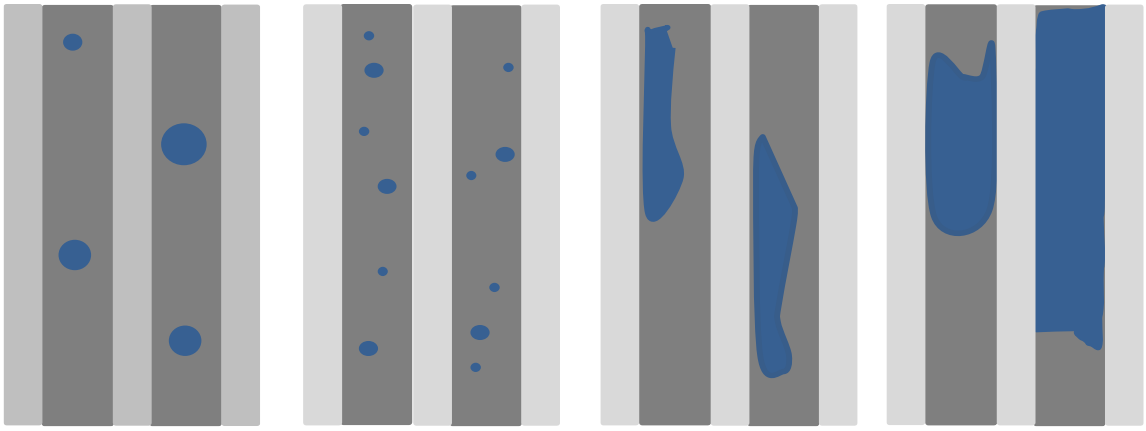

(a) **(b)** **(c)** **(d)**

Figure 2.12: Different water flow pattern observed in the PEMFC gas channels in terms of increasing flow resistance a) Droplet b) Mist c) Film d) Slug

He *et al.* developed a two–fluid model, and presented another simplified numerical model to obtain the droplet detachment diameter that takes into account the effect of surface properties of the GDL [146]. The results showed that a lower surface tension and a higher contact angle of the liquid at the GDL–channel interface are beneficial for water removal as they result in smaller droplet sizes at detachment.

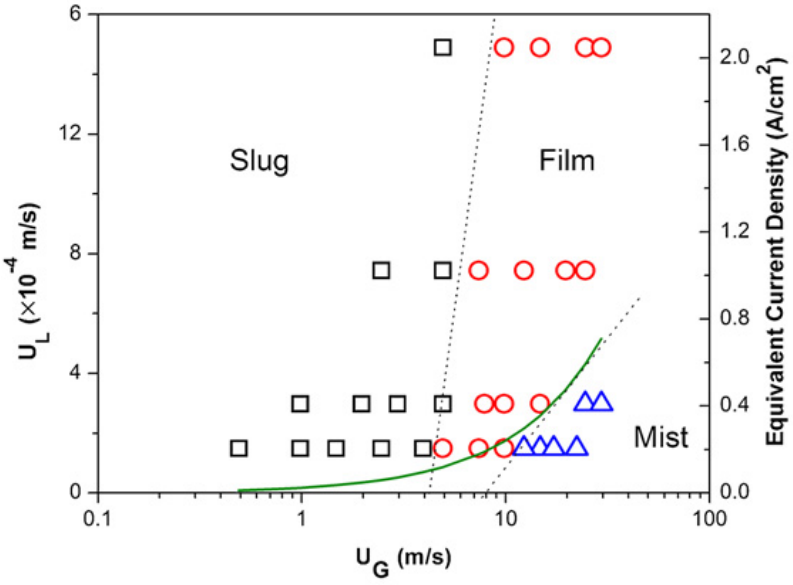

Figure 2.13: Flow pattern map for polycarbonate sidewall and MRC–105 GDL for different water (U_L) and airflow (U_G) rates. Adapted from [119].

Tuber *et al*. used a transparent material for the gas channel walls to elucidate the effect of GDL materials on water management in PEMFCs [111]. They reported that hydrophilic GDLs spread the water on the GDL surface and lead to higher water accumulation in the gas channels. This increases the pressure drop in the channel and decreases the fuel cell efficiency. Kumbur *et al*. developed a theoretical model to predict the influence of GDL hydrophobicity and $\Delta\theta$ on the mobility of the droplet and its removal [131]. It was seen that at high gas flow rates, the surface hydrophobicity of the GDL helps in the removal of the droplet. At low gas flow rates, hydrophobicity of the GDL has only a small influence on droplet removal. Chen *et al*. provided simplified models for predicting the water droplet removal from the GDL based on a macroscopic force balance [128]. They found that the droplet removal could be enhanced by increasing the flow channel length or mean gas flow velocity, in combination with

decreasing the channel height or the $\Delta\theta$, as well as increasing the hydrophobicity of the GDL.

2.6.1.2 Effect of Channel Material Properties on Droplet Removal

Earlier works reported in this area indicate that material properties of the channel sidewall have great influence on water transport in the gas channel [119, 148, 152-154]. It is seen that even though the water moved faster on a hydrophobic surface, having a hydrophobic channel sidewall is disadvantageous for gas diffusion to the catalyst layer and fuel cell performance [152]. Quan and Lai performed a numerical simulation to understand water management in gas channels and found that a hydrophilic channel surface facilitates the transport of reactant gases to the reaction sites by transporting the water along the channel edges [153]. This acts as an effective water management strategy in the gas channels. On the other hand, hydrophilic surface also increases the pressure drop due to liquid water spreading, forming slugs and leading to blockages in the channels. Zhu *et al.* conducted a numerical study to understand the effect of surface wettability on droplet removal from the gas channels [148]. They proposed that hydrophilic channel walls spread water to the channel corners leading to film flow and eventually resulting in blocking of the gas flow pathways. A similar experimental study was performed by Lu *et al.* and found that hydrophilic channels help in uniform water distribution along the GDL surface [119]. They also stated that hydrophilic gas channel walls help in creating film flow in the channel and therefore reduce the pressure drop in the channel. Zhang *et al.* also studied the effect of channel material properties and found that the hydrophilicity of the channel surface facilitates the removal of the water by

wicking it into the channel corners [120]. Therefore, from all these work, it is seen that both hydrophilic and hydrophobic channels have their own merits and demerits.

2.6.1.3 Effect of Channel Cross Sectional Geometry on Droplet Removal

It was also noted that the channel geometry has an important effect on water management in the PEMFC gas channels. Owejan *et al.* performed an *in situ* study to understand the effect of gas channel properties on water accumulation in PEMFCs [133]. They stated that triangular cross–sectional channels retained less water as compared to rectangular channels at a given current density Zhu *et al.* performed a numerical investigation on six different channel geometries to understand which geometry performs best for a PEMFC gas channel [154]. It was observed that the detachment time, detachment diameter, and removal time of water droplets were found to be lower for triangular and trapezoidal channels, and higher for rectangular and upside down trapezoid channels. It was also seen that the normalized friction factor was highest for the upside down trapezoid and lowest for the semicircle as shown in Figure 2.14(a). A similar study was performed by Lu *et al.,* and reported that sinusoidal and trapezoidal channels produce lower pressure drops in the channel compared to rectangular gas channels as shown in Figure 2.14(b) [119].

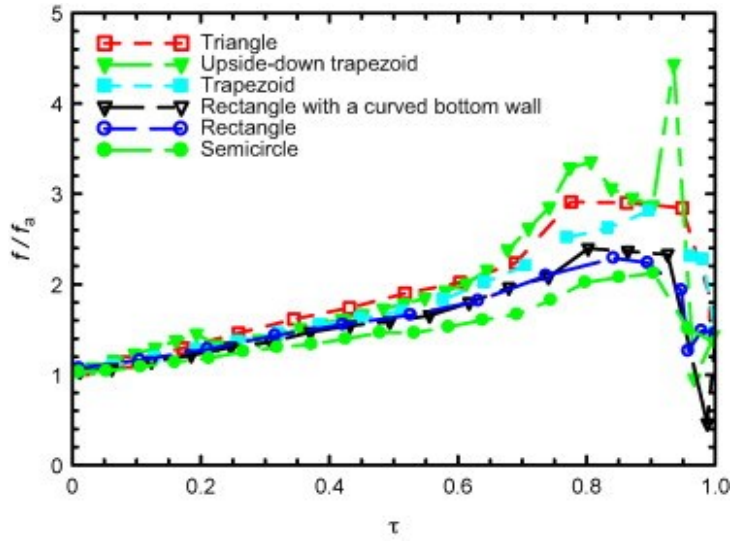

(a)

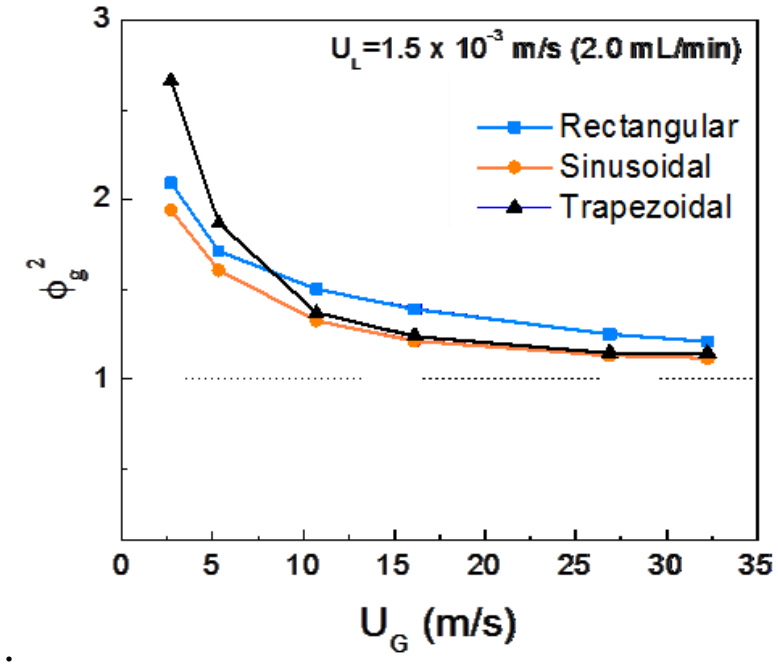

(b)

Figure 2.14: (a) Comparison of the normalized friction factor for different channel geometry as a function of time. Adapted from {Zhu, 2010 #150} (b) Comparison of the pressure drop factor in different reactant channel geometries at air velocity of 1.5 x 10^{-3} m/s. Adapted from [119].

Wang *et al*. performed two–phase flow modeling with different channel geometries and reported that water generally is trapped around the geometrical heterogeneity [150]. Akhtar *et al*. researched the effect of the aspect ratio of the gas channel on fuel cell efficiency and showed that the measured pressure drop decreases with increasing channel cross sectional area [155]. It was also seen that for the same cross sectional area but for different aspect ratio, the pressure drop was significantly different. Hence, the aspect ratio is believed to play an important role in the water transport phenomena occurring in the fuel cell.

According to most researchers, sinusoidal channels seem to perform much better in terms of water removal and pressure drop in the system. However, sinusoidal channels provide high electrical contact resistance and the stamping process of making channels is very difficult. The next best channel configuration that could be used for gas channels are the trapezoidal channels, which are cheap and easy to manufacture.

However, a trapezoidal channel can have different channel angles and the trapezoidal channel angle that provides the best-working configuration has not yet been identified. To evaluate the importance of the trapezoid channel angle, Hwang *et al.* conducted a simulation to verify the droplet dynamics at the channel corner [156]. It was seen that the effect of the sidewall became more prominent as the open angle between the sidewall and the base decreased. To investigate the water accumulation and removal processes from the gas channel at a microscopic level, Rath and Kandlikar analyzed the droplet interactions with the sidewall of a trapezoidal gas channel at different channel open angles [90]. They found that the droplet interacted with the channel walls in two

ways: the droplet exhibited either fill or not–fill conditions at the corner. They used the Concus–Finn condition to predict the corner filling behavior of the droplet [85-87]. Rath and Kandlikar also observed a droplet jumping behavior (droplet would detach from the horizontal base surface and move completely towards the sidewall of the channel) at the transition angle between corner filling and non–filling for a given material pair [89]. Transition angle is a channel open angle for a given material pair below which the droplet remained pinned to the sidewall and not fills the channel corners. However, at angles greater than the transition angle, the droplet would fill the channel corners. Das *et al.* also worked on a similar problem where they analyzed why the droplet always remains at a finite distance from the corner, referring it to as the "enclosure effect" [95]. They mentioned that the enclosure effect is dependent on the size of the droplet, surface wettability and the dynamics of the drop evaporation. The authors also noted that the evaporation flux plays an important role at the three-phase contact line of the droplet and dictates the enclosure effect.

There has been a remarkable amount of research done on the water management issue in PEMFCs. However, there is still a need for thorough understanding of the droplet behavior at the channel corners to understand the intricate details that affect the droplet pinning and water removal process inside the gas channels. Rath and Kandlikar studied the droplet–sidewall interactions on a polycarbonate sidewall [90]. However, the research was performed in a static condition where no airflow conditions in the system were analyzed. On the other hand, in an actual fuel cell, airflow in the gas channel is a very important criterion, which affects liquid water removal from the channel. Therefore, the

work presented in this dissertation focuses on the behavior of the droplet and its interaction with the channel sidewall in the presence of gas flow. This work corresponds to the actual droplet behavior that prevails in a PEMFC and will help in gaining better insight into droplet dynamics, droplet pinning on the GDL and channel wall surface, and the effect of gas flow on droplet–channel wall interactions. This work will also help in providing guidance in designing the gas channel configuration for PEMFCs such that it will reduce water accumulation in the gas channel and decrease gas transport resistance in the PEMFC's channels. In this work, effect of different channel wall material and GDL materials would be studied to get an in-depth knowledge on how these materials affect the droplet removal from a trapezoidal channel work at different air velocities. The flow pattern transition of the liquid flow in the gas channel would also be mapped as a function of channel open angle, different GDL and channel wall materials and air velocity inside the channel.

Chapter 3 Experimental Setup

3.1 Designing of *Ex Situ* Setup

The *ex situ* setup used in the present study is shown in Figure 3.1. The test section consists of different plates mounted on top of each other to form the single channel experimental setup. The test setup consists of a base plate, which holds the GDL on top of it. An inlet for the water droplet was made on the base plate near the channel end to allow the water to emerge onto the GDL and visualize the droplet interactions with the sidewall of the channel. The channel sidewall consists different open angles (30°,45°, 50°, 60°, 90°) machined on the sidewall plates. These plates were placed on top of the GDL layer. The top wall was placed above the sidewall plates to form a complete 100 mm long channel.

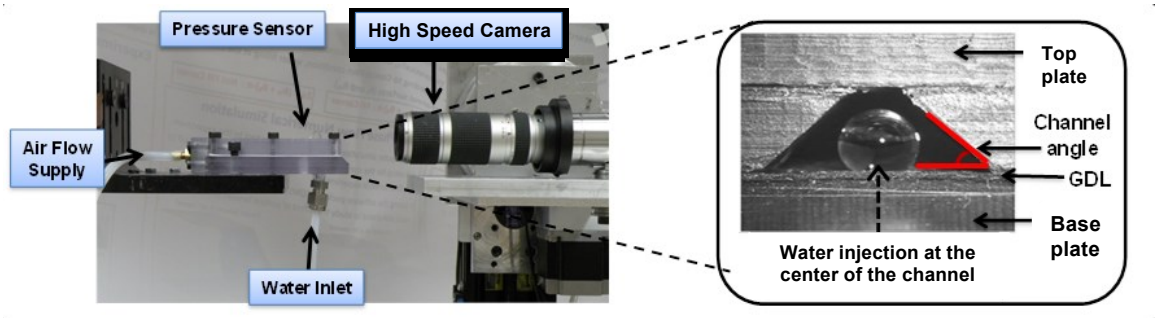

Figure 3.1: Experimental test set up used for visualization of the droplet dynamics inside the gas channel.

It was demonstrated previously in the literature that the material roughness influences the contact angle measurements on a given surface [30, 34, 49, 51, 65, 84,

157]. To avoid such discrepancies in our experiments, the channel walls were smoothed using emery cloth after machining. The surface roughness of the sidewalls was measured using a Confocal Laser Scanning Microscope (CLSM), and the corresponding images of the different channel walls and the GDL samples used in this study are shown in Figure 3.2. The surface roughness factor for the different sidewall materials was confirmed to be less than 900 nm from the image slices and is summarized in Table I.

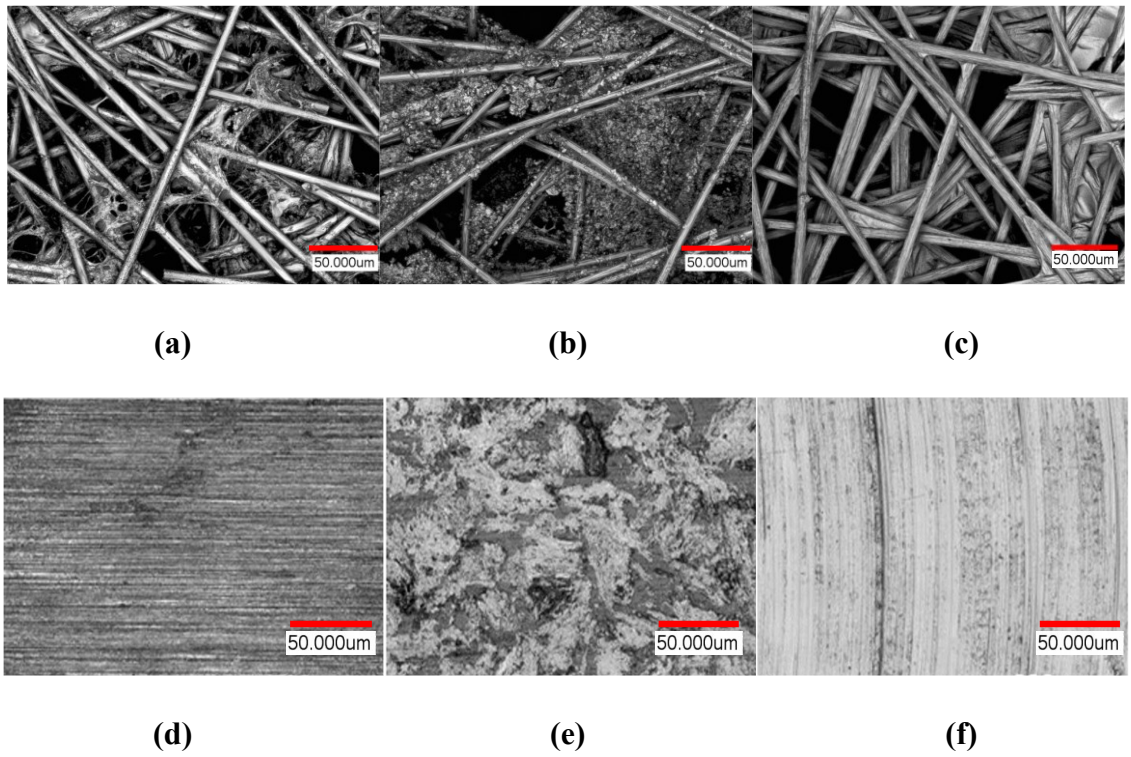

Figure 3.2: Confocal laser scanning microscope (CLSM) images of different GDL and channel wall materials (a) MRC–105 (b) SGL–25BC (c) TGP–H–060 (d) Cu-110 (e) Graphite Composite (f) SS-2205

In our experiments, we also studied the effect of different channel wall and GDL material effect on the droplet dynamics inside the gas channel. Stainless steel (SS–2205), copper (Cu–110) and graphite composite are a few of the most commonly used materials

for the bipolar plates in the PEMFCs. Therefore, all three of these channel sidewall materials were tested. Along with this, different GDL materials such as SGL–25BC, MRC–105 with 6% PTFE and TGP–H–060 with 6% PTFE were tested to understand the effect of GDL material on droplet removal from the PEMFC gas channel. To evaluate the performance difference due to GDL aging or deterioration, MRC–105 that was run for 40 and 125 hours in *in situ* experiment previously was compared with a fresh GDL sample performance [119].

Table I: Surface roughness measured for the different sidewall materials used.

Material	Surface Roughness (Ra)
Copper (Cu–110)	554 nm
Graphite Composite	873 nm
Stainless Steel (SS–2205)	558 nm
Polycarbonate (Lexan^{TM})	666 nm

3.2 Experimentation

The *ex situ* experimental setup consists of four different sections connected to it as shown in Figure 3.3. The different sections are as following (1) water system (2) airflow system (3) visualization section and (4) pressure drop measuring system. Water section consists of water stream coming from the main line that was passed through deionized water generator to remove the ions from the water. The deionized water was introduced on the GDL surface using a syringe pump from Harvard Apparatus (Model 11

Plus). A low water flow rate of 0.005 ml/min was used for the experiments, which corresponds to a current density of 0.3 A/cm^2 for an active area of 2.9 cm^2. The calculation for the superficial water flow rate corresponding to the current density in the PEMFC system is shown in Appendix I. Experiments were also performed with a water inlet flow rate of 0.05 ml/min, which corresponded to the water generation rate for a current density of 3 A/cm^2 for an active area of 2.9 cm^2. There was no difference in the observed droplet behavior between the two water flow rates used. Therefore, to minimize the experimental time, water flow rate of 0.05 ml/min was chosen for all the experiments performed with 3 mm hydraulic diameter channels.

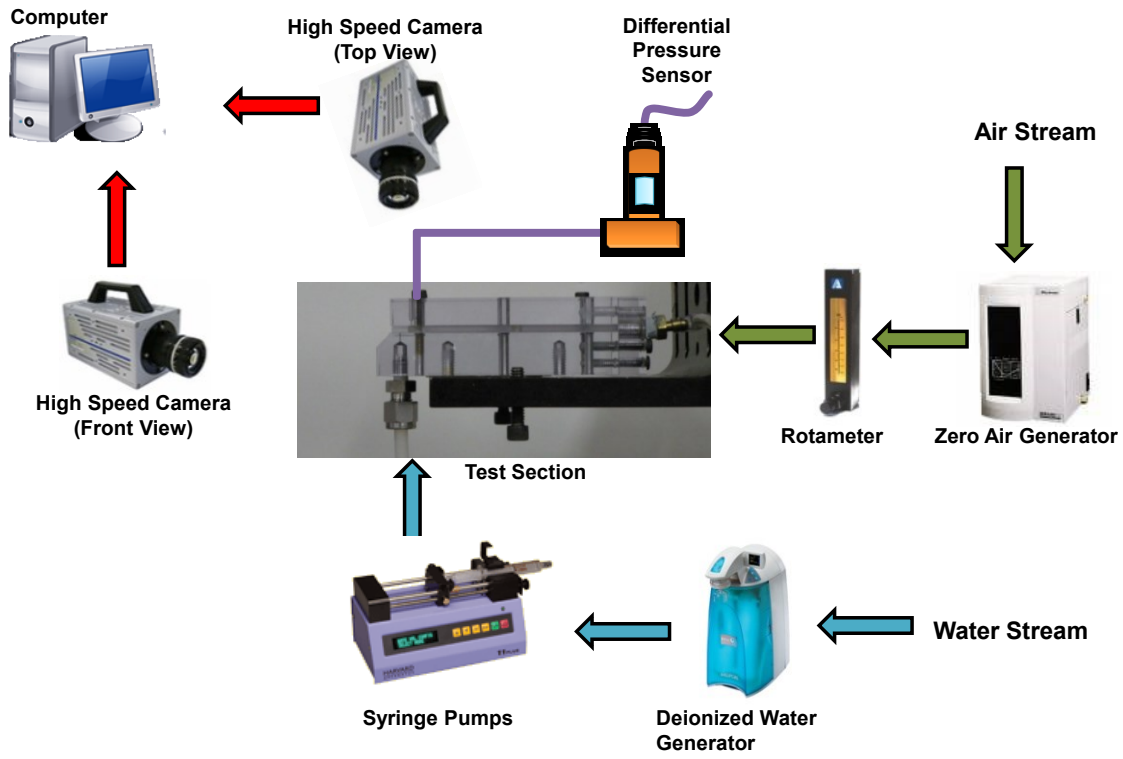

Figure 3.3: Experimental test setup with different control units

The airflow into the gas channel from the Parker Balston HPZA 18000 Zero Air Generator was via an air manifold that was attached to the system at the rear end. The gas flow was controlled using a rotameter, which was attached just before the air manifold. Experiments were performed by varying the air velocity inside the channel. As the channel sizes used were larger than real world fuel cell dimensions, the airflow rates used in the system were matched according to the air velocities (v) observed in the real fuel cell used for automobile application. The superficial air velocities between 0.2 and 2.4 m/s were simulated for a range of current densities from 0.1 to 1.1 A/cm^2 for stoich of 1 and 2. These values would correspond to an active area of 50 cm^2 in a typical fuel cell that meets the Department of Energy specifications [133]. The superficial air velocity calculation corresponding to the current density in the PEMFC system is shown in Appendix I. The relationship between the air velocities used in this experiment corresponding to the actual current densities for a single channel of dimension 183 mm long, 0.4 mm deep and 0.7 mm wide is shown in Table II.

The visualization section consists of the high-speed video recordings to visualize the droplet dynamics in the gas channel. High–speed videos were recorded using the Keyence VW–6000 high–speed digital camera. The droplet dynamics with the sidewall were captured at a frame rate of 250 fps. Videos were obtained from front as well as top view to understand the droplet-corner interaction and the flow pattern transition observed inside the gas channel as a function of channel angle, air velocity and material properties (base and wall contact angle). During experimentation, the air velocity was set to a desired value and the droplet was allowed to grow on the GDL surface. As the droplet

continued to grow, it would encounter the channel sidewall, similar to the process that would occur in a PEMFC gas channel. This process was captured and post processed using the Keyence Motion Analyzer software at 3X magnification. The uncertainty in the contact angle measurement was determined to be within the range of ± 2°.

Table II: Air velocities with corresponding current densities calculated for a channel active area of 18.4 cm^2

Current Density (A/cm^2)	Stoichiometry	Air Velocities (m/s)
0.1	1	0.24
0.1	2	0.48
0.3	1	0.73
0.3	2	1.46
0.5	1	1.21
0.5	2	2.43
0.7	1	1.70
0.9	1	2.18
1.1	1	2.67

Last section in the experimentation is the pressure drop measuring system. Pressure tap was made on the top plate of the test setup just before the droplet emergence location to measure the instantaneous pressure drop across the droplet in the system. Pressure drop data across the droplet was measured using a Honeywell FWD differential pressure sensor (0 – 1 psi range) connected via pressure tap. The accuracy of the pressure sensor was ± 0.25% of full–scale reading. A LabVIEW program was used to record the

pressure drop across the droplet. A snapshot of the front panel of the program and the connection diagram is shown in Figure 3.4. All the data measured were post processed and are discussed in detail in the results section (Section 4). The entire test section was mounted on top of a test stand on a vibration isolation table to mitigate any discrepancies due to vibrations.

The thickness of the GDL used for the experiments were approximately 245 μm. A 178 μm thick PTFE gasket was used to ensure the appropriate compression under the applied load. In the GDL, a preferential pore of 180 – 200 μm was made for the droplet to appear on the surface at a desired location of 5 mm away from the channel exit to provide easier visualization access and capture the droplet dynamics. Since the droplet size introduced in the channel before it contacted the sidewall was much larger than the inlet pore size, the effect of pore diameter on the droplet interaction with the gas channel walls can be neglected.

For different channel angles used in our study, the channel cross section was varied in order to maintain a constant hydraulic diameter of 3 mm. The channel sizes used were slightly larger than the actual fuel cell dimensions to provide visible access to the droplet and its behavior inside the channel. Further work on smaller channels with cross section of 0.4 x 0.7 mm was performed later to understand how the scaling of the system affects the water droplet behavior inside the PEMFC gas channel, the results of which are discussed in detail in Section 4.7.

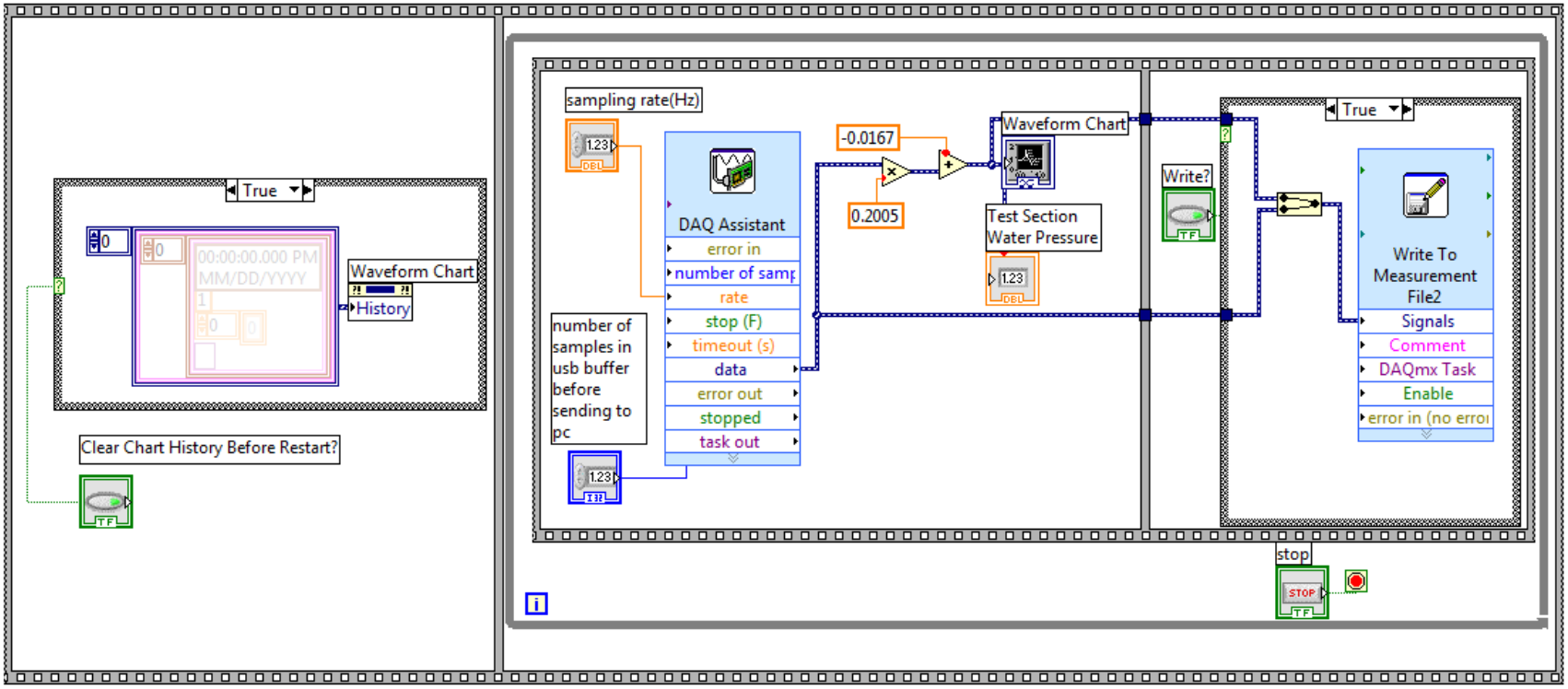
True
0
0
00:00:00.000 PM
MM/DD/YYYY
1
0
0
Waveform Chart
History
Clear Chart History Before Restart?
sampling rate(Hz)
1.23
DBL
DAQ Assistant
error in
number of samp
rate
stop (F)
timeout (s)
data
error out
stopped
task out
number of samples in usb buffer before sending to pc
1.23
I32
-0.0167
0.2005
Waveform Chart
Test Section Water Pressure
1.23
DBL
Write?
TF
True
Write To Measurement File2
Signals
Comment
DAQmx Task
Enable
error in (no erro
stop
STOP
TF

(a)

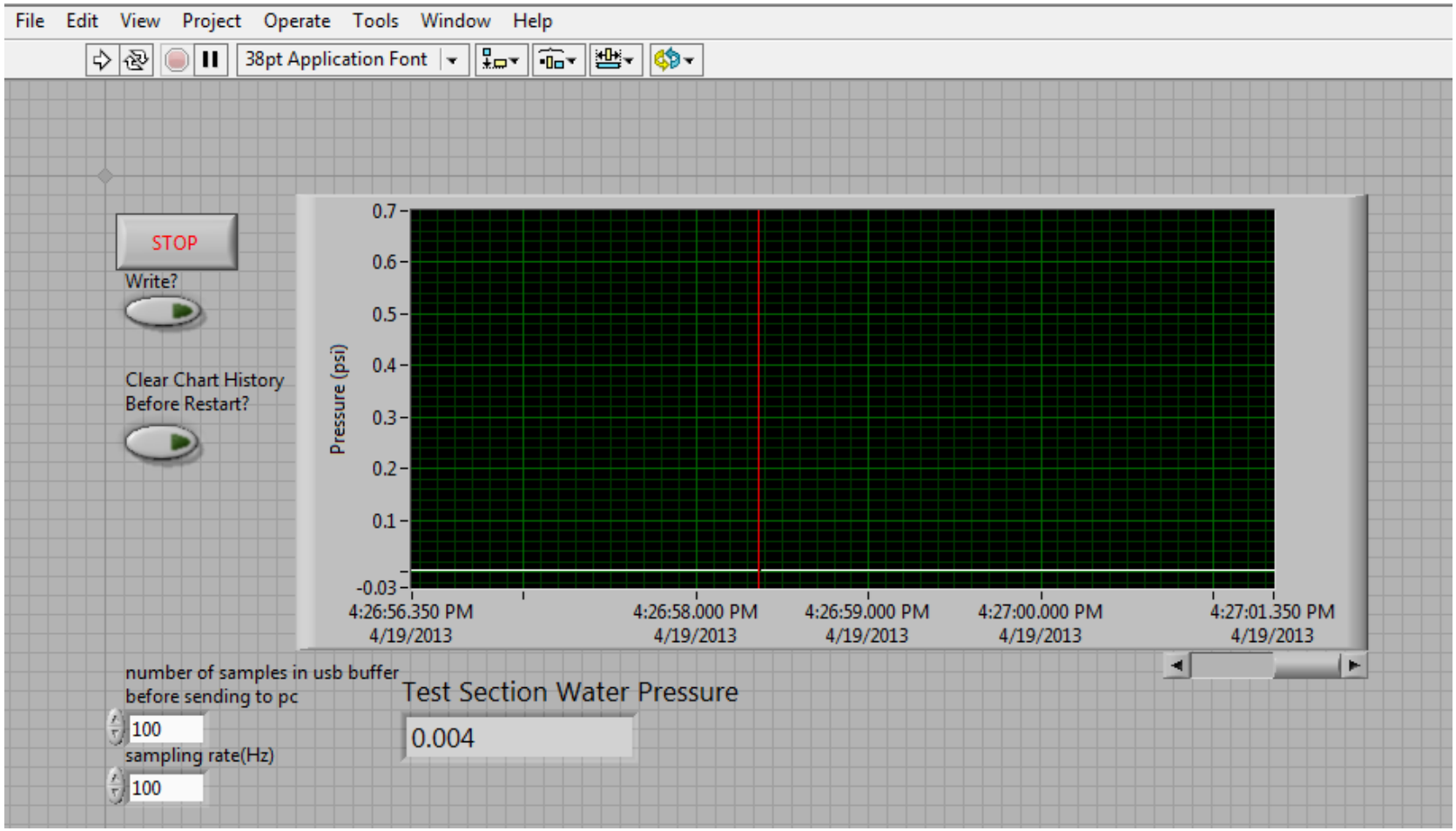

(b)

Figure 3.4: (a) Image of the LabVIEW connection diagram used for the pressure drop measurement (b) Front panel view of the pressure drop measurement.

Prior to determining the desired angular configuration of the trapezoid channel for efficient water removal from the PEMFC, it is necessary and important to measure the $\Delta\theta$ of the channel material used for the study. In order to quantify the $\Delta\theta$, the advancing contact angle θ_A as well as the receding contact angle θ_R were measured for all the sidewall and base GDL materials. The contact angle measurement was done using the VCA Optima Surface Analysis System, which uses sessile drop method to measure the contact angles, and the corresponding measurements for different GDL and sidewall materials are given in Table III.

Table III: Static advancing, receding contact angles and contact angle hysteresis of sidewall and GDL materials

Material	Advancing Contact Angle (θ_A)	Receding Contact Angle (θ_R)	Contact Angle Hysteresis ($\Delta\theta_{hys}$)
MRC–105 with 6% PTFE	148	138	10
TGP–H–060 with 6% PTFE	145	127	17
SGL–25BC	148	136	12
40 hours MRC–105 GDL	144	136	8
125 hours MRC–105 GDL	132	123	9
Polycarbonate	86	61	25
Copper (Cu–110)	80	53	27
Graphite Composite	84	34	50
Stainless Steel (SS–2205)	81	60	19

In order to analyze the droplet dynamics, the contact angles the droplet makes with the sidewall and the base GDL are required. The Figure 3.5 shows the different contact angles the droplet makes with the sidewall and the base. Droplet pinning on the surface is dependent on the lower contact line (LCL) and inner contact line (ICL) [158]. Near the channel corner, θ_W is the angle made by the LCL of the droplet with the sidewall and θ_B is the angle made by the ICL of the droplet with the base. When there is airflow in the system, the contact angle made by the droplet on the base and the channel wall cannot be defined by the static advancing and receding contact angles. The contact angle on the surface differs at every instant of time due to oscillation in the droplet. Therefore, the instantaneous dynamic contact angles (IDCA) the droplet made with the channel wall and the GDL were measured on each frame of the video that was captured during experimentation in the presence of airflow. The IDCA of a material is the measurement of advancing contact angles made by a droplet at a given instant of time on a given surface in the presence of airflow in the system.

These angles determine the droplet filling criteria of the channel corner where the sidewall and base meet. In PEMFCs, once the droplet fills the channel corner, it acts as a viable pinning site for other successive droplets that emerge onto the channel. These droplets will merge with each other, and eventually will lead to droplet accumulation and channel flooding on the GDL surface. Therefore, it is very important to prevent the droplet from filling the corners of the channel.

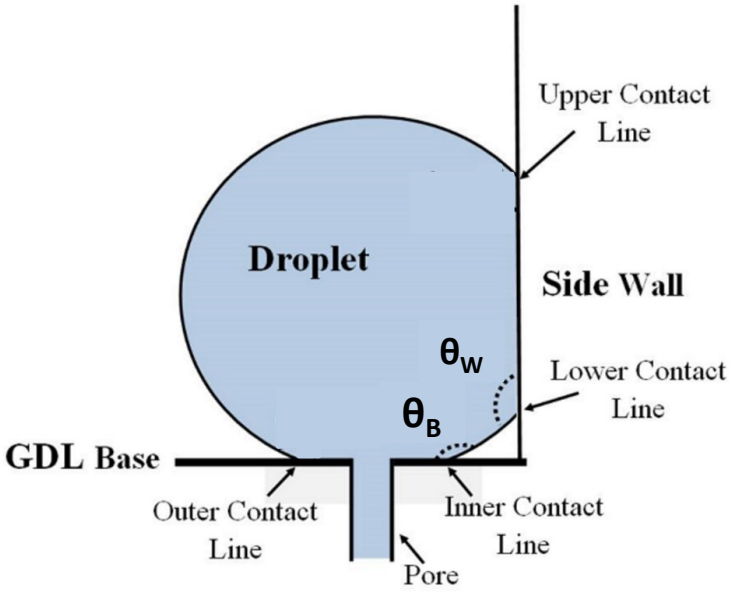

Figure 3.5: Image of a droplet touching the base GDL and the sidewall of a channel. This shows the different contact lines the droplet makes with the different surfaces. Adapted from [90]

As mentioned earlier, the Concus–Finn condition was used to predict the liquid behavior in the corner of a channel. They used the 2D graph as shown in Figure 2.8(b) for predicting the droplet behavior in the corner of the channel. To make the plots simple to understand for our particular application, instead of drawing the whole box to indicate the filling region as shown by Concus–Finn in their work, only the upper limit line of the box was used. This would imply that for any contact angle points falling below the Concus–Finn limit (CFL) line or transition point, the droplet would move towards the corner of the channel and would ultimately fill the corner of the channel. If the IDCA point falls above the CFL line, then the droplet would remain pinned to the sidewall and not move towards the channel corner. Therefore, using the static contact angles, the CFL for non–filling condition of the channel corners is predicted by the Eq. 3.2

$$2\alpha \leq (\theta_B + \theta_W) - \pi \quad [3.2]$$

where θ_B is the advancing contact angle for the base material and θ_W is the advancing contact angle for the sidewall.

The theoretical estimation of the transition angle from non–filling to filling condition for the material pairs used in this work is shown in Table IV. It was found from this data that all material combinations had the transition angles near 50° (48° – 53°). According to the Concus–Finn condition, the open angles below the transition angle will not fill the channel corners and for any open angles above the transition angle, the droplet will fill the channel corners.

Table IV: Transition angles from non–filling to filling for a given material pair

Material Pair	Transition Angles
MRC–105 – Polycarbonate	53°
MRC–105 – Copper (Cu–110)	48°
MRC–105 – Graphite	52°
MRC–105 – Stainless Steel (SS–2205)	49°
TGP–H–060 – Polycarbonate	50°
SGL–25BC– Polycarbonate	51°
40 hours MRC–105– Polycarbonate	49°
125 hours MRC–105 – Polycarbonate	37°

Chapter 4 Experimental Results

High–speed videos at frame rates of 250 fps were captured in order to see the droplet dynamic behavior in the gas channel with different trapezoidal angular configurations. Frame by frame analysis was performed on the videos to estimate the IDCA and the movement of the droplet with airflow. Pressure drop data was recorded for all the experiments performed and processed to evaluate the effect of different parameters (channel open angle, superficial air velocity, channel material, GDL material, GDL degradation, channel scaling and droplet inlet location) on the droplet dynamics in the system. More than 500 experimental cycles were performed and analyzed. Corner filling and non-filling behavior was analyzed for all the experiments performed. One of the major observations was that the IDCA made by the droplet on the sidewall and the GDL was outside the range of the static advancing and receding contact angles. The airflow causes oscillations in the droplet interface introducing significant variations in the associated dynamic contact angles.

4.1 Effect of Channel Wall Angle

To evaluate the effect of the channel trapezoid angle on the droplet dynamics, experiments were performed with five different sidewall angles (30°, 45°, 50°,60°, 90°) for air velocities of 0.4 and 2 m/s. Figure 4.1 shows the image sequence of the video captured for the droplet behavior at 30° for air velocity of 0.4 m/s. The video was

captured for the whole sequence of droplet dynamics i.e. from droplet growth until the droplet was removed from the channel. It was observed that a droplet in a channel undergoes a series of transitions as mentioned in Figure 4.1 before it is removed from the channel. The transition the droplet undergoes in all the channel is as follows.

The droplet emerges on the GDL surface and continues to grow until it touches the top wall and spreads on the channel sidewall. Once the droplet spreads in the channel, it blocks the channel almost completely until the pressure in the channel increases so much that the droplet is removed. The droplet starts to move on the GDL and the channel surface along the airflow direction only when the pressure force from the air exceeds the surface tensions forces that are holding the droplet on the GDL. Once the droplet starts to move on the GDL surface it eventually gets pushed out of the channel. The whole sequence of droplet behavior inside the gas channel was common for all the trapezoid channel angles used but the only difference that was observed was in the corner filling and non–filling behavior with different open angles.

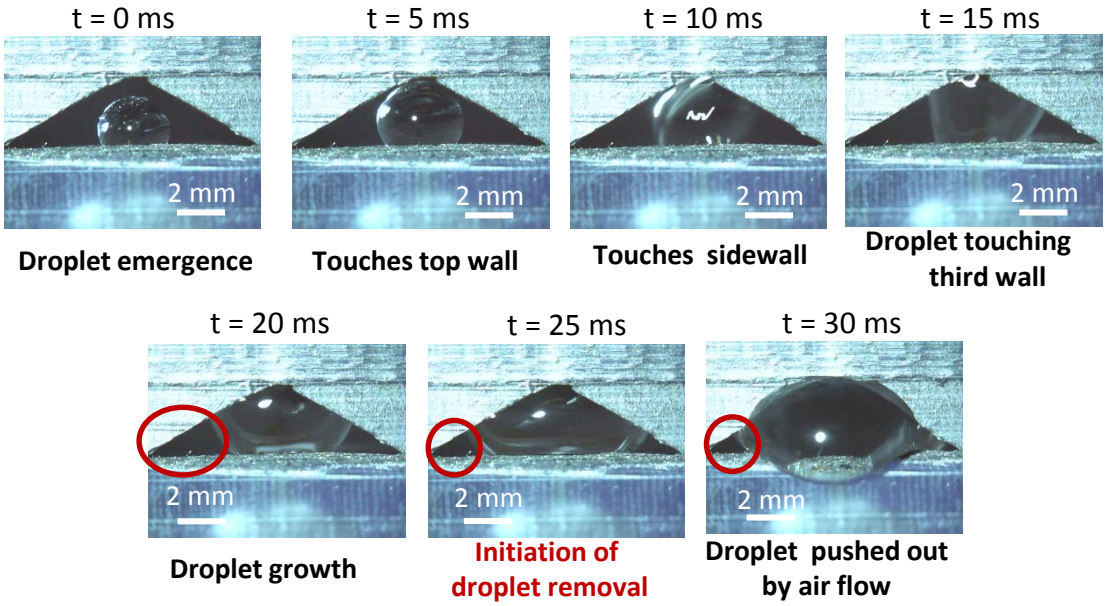

Figure 4.1: Sequence image of a single droplet behavior inside a 30° open angle channel made of polycarbonate sidewall and GDL base with 0.4 m/s air velocity introduced into the channel from the air manifold. The red circle in the image shows that the droplet does not fill the corner of the channel as the droplet makes its exit from the channel.

In terms of corner filling and non–filling behavior, in a 30° channel the droplet did not fill the channel corners. Similar behavior was observed for the 45° channel as well. However, for 60° and 90° channel, the droplet filled the channel corner. Figure 4.2 shows the sequence image of the video for a single droplet behavior in 60° channel. All these video images are recorded for a longer time span to visualize the successive droplet emergence and departure but for simplicity in Figure 4.2, sequence images of only one droplet emergence and departure have been shown.

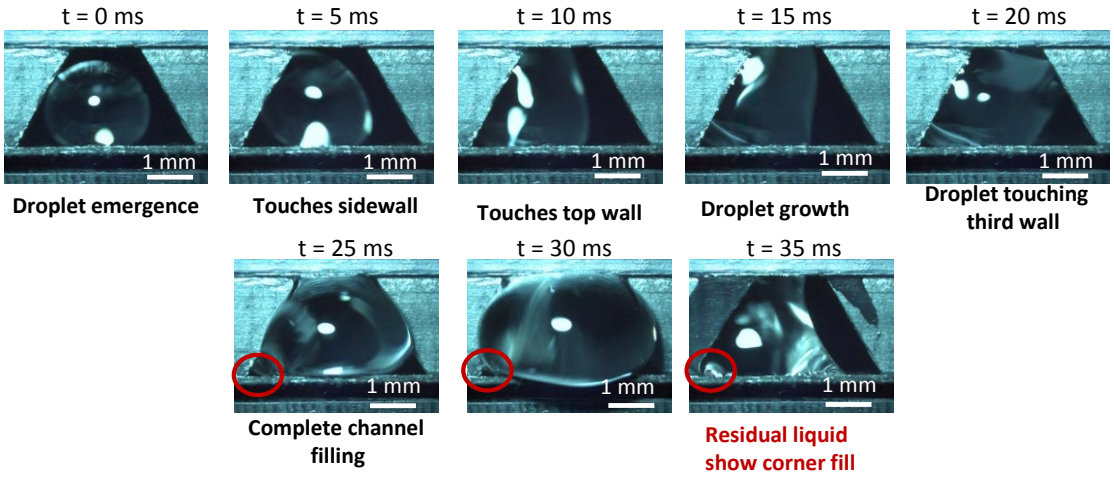

Figure 4.2: Sequence image for the droplet dynamics in a 60° open angle channel made of a polycarbonate sidewall and GDL base with 0.4 m/s air velocity introduced into the channel from the air manifold. The red circle in the image shows that the corner of the channel is completely filled.

To evaluate the experimental observations using Concus–Finn condition, the IDCA values the droplet made with the sidewall and the GDL were measured from the video and were plotted against each other. IDCA values were obtained by measuring the contact angle θ_W and θ_B the droplet made with the wall and the base respectively for each video frame until it filled the channel corner. This was extended for the entire range of open angles tested. The IDCA (θ_W and θ_B) data obtained from the experiments were plotted with the theoretical CFL line as shown in Figure 4.3. In the plots, even if one of the IDCA point fell below the CFL line, then the droplet would not remain pinned to the sidewall. Instead, it would slowly move towards the channel corner and fill it.

The IDCA plot for 30° and 45° channels is shown in Figure 4.3(a), and 60° and 90° channels is shown in Figure 4.3(b). In these plots, the solid line shows the theoretical

CFL for a particular channel angle. The dotted line for $\Delta\theta_B$ and $\Delta\theta_W$ shows the static $\Delta\theta$ observed for the base GDL and the sidewall respectively. The filled boxes in the plot shows the filling contact angle, i.e. the contact angle values that would attract the droplet towards the corner of the channel and the open boxes shows the non–filling dynamic contact angle values which would not lead to corner filling scenario. Figure 4.3 clearly shows that the IDCA points for the 30° and 45° channels obtained from the experimental results fell above the CFL line. This indicates that the droplet would not fill the corner, which matched the experimental results observed from the videos. For the 60° and 90° channels, the contact angle points fell below the CFL line showing that the corner should be filled. The observed results were similar for all the air velocities used in the study. These results were also consistent with the findings shown by Rath and Kandlikar for a static condition (no airflow rate introduced in the system) [89, 90]. However, for the 50° channel, which is near the transition point for corner filling behavior according to the Concus–Finn condition, the experimental results showed different behavior at different air velocities [94]. These results are discussed in more detail in the next section (Section 4.2).

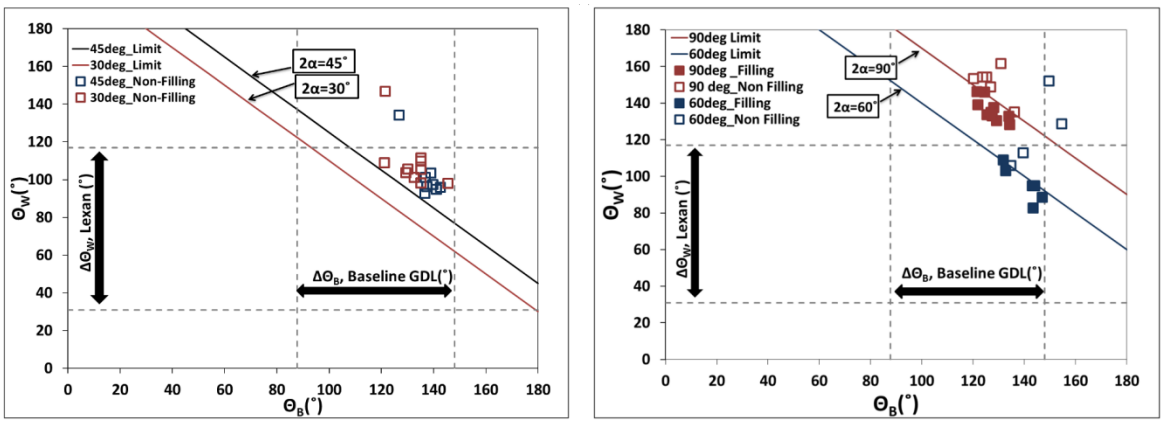

(a) **(b)**

Figure 4.3: Dynamic contact angles made by the droplet at an air velocity of 0.4 m/s with the sidewall and the base GDL plotted against each other along with the theoretical CFL line shown by solid line. The solid boxes in the plot show the angles that lead to the droplet filling the corner of the channel and the open box shows the angle showing pinning of the droplet. For channel angle 30° and 45° the corner of the channel is not filled and for channel angles 60° and 90° the corner of the channel is filled.

4.2 Effect of Superficial Air Velocities

To understand the effect of airflow on the droplet behavior, similar experiments as mentioned above were conducted by keeping the channel angle constant and by varying the air velocity between 0.2 and 2 m/s. It was seen that for a 90° channel, the droplet filled the channel corners for all air velocities. Similar results were found for a 60° channel as well. For 30° and 45° channel, the corners were not filled for any air velocities. Apart from corner filling and non–filling behavior for different channel open angles, there were some distinct differences observed in the droplet dynamics between lower and higher air velocities in the channel. These differences are listed below:

1) At lower air velocities between 0.2 and 1 m/s, the droplet blocked the channel completely (slug flow) before the air pushed the droplet out of the channel, whereas for higher air velocities between 1.1 and 1.6 m/s, the droplet was pushed out of the channel well before it blocked the channel completely (film flow).

2) At much higher air velocities between 1.7 and 2.4 m/s, the droplet was removed from the channel well before it even touched the channel walls. More in depth theoretical analysis is performed on this behavior in the theoretical analysis section (Section 5) to understand the minimum velocity and minimum pressure force required in the channel to remove the droplet from the channel before it touches the channel wall.

3) At lower air velocities, the droplet first translated in the direction of the sidewall, which eventually led to a filling or non–filling condition depending upon the trapezoid channel angle, and then moved in the direction of the airflow to be removed from the channel. At higher air velocities, the droplet first translated in the airflow direction and later moved on to the sidewall.

4) The time required for the droplet to be removed from the channel from when it appears on the top of the GDL was high for lower air velocities (15 – 20 sec), while using higher air velocities cut the droplet removal time almost in half (5 – 10 sec).

Another significant effect that was observed only for the 50° channel was that the droplet filling and non–filling of the channel corner was dependent on the air velocity. At lower air velocities between 0.2 and 0.4 m/s, the droplet filled the channel corner as

shown in Figure 4.4, whereas at higher air velocities (0.5 m/s onwards), the droplet did not fill the channel corner as shown in Figure 4.5.

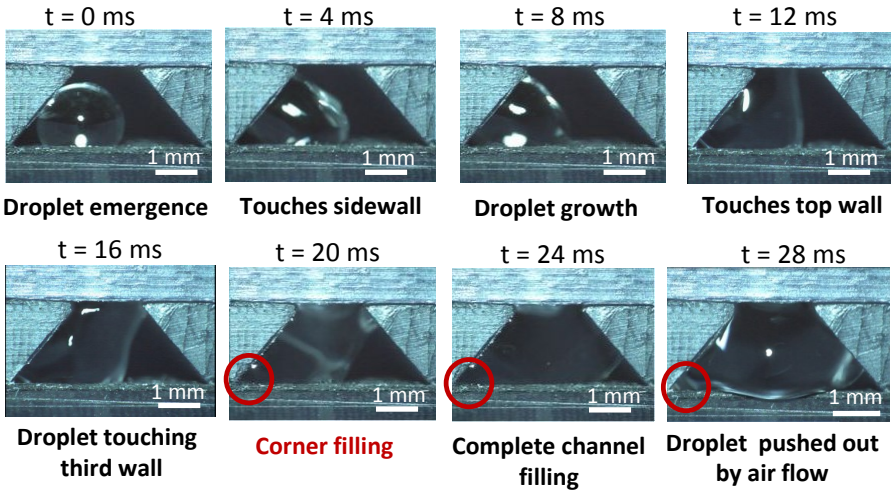

Figure 4.4: Sequence image of the droplet interaction with the polycarbonate sidewall and GDL base in a 50° open angle channel with 0.4 m/s air velocity introduced into the channel. Red circle in the image shows the corner filling of the channel by the droplet.

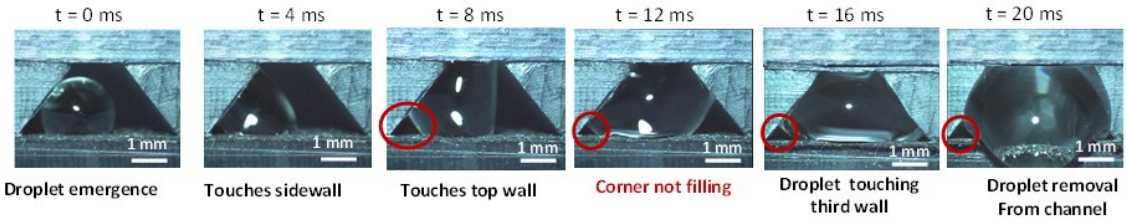

Figure 4.5: Sequence image of the droplet interaction with the polycarbonate sidewall and GDL base in a 50° open angle channel with 1.6 m/s air velocity introduced into the channel. Red circle in the image shows that the droplet does not fill the corner of the channel.

To evaluate the actual cause for this behavior, the IDCAs obtained from the experimental videos before filling the channel corners were plotted along with the theoretical CFL as shown in Figure 4.6. It was seen that for lower air velocities, the

IDCA made with the sidewall and the base GDL measured from the video were found to lie below the CFL line implying that the droplet should fill the channel corner, while for higher air velocities, the contact angle points were above the CFL line. These results were similar to what was observed from the experimental videos. From these observations, it can be inferred that the air velocities inside the channel manipulates the droplet and oscillates it before it contacts the sidewall. For open angles closer to transition angle, these oscillations in the droplet drive the channel corner filling and non–filling behavior at different air velocities. According to the static advancing contact angle values for the GDL and polycarbonate sidewall, the transition angle is 53°. Experimentally, a 50° channel marks the transition point from non–filling to filling.

To further characterize the effect of airflow on the droplet in different channel angular configurations, the length of the sidewall (polycarbonate length) and the length of the GDL (GDL length) from the corner of the channel which were left non–wetted by the droplet for a given instant of time, as shown in Figure 4.7, were also measured and plotted. This will provide the amount of clearance length left open near the channel corner when the droplet is pinned onto the surface. This plot will also give insight on the time required by the droplet to fill the channel corner in a particular angular configuration.

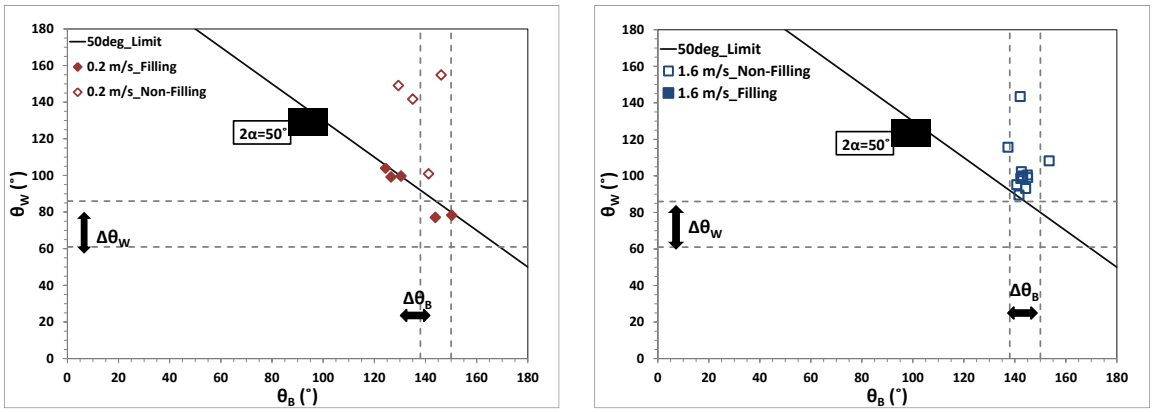

(a) **(b)**

Figure 4.6: Dynamic contact angles made by the droplet in a 50° open angle channel made up of polycarbonate sidewall and the base GDL plotted against each other along with the theoretical CFL line shown by solid line at different air velocities a) 0.2 m/s and b) 1.6 m/s

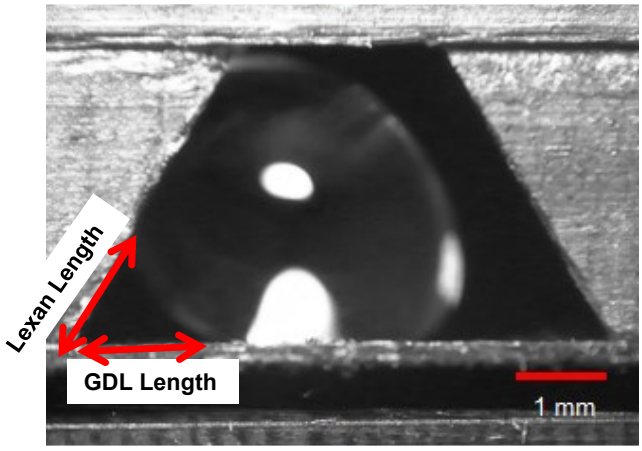

Figure 4.7: Length of the sidewall (Lexan length) and the length of the GDL (GDL length) from the corner of the channel which was left non–wetted by the droplet at a given instant of time

The length measurement was done manually using Keyence Motion Analyzer software by going through each frame in the video and measuring the wetted and non–wetted length values for a particular time. Figure 4.8 shows the length of the non–wetted

sidewall and GDL surface for different channel angles plotted against time. It was seen from the plot that the droplet pinning to the channel wall and showing enclosure effect was prominent for a 45° channel as shown in Figure 4.8(a). Here the non–wetted length remained constant after certain time. This indicates that the droplet pinning phenomenon occurred on the surface, which would not allow the droplet to move towards the channel corner to fill it. Once the droplet is pinned to the sidewall from the LCL, the upper contact line (UCL) of the droplet as shown in Figure 3.5, starts to move more rapidly to block the channel and eventually getting removed from the channel. It was also seen that the clearance length near the channel corner was dependent on the air velocity introduced in the channel. The clearance length was larger for higher air velocities than lower air velocities.

For 60° and 90° channels, the non–wetted length of the wall near the LCL became zero after 35 ms displaying the corner filling condition. This sequence was similar for all airflow rates studied. Droplet filling in the channel corner took place rapidly in these channels. When the same experiment was performed for the 50° channel, it was observed that for lower air velocities the non–wetted length of the wall approached to zero at 27 ms whereas for higher air velocities the non–wetted length of the wall never reached zero. This corresponds to the non–filling criteria in the channel where the droplet remains pinned to the sidewall and does not move forward on the wall surface to fill the corner. It can also be seen from the plot that the clearance length for the 50° channel at 1.6 m/s air velocity was lower than that in the 45° channel. Similarly, the clearance height at 1.6 m/s

air velocity in a 45° channel was smaller than that in the 30° channel. Therefore, it can be concluded that as the channel angle goes down the clearance length of the channel wall increases for non–filling channel corners.

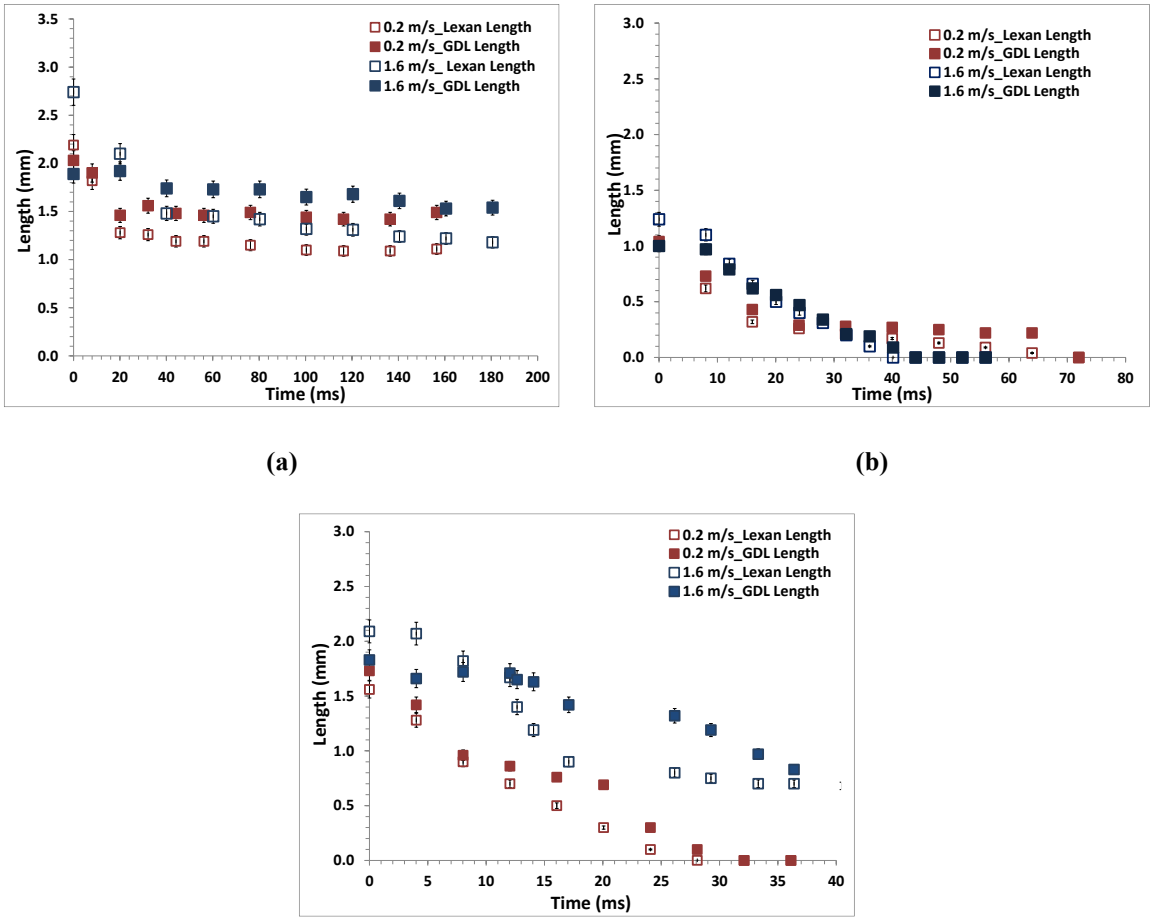

Figure 4.8: Plot of non–wetted length of GDL and sidewall from the corner of the channel for different channel angles as a function of air velocity. (a) 45° channel where the droplet is pinned to the channel sidewall and does not fill the corner of the channel for any air velocity (b) 60° channel where the droplet does not pin to the channel sidewall and fills the corner of the channel for all air flow rates (c) 50° channel where for lower air flow rates the droplet fills the corner of the channel (shown by red box) and for higher flow rate the droplet remains pinned to the sidewall and doesn't fill the channel corner (shown by blue boxes).

To understand how the airflow in the system produces oscillations in the droplet that affect the dynamic contact angle it makes with the wall and base of the PEMFC gas channel, the IDCA point just before the droplet started to move in the gas channel due to airflow was measured. Figure 4.9 shows the IDCA plot of a MRC–105 GDL and polycarbonate wall for different air velocities plotted against time for a 50° channel.

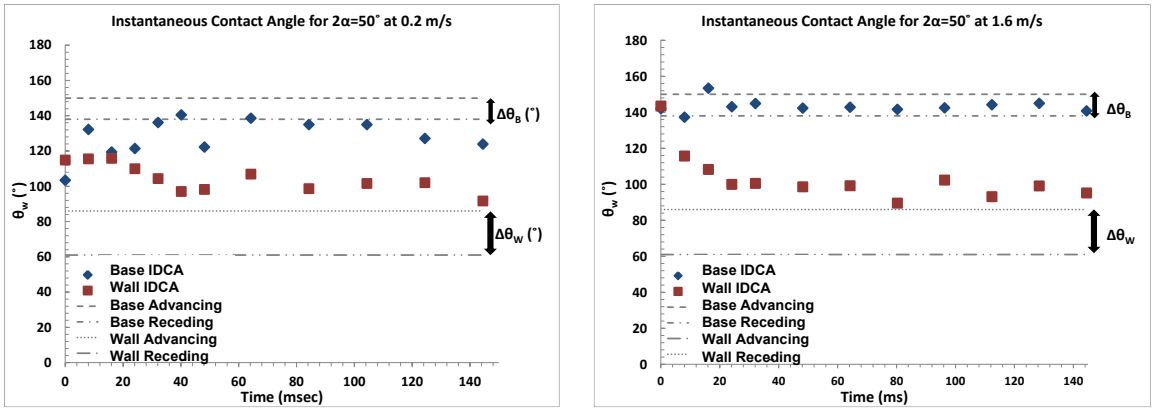

(a) **(b)**

Figure 4.9: IDCA plot of a droplet on the MRC–105 GDL and polycarbonate sidewall in a 50° channel at air velocities of (a) 0.2 m/s (b) 1.6 m/s. it is seen from the plot that the IDCA of the base wall are within the *Δθ* range however, the IDCA of sidewall is above the *Δθ* value. This shows that the air velocity in the channel produces oscillations in the droplet, which changes the contact angle the droplet makes with the wall.

It can be seen from the plot that the advancing contact angle value changes very drastically for a given open angle channel with air velocity. The IDCA point for the channel wall did not fall under the *Δθ* value for the material used at all air velocities. For the GDL surface, at higher air velocity, the IDCA point for the GDL fell inside the *Δθ* value showing that the droplet remained pinned to the GDL surface leading to no channel corner filling. However, at lower air velocity, the IDCA for both wall and GDL fell

outside their respective $\Delta\theta$ values showing that the droplet got de-pinned from the channel wall and led to corner filling. This implies that the air velocity changes the contact angle on the channel wall significantly due to the oscillation in the droplet.

4.3 Pressure Drop across the Droplet

The corner filling of a reactant channel leads to an undesired water buildup within the channel, which may eventually reduce the performance of a PEMFC. Pressure drop across the droplet is one of the reliable ways to measure the gas transport resistance due to the water hold up in the channel. When the water builds up in the channel, pressure drop increases accordingly. Therefore, lower pressure drop corresponds to lower gas transport resistance. In order to study the pressure drop across the droplet in various channels, a pressure tap was made behind the droplet inlet, which would read the pressure change across the droplet as the droplet grew. The peak pressure drop across the droplet for different air velocities in the channel was plotted and is shown in Figure 4.10. The uncertainty in the peak pressure drop was about 0.25%. Figure 4.10 clearly shows that in a 90° channel the pressure drop across the droplet increases as the air velocity increases. However, at lower air velocities the pressure drop is high. This is observed when the droplet grows and completely blocks the channel and the pressure in the channel starts to build up. When the pressure in the system reaches to a certain point, the droplet is removed from the channel. The time taken by lower air velocities to remove the droplet from the channel is comparatively large, which leads to high pressure build up in the

channel. However, at higher flow rates, the droplet experiences a much stronger force due to the airflow, which pushes the droplet out of the channel sooner than at the lower velocities. This trend was similar for all channel angles showing corner filling. Also at higher air velocities between 1 and 1.6 m/s, the droplet behaves as a film in the channel, which helps in keeping the pressure drop low. In Figure 4.10, it is can be seen that the pressure drop value for the 60° channel is higher than that of the 90° channel. The channel area of the 60° channel is larger than that of the 90° channel. Hence, when the droplet fills the channel corner, more liquid water is present in the 60° channel compared to the 90° channel and the amount of pressure required to remove the droplet becomes large.

For the 45° and 30°channel, the droplet does not fill the corner of the channel at any air velocity. For these channels, the observed pressure drop value is significantly lower when compared to that of the 60° or 90° channels where the corner of the channel is filled. For the 50° channel, at higher air velocities, the droplet did not fill the corner and the pressure drop is lower whereas at lower air velocities where the droplet fills the corner, the pressure drop was comparatively larger. In addition, at much higher air velocities between 1.6 and 2.4 m/s, the droplet was removed from the channel before it touched the channel walls. This behavior was reflected in the pressure drop plot by a drop in the peak pressure drop value. It was also observed that the pressure drop is directly proportional to the channel angle for the non–filling channel angles, i.e., the 30° channel has the lowest pressure drop for a given flow rate and the 50° channel has the highest

pressure drop amongst the three. The main reason for such low pressure drop values for the smaller channel angles is mainly due to the gap near the channel corner. For example, in the 30° channel the droplet squeezes in the channel due to the geometry before it is removed in such a way that there is a larger gap near the sidewall corner for the air to squeeze through and escape to the atmosphere. This leads to the lower pressure drop observed in the channel. However, in the 50° channel, the space for the air to squeeze through the channel is less than in the 30° channel, which increases the velocity of the air around the droplet. This leads to building up of pressure before the droplet is pushed out of the channel and the observed in the channel.

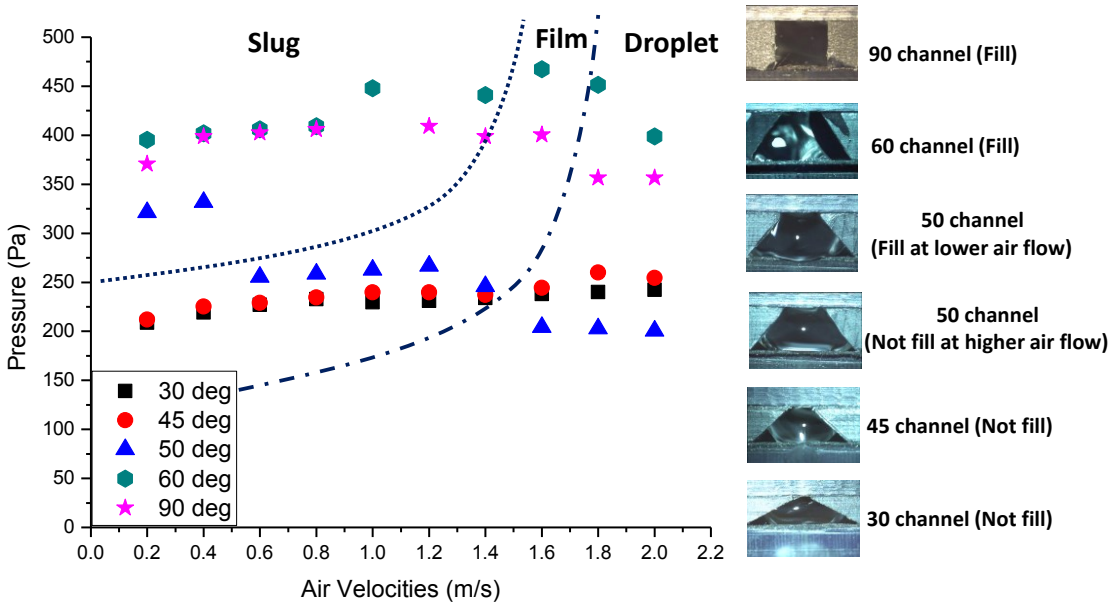

Figure 4.10: Plot of the peak differential pressure drop values across the droplet for different channel angles as a function of air velocity. The dotted line shows the transition in the flow pattern inside the gas channel from slug to film flow and the dot-dash line shows the transition from the film to droplet flow observed in the channel through the experimental data.

The different flow patterns observed in this study are slug flow, film flow and droplet flow. The dotted line and the dot–dash line in the plot, which are plotted using visual observation of the data, show the flow patterns observed for different channel open angles at different air velocities. The pressure drop points falling to the left side of the dotted line represent slug flow, the points falling on the right side of dotted line show film flow and the points falling to the right side of the dot-dash line shows droplet flow. It was observed from the high–speed videos that at higher air velocities (1.6 m/s and above), all the channels showed droplet flow, i.e., the droplet did not touch the sidewalls and is removed as a droplet.

4.4 Effect of Channel Wall Material

To evaluate the droplet behavior as a function of different sidewall materials, experiments were conducted with stainless steel (SS–2205), copper (Cu–110) and graphite composite channel walls with 45° and 50° open angles. These angles were chosen as they were near the transition angle for the materials mentioned with MRC–105 as the base. The transition angles calculated using the static contact angle for these materials with the MRC–105 GDL are shown in Table IV. For all these experiments, the MRC–105 GDL base was kept constant and the sidewall materials were changed. The air velocities in the channel were varied between 0.2 and 2.4 m/s. Different dynamics were observed for different sidewall materials.

4.4.1 **Stainless Steel Sidewall**

The transition angle for SS–2205 and MRC–105 was found to be 49° according to a theoretical prediction using the Concus–Finn condition. Experimentally it was found that for a 45° channel, corner filling did not occur for any air velocity agreeing with the theoretical predictions. A recorded image sequence of the droplet growth and its interaction with the SS–2205 sidewall for a 45° channel and air velocity of 1.6 m/s is shown in Figure 4.11. The IDCA for the SS–2205 sidewall and the MRC–105 base measured from each frame of the video sequence was plotted against the CFL as shown in Figure 4.12. According to the Concus–Finn condition, any point falling below the CFL line would lead to a corner filling condition, and any point above would lead to a no corner filling condition. The Concus–Finn plot with IDCA points also verified the observed experimental behavior.

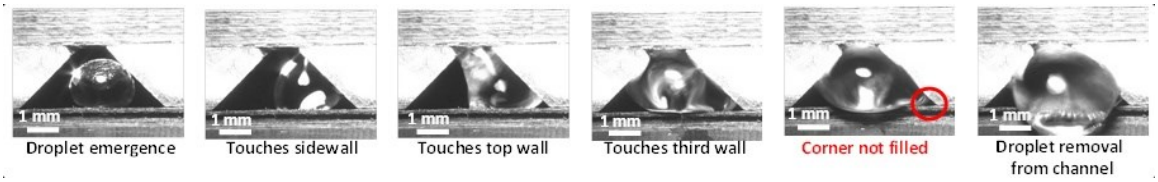

Figure 4.11: Image sequence of the droplet interaction with the Stainless Steel (SS 2205) sidewall and MRC–105 base in the 45° open angle channel with 1.6 m/s air velocity inside the channel. The red circle in the image shows that the droplet does not fill the channel corners.

However, for the 50° channel, the experimental and theoretical results did not agree. For the 50° channel, corner filling was observed only for lower air velocities between 0.2 and 0.6 m/s, and not for higher air velocities (0.7 – 2.4 m/s). Image

sequences of the droplet interacting with the 50° channel walls with an air velocity of 1.6 m/s are shown in Figure 4.13. For higher air velocities, the IDCA fell above the CFL line leading to non–corner filling behavior.

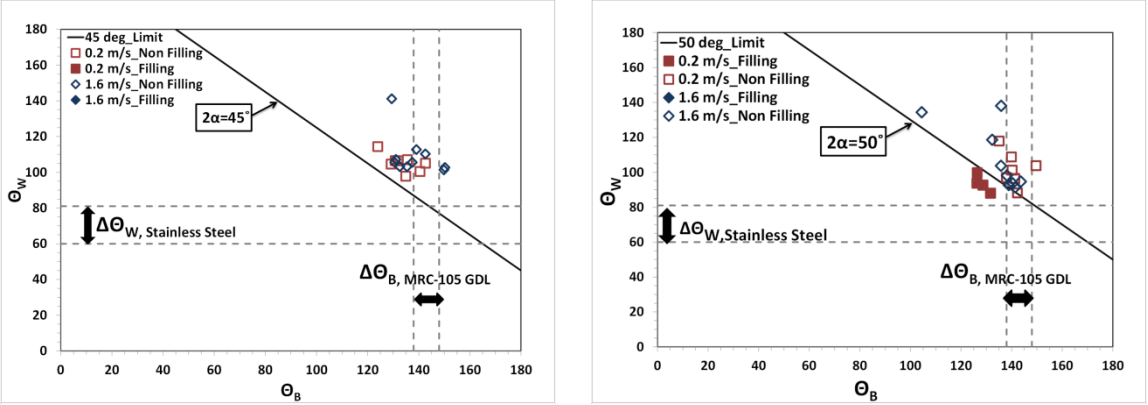

(a) **(b)**

Figure 4.12. Plot of IDCA made by the droplet at different air velocities with the Stainless Steel (SS-2205) sidewall and the MRC–105 GDL base for (a) a 45° open angle channel and (b) a 50° open angle channel.

From the experiments, it was observed that the effect of air velocity was pronounced, and caused an "imbalance" in the droplet at higher velocities causing noticeable oscillations. This "imbalance" marked the transition between channel filling and non–filling behaviors at the transition angles (disagreeing with the traditional Concus–Finn condition). The use of dynamic contact angle information is emphasized to predict the droplet behavior and thus, the overall water coverage ratio on the GDL more accurately.

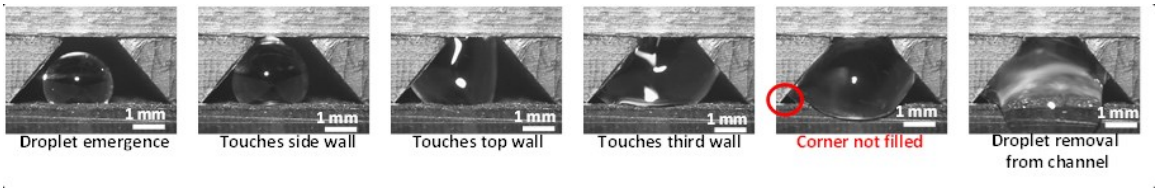

Figure 4.13. Image sequence of the droplet interaction with the Stainless Steel (SS-2205) sidewall and MRC–105 base in a 50° open angle channel with 1.6 m/s air velocity inside the channel. The red circle in the image shows that the droplet did not fill the channel corner.

4.4.2 **Copper Sidewall**

A similar set of experiments as mentioned above was conducted with the Cu–110 sidewall. According to the theoretical prediction, the transition angle for Cu–110 and MRC–105 should be 48°. The experimental results for both the 45° and 50° channels were similar to those observed for SS–2205 sidewalls. For the 45° channel, the channel corners were not filled for all the air velocities introduced in the system. However, in the 50° channel, the channel corners was filled at lower air velocities between 0.2 and 0.6 m/s, and was not filled at higher air velocities between 0.7 and 2.4 m/s.

4.4.3 **Graphite Sidewall**

For the graphite sidewall, the transition angle from corner non–filling to filling was found to be 52° according to theoretical prediction. The experimental results showed that for 45° and 50° open angle channels, the droplet did not fill the channel corners for any air velocities between 0.2 and 2.4 m/s. The results agree with the IDCA plot (Figure 4.14) which showed no corner filling for all air velocities as well.

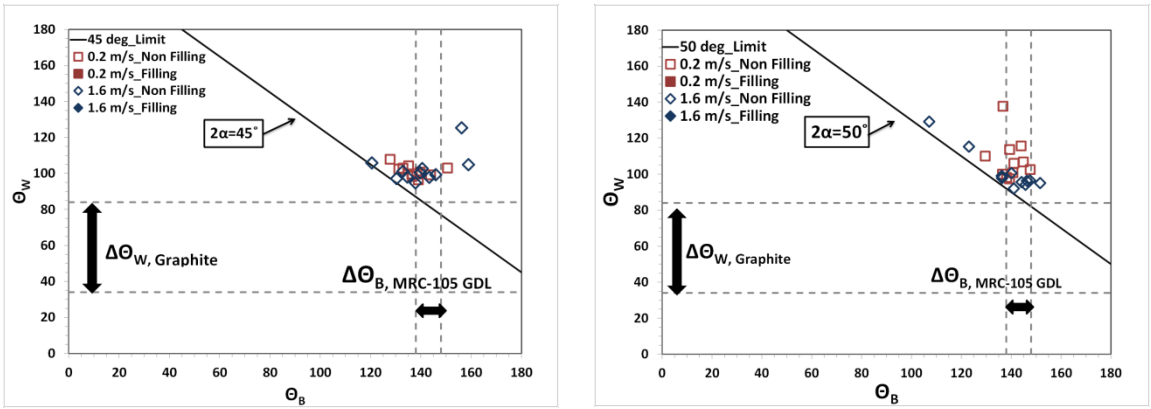

(a) **(b)**

Figure 4.14: Plot of IDCA made by the droplet with the graphite sidewall and the MRC-105 GDL base for (a) 45° channel open angle and (b) 50° channel open angle at different air velocities. Contact angle points fall above the CFL line showing that the corner should not be filled for any air velocities.

The three channel wall materials proposed for the use in automobile applications (stainless steel, copper, graphite) have been found to have varying effects on the droplet behavior depending upon their $\Delta\theta$ value. Near the transition angle, the graphite composite that has a larger $\Delta\theta$ as shown in Table III, behaved differently than materials having a lower $\Delta\theta$. It can be concluded that the $\Delta\theta$ affects the droplet behavior in the gas channel. Materials having a larger $\Delta\theta$ value can accommodate a larger range of contact angle changes in the droplet due to the airflow in the channel. In these materials, the droplet pins to the wall and does not move to the channel corners very easily. This leads to a no corner filling condition in the channel. On the other hand, droplets on materials having a smaller $\Delta\theta$ can only accommodate small oscillations produced by the airflow before getting de–pinned from the surface and moving towards the channel corner and filling it. More insight on the transport resistance offered by these different channel materials is

provided by the pressure drop data in the channel which is discussed in detail in the next section.

When using a MRC–105 GDL with any of the selected channel materials, the droplet filling of the channel corners did not take place for angles below 45°, and the 50° channel behaved as a transition angle between filling and non–filling. The Concus–Finn condition could not accurately predict the corner filling behavior of the droplet near the transition angle. Hence, using IDCA information would be helpful in predicting the droplet behavior in the gas channel of a PEMFC.

4.4.4 **Pressure Drop in the Channel**

Figure 4.15 shows the peak pressure drop across the droplet in a gas channel with different channel wall materials and air velocities. The uncertainty in the peak pressure drop value was about 0.25%. For the 45° channel, Figure 4.15(a) shows that as the air velocity increases, the peak pressure drop across the droplet increases for different channel wall materials. Once the pressure inside the system reaches its maximum value, the droplet is removed from the system. At air velocities between 0.5 and 1.6 m/s, the droplet starts to transition towards the film flow regime instead of slug flow as observed at lower air velocities and the peak pressure drop starts to decrease. At higher air velocities between1.7 and 2.4 m/s the droplet was removed from the system before it even touched the sidewalls of the channel. Therefore, the force required to remove the

droplet was much less compared to that required at lower air velocities. The different flow patterns observed in the 50° open angle channel are shown in Figure 4.16.

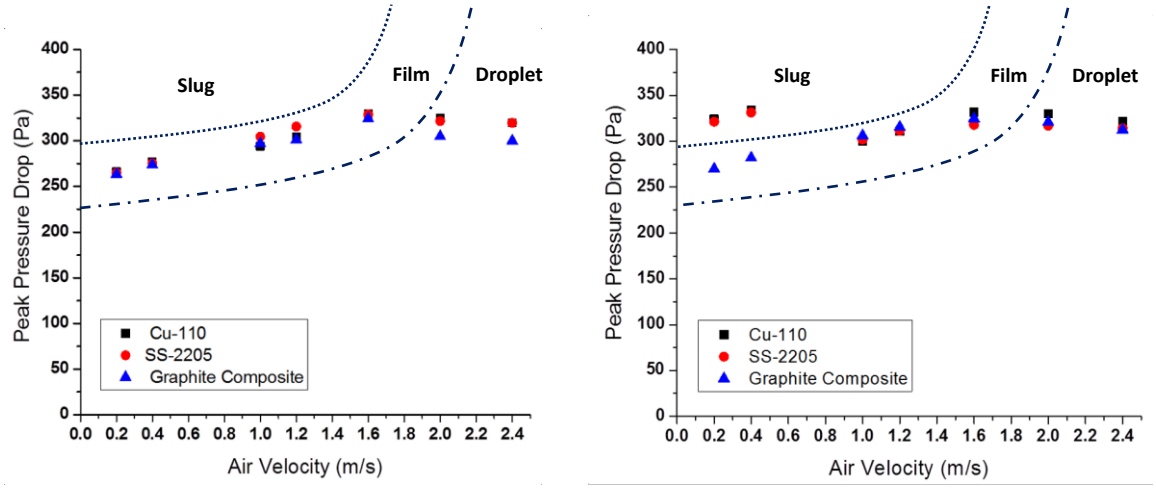

Figure 4.15: Peak pressure drop plot in the trapezoidal channel with different sidewall materials (Cu-110, SS-2205 and graphite composite) and MRC–105 GDL base for (a) a 45° channel (b) a 50° channel

It was also observed that there was no significant difference in the peak pressure drop value for each channel materials at a given air velocity in the system. However, in a 50° channel, the peak pressure drop followed a different trend. From Figure 4.15(b), it was observed that Cu–110 and SS–2205 produced a much higher pressure drop compared to the graphite composite channel wall at lower air velocities between 0.2 and 0.9 m/s. This was mainly due to the channel corner filling observed for both Cu–110 and SS–2205 at lower air velocities.

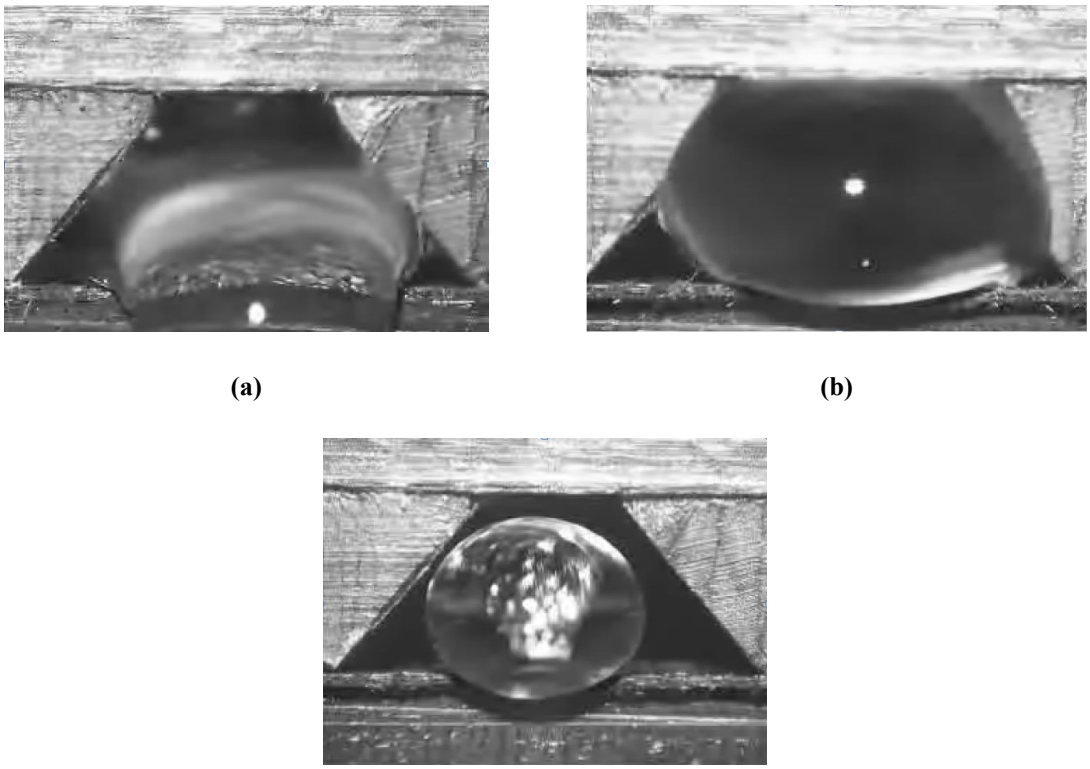

(a) **(b)**

(c)

Figure 4.16: Water flow pattern in a 50° channel at different air velocities (a) 0.4 m/s – slug flow (b) 1.6 m/s – film flow (c) 2.0 m/s – droplet flow

On the other hand, the graphite composite channel wall showed no corner filling at lower air velocities, resulting in a much lower pressure drop in the system. At medium air velocities between 1.0 and 1.6 m/s, the entire set of channel wall materials showed a similar peak pressure drop in the system, which increased with an increase in the air velocity. This corresponded to the non–corner filling condition observed in the experiments. At much higher air velocities between 1.7 and 2.4 m/s, the peak pressure drop in the system started to gradually decrease, since the droplet transitions to drop flow,

and produces much lower blockage in the channel cross section compared to the slug and film flow at low and medium velocities.

The different flow patterns observed in this study are shown in Figure 4.15. The dotted line in the plot shows the flow pattern transition from slug to film flow and dot–dash line shows the transition from film to droplet flow for different channel materials at different air velocities. It was also observed from the plot that for a 45° channel all the materials showed film and droplet flow in the channel. For a 50° channel, Cu–110 and SS–2205 showed slug flow in the channel for lower air velocities (0.2 – 0.4 m/s), film flow at medium air velocities between 0.5 and 1.6 m/s, and droplet flow at higher air velocities (1.7 – 2.4 m/s). Graphite sidewall material showed only film and droplet flow for all air velocities introduced into the 50° trapezoid channel.

Droplet pinning to the channel wall and corner filling or non–filling are not only dependent on the channel material used but also on the GDL material used. Hence to evaluate the effect of GDL material on droplet pinning, a similar study was performed.

4.5 Effect of GDL Material

There are different types of GDL materials that are used in PEMFCs. The most commonly used GDLs for automobile application are Toray, SGL and MRC–105. To evaluate the effect of different GDL materials on droplet growth and removal, experiments were performed under conditions similar to the sidewall material study. In

these experiments, the channel wall material was kept constant (polycarbonate) while the GDL material was changed along with the channel open angle.

4.5.1 **Toray (TGP–H–060) GDL**

For Toray (TGP–H–060 with 6% PTFE) GDL and a polycarbonate sidewall, the transition angle was found to be 50° according to the Concus–Finn condition. According to the experimental results, no corner filling behavior was observed for both 45° and 50° channels at all air velocities introduced in the channel. The experimental results agreed with the theoretical predictions for the TGP–H–060 GDL. The IDCA plot for both the 45° and 50° channel at 0.2 and 1.6 m/s air velocities is shown in Figure 4.17. From the IDCA plot, it can be seen that the contact angle values fall well above the $\Delta\theta$ values. This is mainly due to the oscillations in the droplet, which affect the contact angle the droplet makes with the wall.

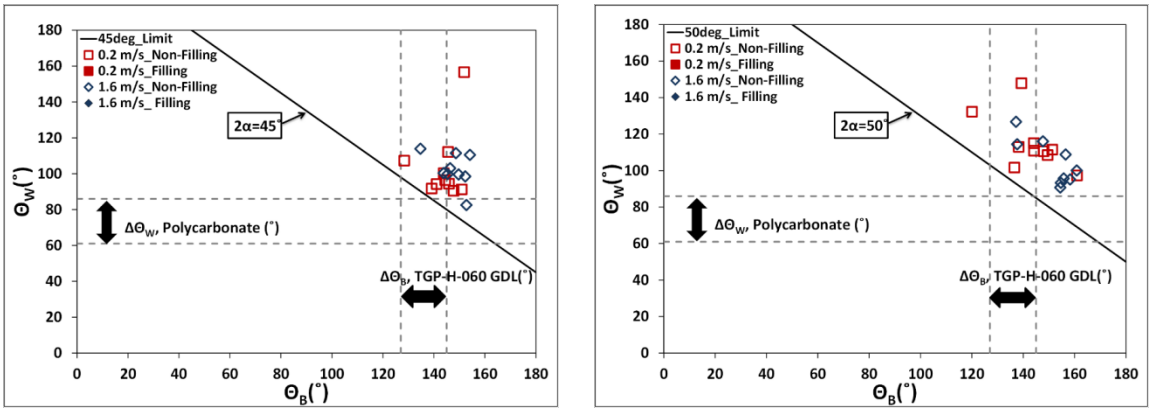

(a) **(b)**

Figure 4.17: Plot of IDCA made by the droplet with the polycarbonate sidewall and the TGP–H–060 base for (a) a 45° channel and (b) a 50° channel at different air velocities

4.5.2 **SGL–25BC GDL**

The theoretical transition angle for SGL–25BC and polycarbonate is 51°. Experimental results for SGL–25BC were similar to the TGP–H–060 GDLs performance. For a SGL–25BC GDL, the droplets did not fill the channel corners for both 45° and 50° channels at all air velocities. However, there was a significant difference in the droplet interaction pattern with the channel walls when a SGL–25BC base was used. High–speed videos of the droplet interaction with the channel walls for a SGL–25BC base revealed that at any given air velocity, the droplet would grow on the GDL until it jumped and made its first contact with the top wall. In other material studies, the first contact the droplet made was mostly with the channel sidewalls. For SGL–25BC, once the contact was established with the top wall, the droplet moved towards the sidewall and eventually blocked the entire channel cross section. The image sequence of the droplet growth in the 50° open angle channel at 1.6 m/s air velocity is shown in Figure 4.18.

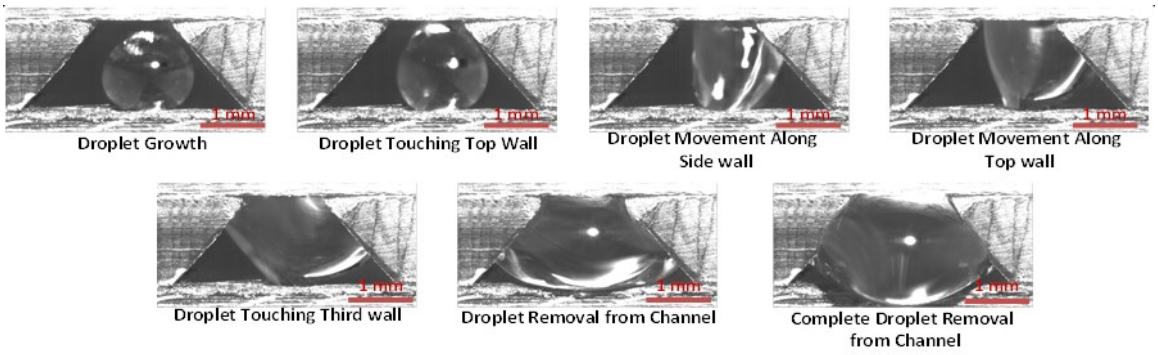

Figure 4.18: Image sequence of the droplet interaction with the polycarbonate sidewall and SGL–25BC base in the 50° open angle channel with 1.6 m/s air velocity. It was seen from the images that the fiber entanglement pattern of the GDL has a significant impact on the droplet dynamics in the gas channel.

The droplet's jumping behavior and clinging to the top wall can be attributed mainly to the fiber entanglement pattern of the GDL surface. In general, SGL–25BC has a more openly packed fiber structure than TGP–H–060 or MRC–105 as shown in Figure 1.5. The open fiber structure allows the water to overcome the breakthrough pressure and to be pushed through the GDL easily. In addition, the droplet inlet being more centered in the channel makes it easier for the droplet to touch the top wall instead of the sidewall first. In addition, SGL–25BC and TGP–H–060 have their transition angles near 50°, but there was no corner filling for any air velocities in the 50° channel. However, MRC–105 showed corner filling at lower air velocities and non–filling at higher air velocities. To understand this behavior, the IDCA plots for 0.2 and 1.6 m/s air velocities were plotted for both MRC-105and SGL-25BC GDL for 50° channel and are shown in Figure 4.19. It was seen from the plot that at lower air velocity, the IDCA for the MRC–105 GDL and polycarbonate wall (Figure 4.19(a)) fell outside their respective $\Delta\theta$ range. This shows that the droplet is de-pinned from both sidewall and base surface and lead to corner filling of the channel. However, for SGL-25BC at lower air velocity as shown in Figure 4.19 (c), the IDCA points for the base fell within the $\Delta\theta$ range. This shows that the droplet could not be de-pinned from the GDL base and therefore, showed no corner filling behavior for SGL-25BC GDL. At higher air velocity, for both SGL-25BC and MRC-105, the droplet did not fill the channel corners due to the pinning of the droplet on the GDL surface as shown in Figure 4.19(b) and (d). Thus, the oscillations produced by the airflow and the $\Delta\theta$ due to material surface characteristics and fiber entanglement pattern play a significant role in capturing the droplet dynamics within a PEMFC gas channel.

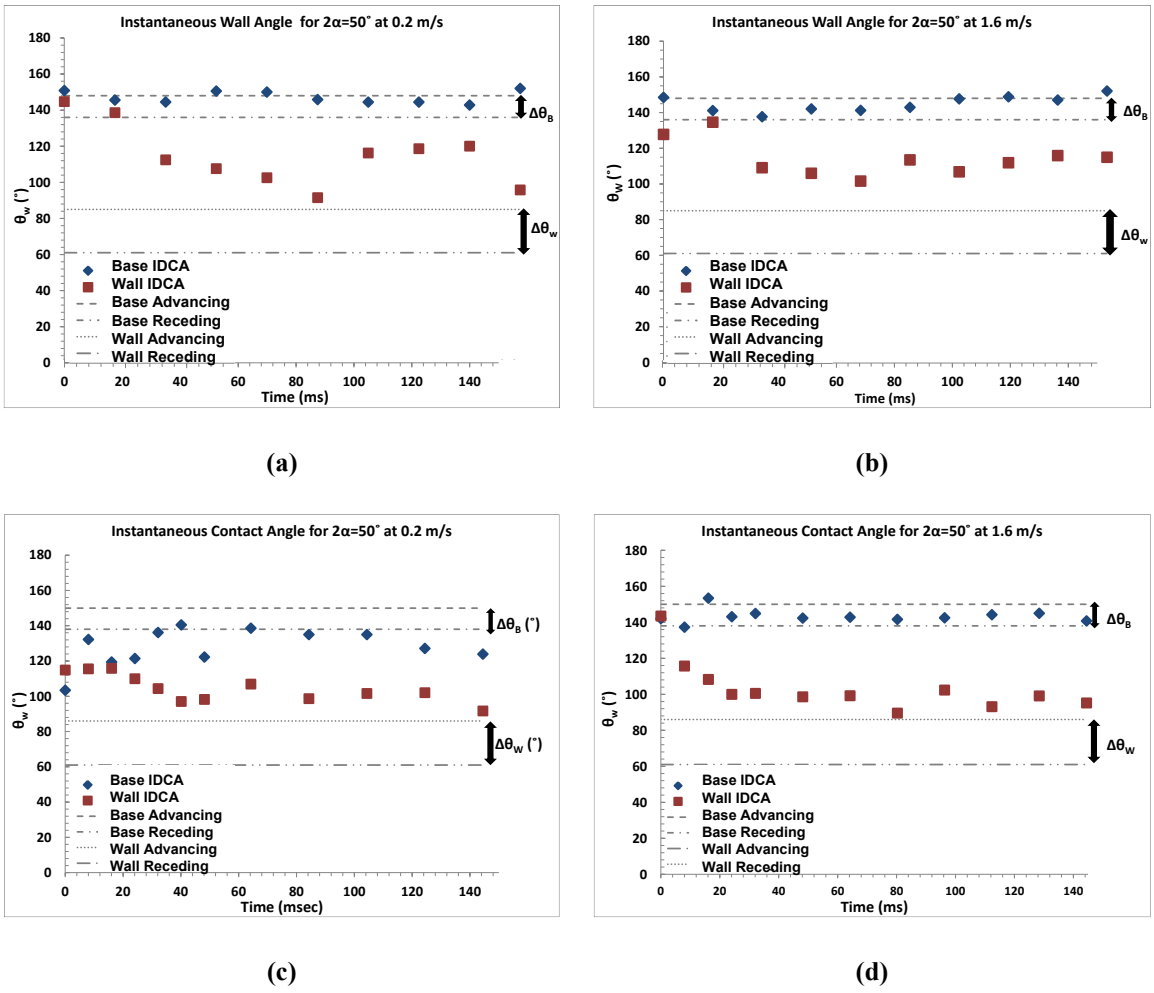

Figure 4.19: Plot of IDCA points made by the droplet for 50° open angle channel with the polycarbonate sidewall and (a) SGL–25BC base at 0.2 m/s (b) SGL–25BC base at 1.6 m/s (c) MRC–105 base at 0.2 m/s and (d) MRC-105 base at 1.6 m/s.

4.5.3 **Pressure Drop in the Channel**

The peak pressure drop measured for different GDL materials followed a pattern similar to the one observed for different channel wall materials and is plotted in Figure

4.20. It was observed that for both SGL–25BC and TGP–H–060, the droplet did not fill the channel corners for 45° and 50° channels for any air velocities.

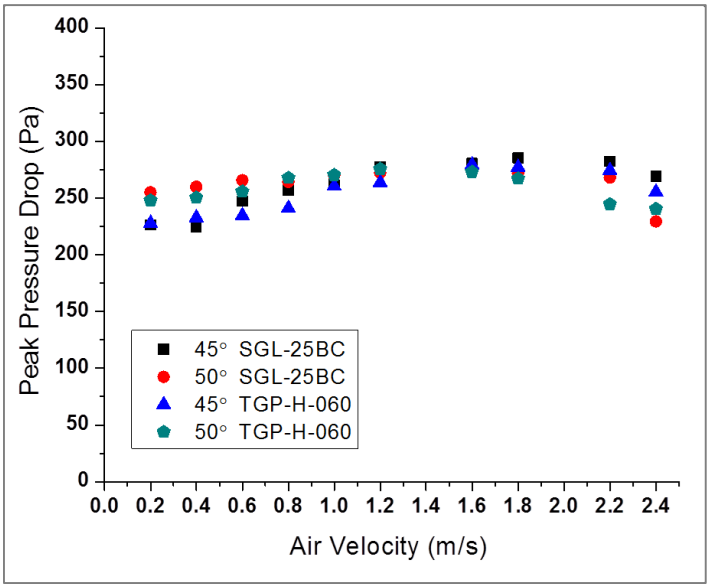

Figure 4.20 Plot of peak differential pressure drop values across the droplet for different GDL materials (SGL-25BC and TGP-H-060) in 45° and 50° open angle channels as a function of air velocities.

The peak pressure drop values measured for a given channel angle with different GDL materials also showed similar results observed for different channel wall materials. The peak pressure drop value was lower than to those observed for channels with corner filling behavior. For both SGL–25BC and TGP–H–060 at air velocities lower than 1.7 m/s, the peak pressure drop in the channel increased as the air velocity increased. However, for higher air velocities (1.8 – 2.4 m/s), the peak pressure drop started to decrease. It is also interesting to note that the pressure drop values observed for different GDL types with polycarbonate sidewalls were similar to those observed for the MRC–

105 GDL and polycarbonate sidewall. This indicates that GDL materials do not have a significant effect on droplet–wall interactions.

4.6 Effects of GDL Degradation

GDL deterioration mechanism and its effect on the fuel cell performance is a well–studied area, but there have not been studies to validate the effect of GDL degradation on the droplet dynamics in the PEMFC. To understand the effect of GDL degradation or deterioration on droplet dynamics inside the gas channel of PEMFCs, MRC–105 GDLs, which had been run previously for 40 and 125 hours in an *in situ* experiment, were employed.

Experiments were performed using these GDL samples with polycarbonate channel walls under similar test conditions used to study effect of different GDL materials. It was observed from these experiments that after 40 hours of run time, the used GDL performed similarly to a fresh MRC–105 GDL. With a 45° channel, the 40 hours run GDL did not show corner filling behavior for any air velocities introduced in the system. With a 50° channel, it showed corner filling behavior at lower air velocities, and non–corner filling behavior at higher air velocities. However, the GDL with 125 hours of run time showed different behavior. It was observed that the droplet filled the channel corners for both 45° and 50° channels at all air velocities. To understand this behavior more precisely, the advancing and receding contact angles on the used GDL samples were measured and are shown in Table V. It was observed that the 125 hours of

run GDL had much lower advancing and receding contact angles than fresh samples. However, samples with 40 hours of run time did not show much difference from the fresh samples in terms of advancing and receding contact angles. This shows that the wettability of the GDL material reduces with longer run time.

Table V: Contact angle measurements on GDLs that were run for longer hours

Material	Advancing Contact Angle (θ_{adv})	Receding Contact Angle (θ_{rec})	Contact Angle Hysteresis ($\Delta\theta_{hys}$)	Transition Angle
MRC–105 fresh sample	148°	138°	10°	53°
MRC–105 (40 hours run)	145°	135°	10°	49°
MRC–105(125 hours run)	131°	120°	11°	37°

The transition angle for both 40 and 125 hours run time samples with polycarbonate sidewalls were calculated and found to be 49° and 37° respectively. This explains the discrepancy observed in the droplet dynamics for the 125 hours run time sample. To further validate these results, IDCA data for both 40 and 125 hours run time samples with polycarbonate sidewalls and a 50° channel were plotted and are shown in Figure 4.21. Figure 4.21(a) shows that for the 40 hours run time sample, the droplet fills the channel corners at lower air velocities, and does not fill the channel corners at higher air velocities. Figure 4.21(b) shows the plot for the IDCA for the 125 hours run time sample.

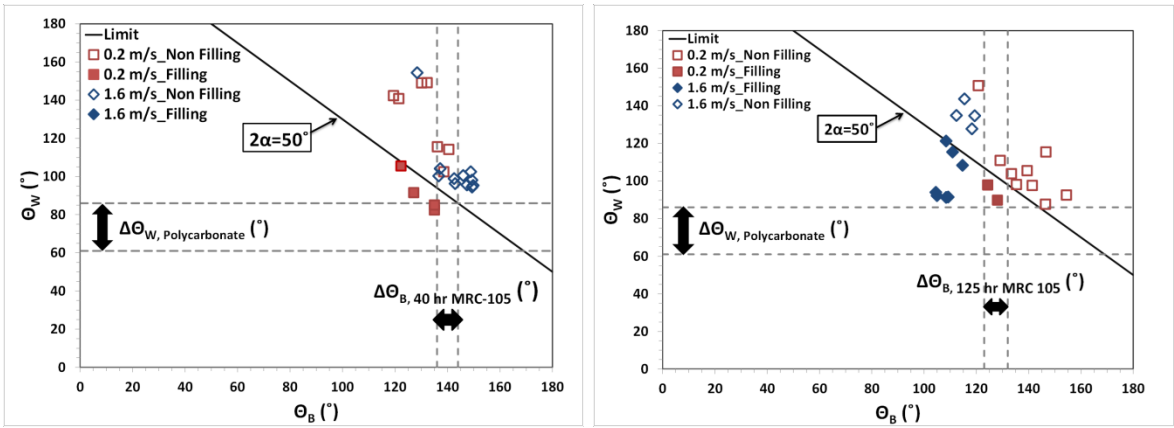

(a) **(b)**

Figure 4.21: Plot of IDCA made by the droplet in a 50° open angle channel at different air velocities with the polycarbonate sidewall and (a) 40 hours run MRC–105 GDL and (b) 125 hours run MRC–105 GDL

It can be seen from the plot that the IDCA points fall below the CFL line for all air velocities indicating that the droplet should fill the channel corners. This work clearly indicates that the GDL material deteriorates or loses its wettability after longer use, which perhaps affects the corner filling behavior of the droplet and leads to a larger accumulation of water inside the gas channel.

4.6.1 **Pressure Drop in the Channel**

Peak pressure drop for the used GDL materials differed significantly from that of fresh GDL samples. Figure 4.22 shows the peak pressure drop measured for a 50° polycarbonate channel with used GDL samples at different air velocities. From the plot, it can be seen that the peak pressure drop for the 40 hours run time sample at lower air

velocities were higher than at higher air velocities. This shows that the droplet fills the channel corners, forms slug flow at lower air velocities and results in higher pressure drop. At higher air velocities, the droplet transition to film flow and does not fill the channel corners, leading to a lower pressure drop in the system.

For the 125 hours run time sample, the droplets showed slug flow for all air velocities. The peak differential pressure drop values for all air velocities were much higher than those of the 40 hours run time sample. This shows that after a longer run time the wettability of the GDL is reduced. This leads to slug flow, which increases liquid stagnation in the channel and reduces the area available on the GDL surface for gas transport.

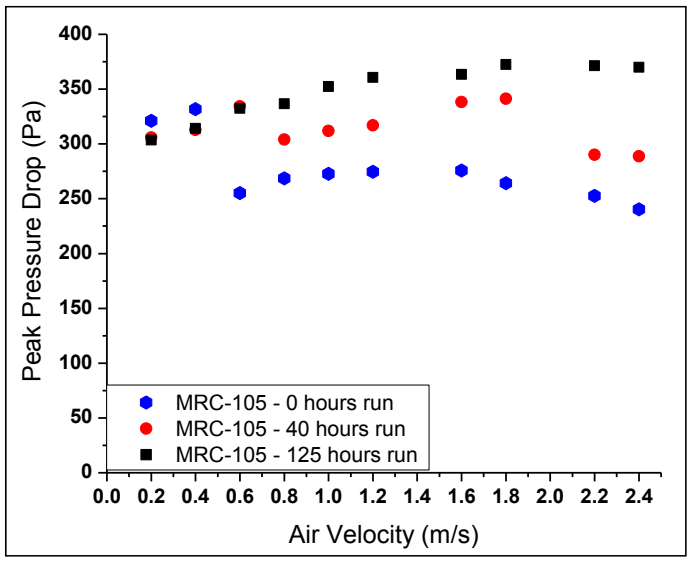

Figure 4.22: Plot of peak differential pressure drop across a droplet in a 50° channel for 0, 40 and 125 hours run MRC-105 GDL

4.7 Scaling of the System

Experiments were performed to understand the effect of scaling of the gas channel on the droplet behavior in the channel. Previously, experiments were performed on the *ex situ* system that had a 3 mm hydraulic diameter channel. These channels are almost three fold larger than an actual gas channel that is used in an automotive PEMFC. Therefore, to verify that the results observed for the large–scale channel hold for the small channel, similar experiments were performed using channels with smaller cross section dimensions. The experimental set up was similar to the one used for the larger channel experiment except that the channel was fabricated from polycarbonate with a channel cross section of 0.7 x 0.4 mm and 100 mm length.

Experiments were performed with superficial air velocities of 0.48 – 7.23 m/s, which correspond to the current densities of 0.1 – 1.5 A/cm^2. The Reynolds Number (Re) for the given air velocities in the channel was within the range of 15 – 233. Table VI shows the air velocities corresponding to the current densities and stoich with their respective Re in the gas channel. The water flow rate in this experiment was set at 0.005 ml/min, which corresponds to a current density of 0.3 A/cm^2 for an active area of 3.0 cm^2. The water flow rate does not have any direct bearing on the experiments as the study was focused on the discrete droplet behavior. The channel open angles used for this study were 45°, 50°, 60° and 90°.

Table VI: **Air velocities corresponding to the current densities and stoich with their respective Re**

Current Density (A/cm^2)	Stoichiometry	Air Velocities (m/s)	Reynolds Number (Re)
0.1	2	0.48	15.53
0.1	3	0.72	23.30
0.2	2	0.96	31.07
0.4	2	1.93	62.13
0.6	2	2.89	93.20
0.8	2	3.85	124.26
1.0	2	4.82	155.33
1.1	2	5.30	170.86
1.3	2	6.26	201.93
1.5	2	7.23	233.00

It was observed from the experiments that for air velocities from 0.48 and 4 m/s, droplets behaved differently at different open angles. In 90° and 60° channels, it was observed that the droplet filled the channel corners for air velocities below 4 m/s. Figure 4.23 shows the images of corner filling/non–filling behavior observed for different channel open angles at air velocities of 0.72 m/s and 3.85 m/s. From the figure, it can be seen that in the 45° channel, the droplet did not fill the channel corners at air velocities below 4 m/s. However, in the 50° channel, different droplet dynamics were observed at different air velocities. For air velocities between 0.48 and 1 m/s, the droplet showed corner filling behavior but for air velocities between 1 and 4 m/s, the droplet showed no

corner filling behavior. It could be concluded that the corner filling behavior observed in smaller channels was similar to the results observed for larger channel experiments. This clearly shows that the scaling of the system did not affect the droplet dynamics in the PEMFC gas channels. Hence, the larger channel experiment performed earlier which provided much easier visual and experimental results could be used to understand the liquid water dynamics.

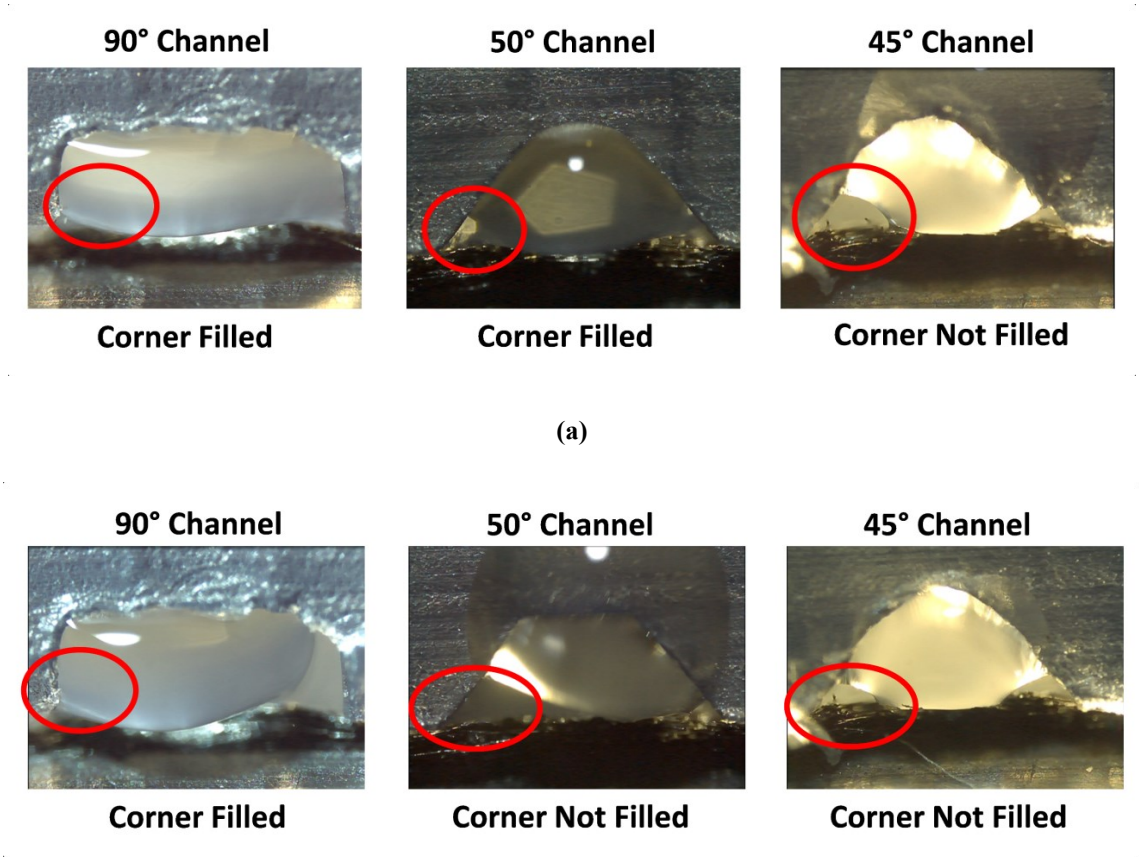

Figure 4.23: Corner filling and non–filling behavior in different channel open angles (90°, 50° and 45°) at different air velocities (a) 0.72 m/s (b) 3.85 m/s. For all air velocities, droplet fills the channel corner in a 90° channel and does not fill the corner in a 45° channel. In 50° channel, the droplet fills the channel corner at lower air velocities and does not fill at higher air velocities.

To characterize the liquid flow pattern in different channel open angles as a function of air velocity, videos were taken from the top view of the channel, i.e., along the airflow direction and parallel to the channel length. From this view, the length of the film or the slug or the droplet flow along the channel cross section was measured. Figure 4.24 shows a film and a slug flow pattern in the gas channel from a top view for 90° and 50° channels. Using these images, channel blockage percentages along the channel cross section were calculated and are shown in Table VII.

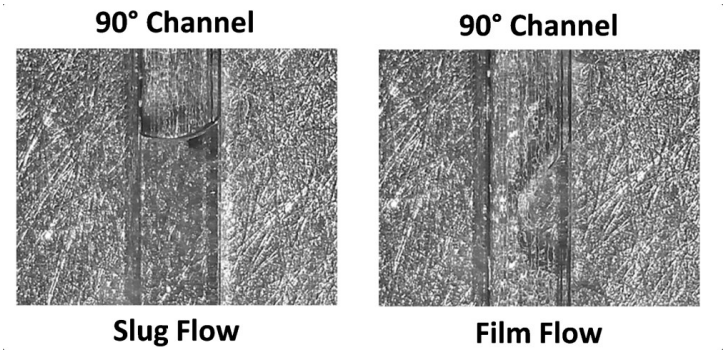

(a)

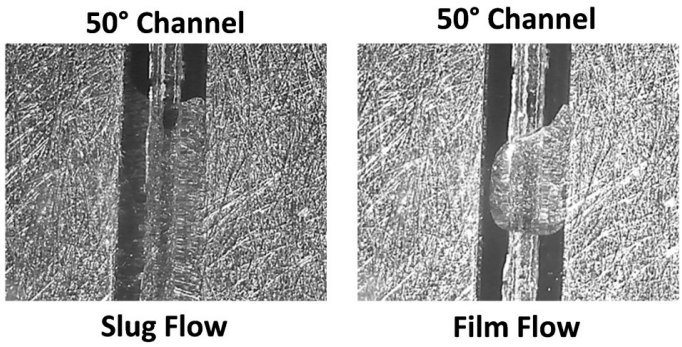

(b)

Figure 4.24: Image of a film and a slug flow from top view at air velocities of 0.72 m/s and 3.85 m/s respectively in a (a) 90° channel and (b) 50° channel.

Table VII: Liquid flow pattern and channel blockage percentage in the PEMFC gas channel as a function of air velocity

Channel Open Angle	Air Velocity	Slug/ Film	Channel Blockage Percentage
90	0.48	Slug	100
	0.72	Slug	100
	0.96	Slug	99.75
	1.93	Film	93.33
	2.89	Film	86.67
	3.85	Film	80.67
	4.82	Droplet	72.83
	5.30	Droplet	70.92
	6.26	Droplet	67.66
	7.23	Droplet	64.58
	9.60	Droplet	61.98
60	0.48	Slug	100
	0.72	Slug	100
	0.96	Slug	99.82
	1.93	Film	95.51
	2.89	Film	85.45
	3.85	Film	80.61
	4.82	Droplet	75.32
	5.30	Droplet	71.25
	6.26	Droplet	65.50
	7.23	Droplet	61.41
	9.60	Droplet	59.57

	0.48	Slug	100
	0.72	Slug	100
	0.96	Slug	99.60
	1.93	Film	86.67
	2.89	Film	80.67
50	3.85	Film	78.53
	4.82	Droplet	66.67
	5.30	Droplet	60.40
	6.26	Droplet	55.87
	7.23	Droplet	52.81
	9.60	Droplet	49.56

It is observed from the table that for lower air velocities (0.48 – 1 m/s), the droplet completely blocks the channel and forms slug flow. As the air velocity was increased above 1 m/s, the channel blockage percentage went down and the water flow pattern in the channel transformed into film flow.

To better understand the system performance in a smaller channel, pressure drop in the channel was measured across the droplet. The peak pressure drop across the droplet for different channel open angles used in the experiments is plotted against the corresponding air velocity in Figure 4.25. From the graph, it can be observed that the pressure drop in the channel increases with the air velocity in the channel. However, when the air velocity increases beyond 4 m/s, the peak pressure drop in the given system

starts to decrease. This decrease in the pressure drop is mainly due to the transition of the water to droplet flow in the channel.

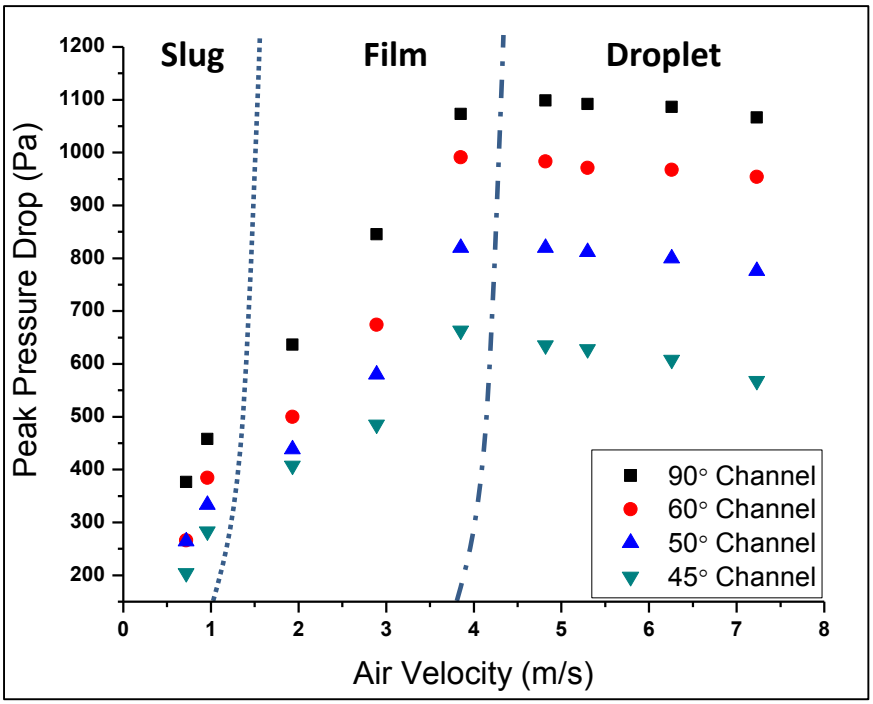

Figure 4.25: Peak differential pressure drop in the 0.4 x 0.7 mm channel of different channel open angle at different air velocities. The dotted line shows the transition in the flow pattern from slug to film flow and the dot-dash line shows the transition in the flow pattern from film to droplet flow through visual observation from the experimental data.

4.8 Effect of Droplet Inlet Location

In a PEMFC, droplet introduction on the top of the GDL surface is not bounded to the center of the channel. It could appear anywhere on the GDL surface, such as near the channel wall surface, at the channel center, or even under the land area. All the above experiments and dynamic contact angle plot results were recorded when the droplet was introduced at the center of the channel. To examine the droplet's behavior when it

appeared near the sidewall, a preferential pore for the droplet inlet was introduced 1 mm away from the sidewall and base interface. It was observed that for a 45° channel the droplet filled the channel corners for all air velocities as shown in Figure 4.26.

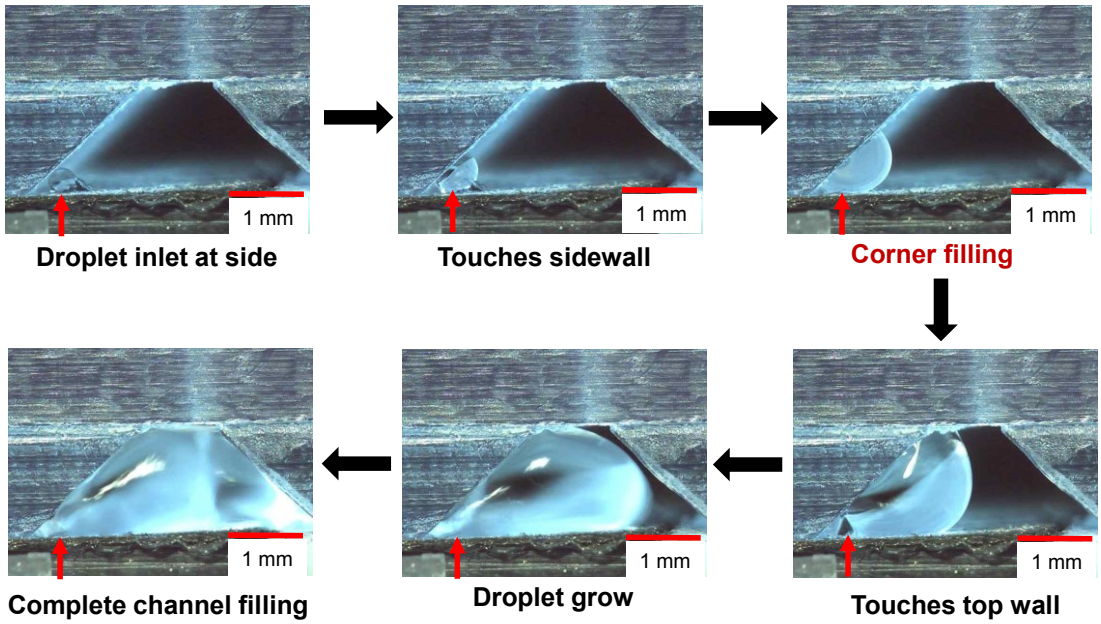

Figure 4.26: : Sequence image of the droplet interaction with the polycarbonate sidewall and GDL base in a 45° channel when the droplet is introduced near the sidewall (1 mm away from the channel corner) at an air velocity of 0.4 m/s introduced in the channel.

According to the Concus–Finn condition, the droplet should not fill the channel corner made by the polycarbonate and GDL in a 45° channel. Using the IDCA values from the experiments and plotting them against the CFL condition revealed that the droplet should indeed fill the channel corners as shown in Figure 4.27. This implies that the IDCA the droplet makes with the sidewall and GDL was altered dynamically by the airflow in the system, which led to the contact angle being in the filling region. This

accordingly changes the criteria of droplet filling and non–filling within the system. Hence, the CFL condition based on static contact angles for predicting the droplet filling or non–filling in the channel is not valid. Using IDCA values in the CFL condition will give the actual filling or non–filling criteria for the system.

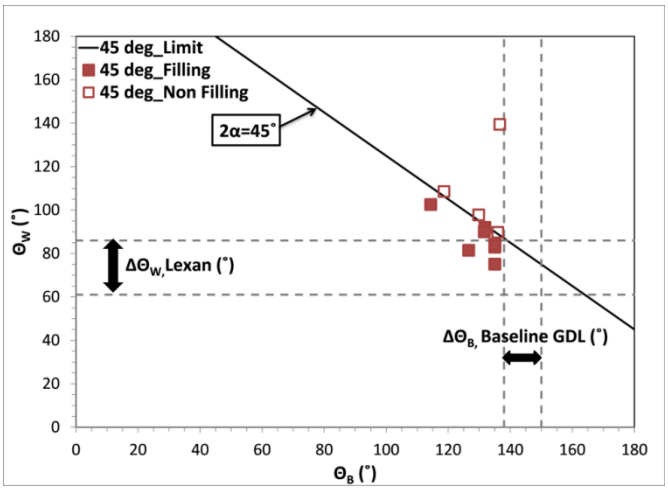

Figure 4.27: Plot of the IDCA made by the droplet with the polycarbonate sidewall and GDL base in a 45° channel when the droplet emerges near the channel corner. Here the contact angle points fall below the CFL line and show corner filling behavior in the gas channel.

Experiments were also performed to visualize the droplet behavior when the droplet was introduced under the land region. In this case, the droplet was introduced 0.5 mm away from the channel sidewall and base intersection into the land region. It was observed that irrespective of the channel angle, the droplet would be introduced into the channel by filling the corner. When the droplet is introduced under the land, it spreads along the land area. When it comes into the channel area, it wets the channel sidewall as well as the GDL surface. To avoid such scenario, different design for gas channel needs to be developed to avoid corner filling of the channel. Moreover, in this case, the

Concus–Finn condition cannot be used to evaluate the results. The Concus–Finn condition is valid only when the droplet emerges near the opening of the channel corner. When the droplet approaches the channel corner from the land region, the Concus–Finn condition cannot be used.

4.8.1 **Groove Capillary Channels for Removing Water Emerging Under the Land**

In a PEMFC, it was observed that the byproduct water emerging due to the electrochemical reactions occurring in the membrane often enters the gas channel through the land region [17]. Once the liquid water enters to the gas channel through the land region, the water is pinned at the gas channel corners. The pinning of the droplet near the channel corners act as a viable pinning site for other incoming droplets and eventually lead to slug flow in the gas channel [91]. To avoid water stagnation near the channel corners, groove patterned surfaces were designed on the channel sidewall to suck the water through the grooves to the top of the channel. Once the water reaches the top of the channel, the airflow inside the gas channel would remove the liquid water. Before the groove channel was designed, preliminary studies were performed to see how the grooves affect the water wetting on a given surface. As mentioned earlier, the liquid water's wetting of the material is dependent on the channel material and the roughness on the surface. If the roughness of a given material is comparable to the water present on the material, then the roughness of the material needs to be taken into account.

The main purpose of this study is to understand the design consideration of grooves acting as roughness on the channel sidewall [159, 160]. The grooves should be made such that the droplet interacting with the channel walls will be able to fill or wet the grooves so that the liquid can be pulled to the top of the channel by capillary forces. For the water to be pulled into the grooves, the liquid needs to wet the channel surface as a Wenzel wetting. Wenzel wetting of a surface happens when the liquid placed on the groove pattern wets the surface similar to the image shown in Figure 4.28(b), whereas Cassie–Baxter type wetting occurs when the droplet sits on the air gap between the grooves and does not wet the groove channels as shown in Figure 4.28(a).

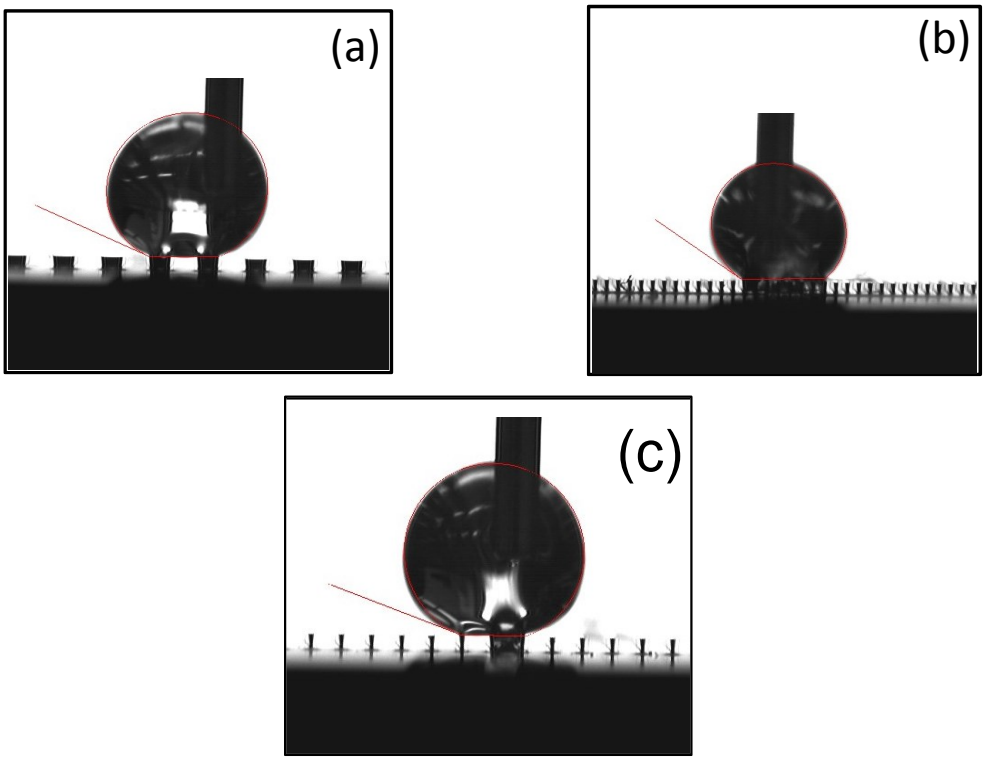

Figure 4.28: Liquid wetting behavior on a groove chip (a) Droplet sitting on the air in the channel area (Cassie-Baxter type wetting) (b) Droplet fills the channel area (Wenzel type wetting) (c) Droplet transitions from Cassie to Wenzel wetting (Metastable state)

Preliminary experiments were performed to understand how the groove–patterned roughness affects the wetting behavior on a surface. For these experiments, <1 0 0> p–type silicon chips 20 mm × 20 mm in size with etched microchannels of different roughness patterns were used. Silicon chips were used for this experiment as they have a similar static contact angle to polycarbonate and copper, and are also easier to fabricate 100 μm channels on silicon. Table VIII shows the groove patterns that were made on the silicon chip.

For different values of channel depth and width, the droplets exhibited Wenzel or Cassie type behavior as shown in Figure 4.28, and at times, even a metastable state was observed. A metastable state is where the droplet is in transition between Wenzel and Cassie wetting as shown in Figure 4.28(c). The complete set of observed behavior for different channel configurations is tabulated in Table IX. It was also observed that for a channel width above 161 μm the droplet sometimes enters into a metastable state and transitions into Wenzel type. This illustrates that the droplet wetting characteristics is affected by the channel width.

In addition to the channel width effect, an additional effect of roughness height was observed. When a droplet is in the Cassie state, reducing the roughness height below a certain limit makes it enter the Wenzel state. The transition occurs when the roughness height is smaller than the depth to which liquid projects into the channel.

Table VIII: Dimensions of different groove roughness patterns on the silicon chip

Chip	Land Width (µm)	Channel Width (µm)	Depth (µm)	Groove Profile
1	38	41	193	
2	38	71	204	
3	97	103	200	
4	99	71	200	
5	37	201	198	
6	40	40	111	
7	39	171	114	
8	101	39	114	
9	39	200	112	
10	98	250	102	
11	39	161	121	
12	99	201	151	
13	37	250	200	
14	39	140	112	
15	99	200	107	
16	199	200	109	
17	199	250	114	

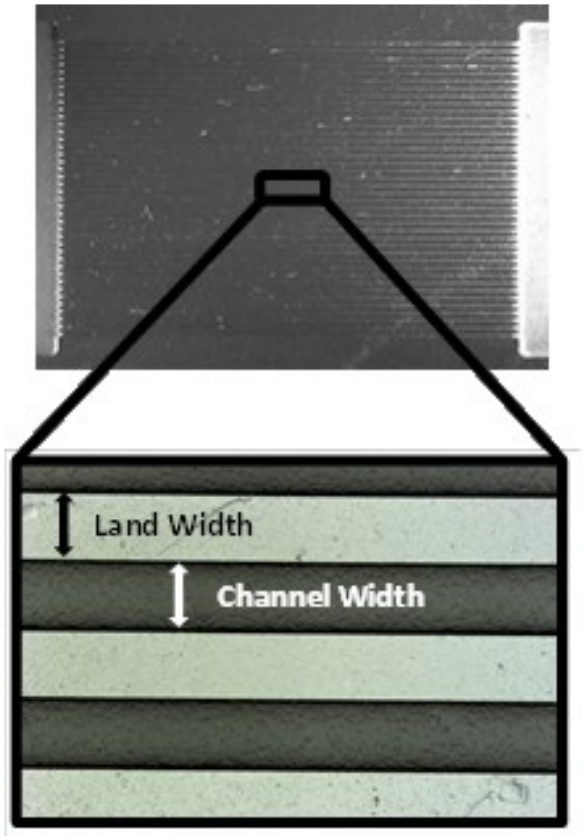

The effect of channel depth can be seen by comparing chips 5 and 9. Both have similar land width and channel widths of around 40 µm and 200 µm respectively, but chip 5's channels are 198 µm deep while chip 9's channel are 112 µm deep. The deeper

chip 5 exhibits Cassie behavior, while the shallower chip 9 exhibits Wenzel behavior. Thus, it can be seen that the channel width and the roughness height both affected the wetting characteristics. However, there was no effect observed due to land width variation on the wetting characteristics of any surfaces used.

Table IX: Effect of scaling factor (*S*) on wettability transition and the contact angle on grooved roughness surface

Chip	Channel Width (W) (µm)	Depth (H) (µm)	Scaling Factor (*S*)	Wetting Type	Contact Angle Measured
1	41	193	4.71	Cassie	141.1
2	71	204	2.87	Cassie	143.7
3	103	200	1.94	Cassie	149.7
4	71	200	2.82	Cassie	145.5
5	201	198	0.99	Cassie	156.5
6	40	111	2.78	Cassie	148.6
7	171	114	0.67	Wenzel	141.5
8	39	114	2.92	Cassie	155.5
9	200	112	0.56	Wenzel	120.4
10	250	102	0.41	Wenzel	125.5
11	161	121	0.75	Metastable	160.4
12	201	151	0.75	Metastable	164.1
13	250	200	0.8	Metastable	165.8
14	140	112	0.82	Metastable	162.8
15	200	107	0.54	Wenzel	138.9
16	200	109	0.55	Wenzel	143.1
17	250	114	0.46	Wenzel	145.7

To better understand the relationship between the droplet behavior and the geometry of shallow grooves (or roughness features) at shallow roughness features, a scaling factor S was used, given by Eq. 4.2.

$$S = \frac{H}{W} \qquad [4.2]$$

where H is the groove depth or roughness height and W is the groove width. Bhushan *et al.* [32] introduced this scaling factor earlier for pillared roughness features where the scaling factor was defined as the ratio of the pillar diameter to the pitch of the pillars. The scaling factor for different chips used in our experiments varied from 0.4 to 4.8 and are shown in Table IX. The scaling factor was plotted for different chips used in Figure 4.29 to determine the transition point between Wenzel and Cassie regimes.

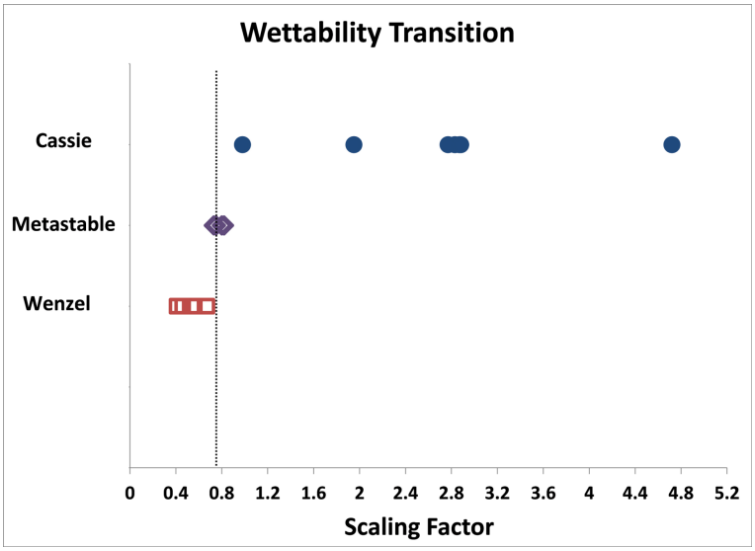

Figure 4.29: Wettability transition from Wenzel to Cassie regime on a groove patterned roughness as a function of scaling factor

It was observed that the droplets remain distinctively in the Cassie regime for $S > 1$, in the Wenzel regime when $S < 0.7$, and in a metastable state or transition state for $0.7 < S < 1$. In the metastable regime, the droplet showed both Wenzel and Cassie type wetting behaviors. The static contact angles measured on different chips were also plotted against the scaling factor, as shown in Figure 4.30 where it is seen that the Wenzel type droplets have lower contact angles than the Cassie droplets. Therefore, for patterned surfaces, the transition point from Wenzel to Cassie wetting can be considered to occur around scaling factors of 0.7 – 1.

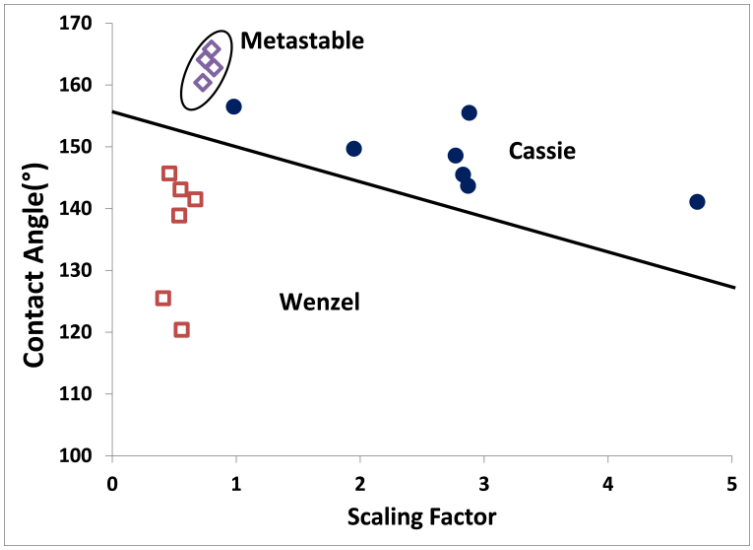

Figure 4.30: Contact angle measured on the groove chip surface as a function of scaling factor. Wenzel wetting shows lower contact angle values compared to the chips showing Cassie wetting. Metastable state wetting chips shows the highest contact angle value. The line shows the transition line between Wenzel and Cassie state contact angles.

Therefore, for the grooves in the sidewall of a PEMFC gas channel, the scaling factor S was used as a predictive tool to understand the change in wettability of the

channel sidewall due to the rough pattern introduced in the channel walls. The liquid would follow Wenzel wetting behavior, if $S \leq 1$. In fuel cell applications, the groove pattern needs to exhibit Wenzel wetting to draw the liquid inside the grooves. Once the liquid is drawn into the groove, capillary forces will pull the liquid to the top of the grooves. Therefore, the grooves were designed such that the $S < 1$. The image of the grooves on the sidewall of the gas channel is shown in Figure 4.31.

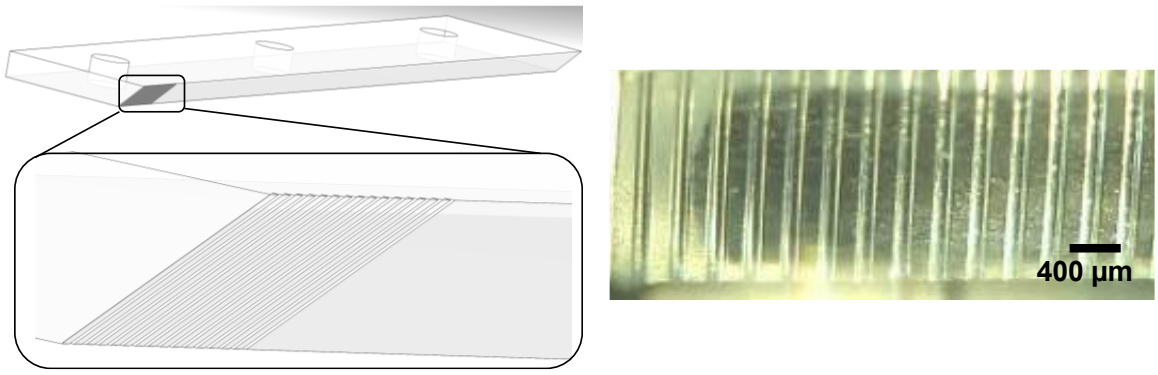

(a) **(b)**

Figure 4.31 (a) Groove pattern design on the sidewalls of the PEMFC gas channel (b) Experimental image of the grooves on the channel sidewall used for experiments.

The grooves made on the channel wall had a depth of 150 µm and a width of 200 µm. S was calculated to be 0.75, which means that liquid water should fill the grooves, which act as capillaries to suck the water to the top of the channel.

For this experiment, a polycarbonate base plate was used with a MRC–105 GDL placed on it with a preferential pore drilled in the GDL for liquid water to emerge on the GDL. A syringe pump was used to pump the water through the GDL under the land

region. A sidewall with the grooved pattern was placed on top of the GDL. The top wall made of polycarbonate was placed on the groove–patterned sidewall to form a 100 mm channel length. High–speed videos were captured to visualize the liquid water behavior near the channel corners using a Keyence VW–6000 high–speed camera. The videos showed that the water coming from the land area was sucked by the capillary grooves and the water rose to the top wall faster than its growth on the GDL inside the channel area. Figure 4.32 shows the image sequence of liquid water growth from the land area onto the groove pattern in the PEMFC gas channel. This shows that using the scaling factor one can predict the wetting behavior on a groove surface accurately.

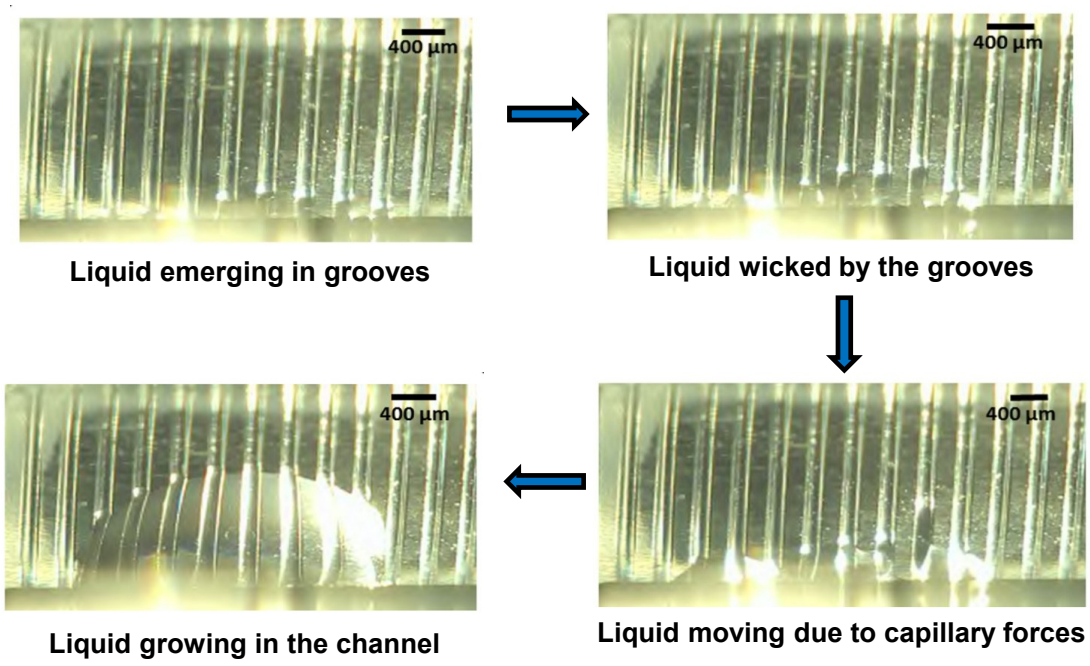

Figure 4.32: Image sequence showing the liquid water growth on the groove pattern in the PEMFC gas channel

However, the suction by the capillary grooves used for this experiment was not strong enough to pull the liquid quickly to the top due to the large size of the capillary grooves. Therefore, grooves with smaller channel depth and width are needed to achieve good capillary rise inside the grooves before the liquid grows inside the channel area. This is being incorporated in the future design of the sidewalls for PEMFC gas channel.

Chapter 5 Theoretical Results

Experimental results showed that droplet dynamics are dependent on the droplet inlet location, channel open angle, channel and base material properties and the inlet air velocity [161]. Therefore, to understand how all these parameters are affecting droplet dynamics in the gas channel, a theoretical analysis based on force balance and geometric analysis was performed.

Earlier, an experimental study performed by Rath and Kandlikar showed how the droplet behaves near the channel corner in the absence of airflow in the channel. They performed the experiment using a horizontal SGL–25BC GDL and a polycarbonate channel wall with an angle of 50° [89]. As we have seen from previous work, 50° is a transition angle for SGL–25BC and polycarbonate. In an experimental study, they observed that the droplet showed neither corner filling nor non–filling behavior, but instead the droplet detached itself from the base wall and jumped to the channel sidewall upon contact. Figure 5.1 shows the image sequence of the droplet jumping behavior to the sidewall in a 50° channel made of a polycarbonate sidewall and SGL–25BC GDL. Figure 5.1(a) shows the emergence of the droplet from the base of the channel. Figure 5.1(b) shows the droplet as it contacts the sidewall right before it jumps. Once sidewall contact is made, the droplet quickly moves towards the sidewall as shown in Figure 5.1(c) and then jumps as shown in Figure 5.1(d). Finally, the droplet completely disconnects from the base and hangs from the sidewall as shown in Figure 5.1(e). To

characterize the droplet jumping behavior and the effect of different parameters on droplet jumping, a geometric analysis was performed.

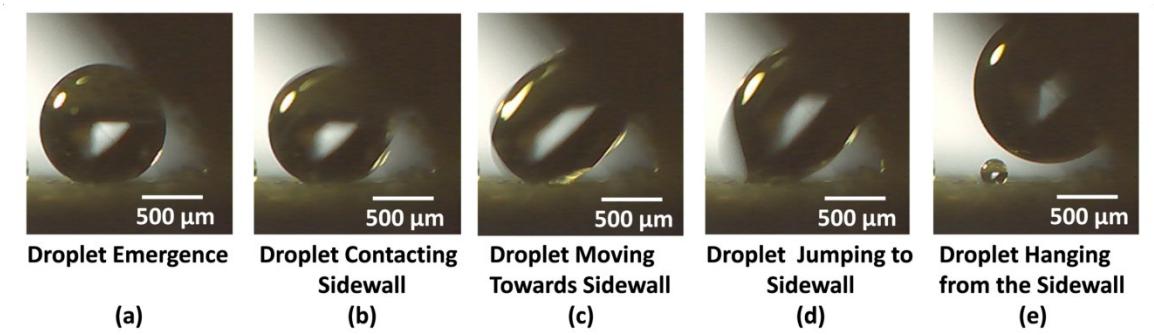

Figure 5.1: Image sequence of the droplet jumping to the sidewall in a 50° channel made of a polycarbonate sidewall and SGL–25BC GDL.

5.1 Geometric Analysis of Droplet Dynamics

For this analysis, three conditions are examined separately. The first condition is when the droplet sat on the base and touched the sidewall right before it jumped as shown in Figure 5.2. At this state, the maximum radius (R_{C_1}) of the droplet is determined.

When the droplet jumped to the sidewall, it was completely detached from the base and hung from the sidewall. The second condition in this analysis is to determine the droplet radius when it was hanging from the sidewall. Since the droplet's volume just before it touched the wall and right after it jumped to the wall is the same, two volume (V_1 and V_2) are equated to find the radius of the droplet (R_2) as it hangs from the sidewall.

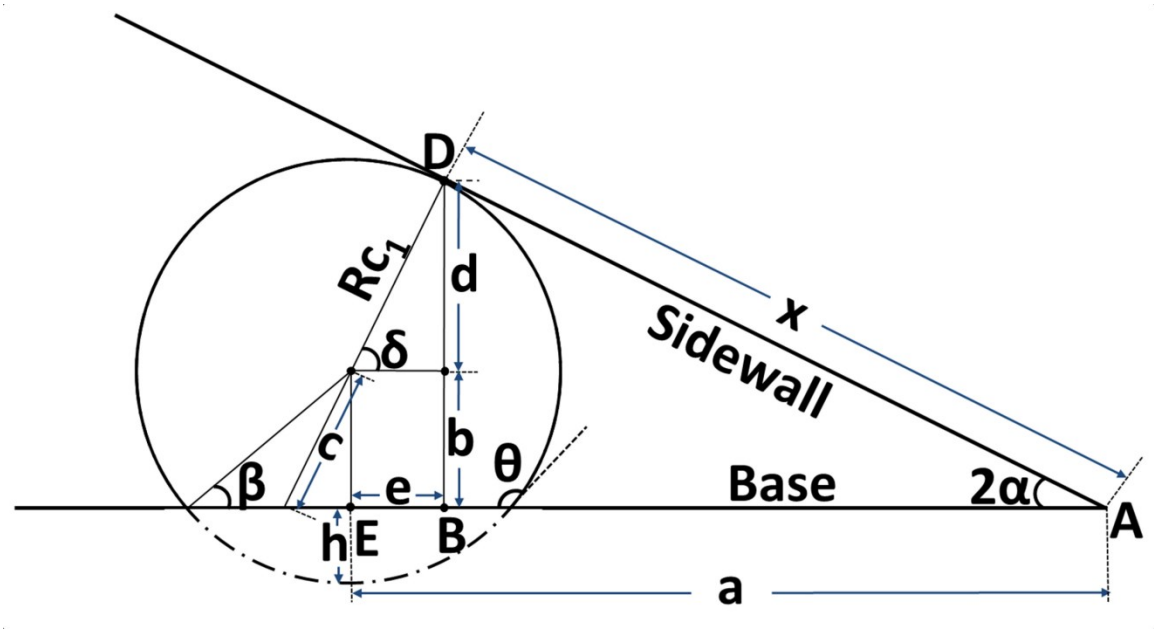

Figure 5.2: Description of the different contact lengths and contact angles made by the droplet with the base wall just before it jumped to the sidewall.

When the droplet hangs from the sidewall, the maximum size of the droplet can be large enough to touch the base of the channel and bridge between the sidewall and the base. Therefore, the third condition is based on the maximum radius (R_{C_2}) that the droplet can have when it jumps to the sidewall and hangs from it, right before it touches the base and bridges the two walls.

The droplet jumping behavior can be predicted by comparing R_2 with R_{C_2}. For the droplet to remain hanging from the sidewall, R_2 needs to be smaller than R_{C_2}. Using this analysis, a criterion is obtained in terms of the droplet volume, the droplet emergence location, contact angle of the base and the sidewall, and the trapezoid channel angle.

In the above analysis, the gravitational force is neglected. This assumption is valid for droplets with a B_o (ratio of gravity to surface tension forces) less than 0.3 [132]. For water droplets at standard earth gravity, this results in a limiting droplet radius of 1.5 mm. In addition, the droplet jumping to the sidewall occurred because the base material used had higher a contact angle than the sidewall material. Therefore, for the droplet to jump, the surface energy of the sidewall needs to be lower than the base. To understand the effect of surface energies on droplet behavior, a Gibbs free energy analysis was performed on the droplet in two states: (a) just before the jump and (b) as it hangs from the sidewall.

5.1.1 **Condition 1: Droplet Sitting on the Base Wall before Jumping to the Sidewall**

The maximum radius R_{C_1} that is associated with the droplet volume just before it jumps to the sidewall is first determined. For this analysis, the following parameters, as shown in Figure 5.2, are defined:

θ is the static contact angle of the base wall.

2α is the open angle between the wall and the base.

a is the distance to the droplet emergence location from the channel corner.

x is the distance from the channel corner to where the droplet contacts the sidewall (D) right before it jumps.

b is the vertical distance from the center of the sphere which constitutes the droplet to the base of the channel.

c is the distance from center of the droplet to the base such that it makes an angle δ with the base and is in line with the radius of the droplet, R_{C_1}.

d and e are the vertical and horizontal distances from the tangent point D to the center of the droplet respectively.

β is the inner open angle made by the radius R_{C_1} with the base of the channel.

The relationship between the above–mentioned angles is given in detail in Appendix II.

The channel open angle is related to the droplet critical radius as

$$tan\, 2\alpha = \frac{R_{C_1}\, sin\, \beta + R_{C_1}\, sin\, \delta}{a - R_{C_1}\, cos\, \delta} \qquad [5.1]$$

From Eq. 5.1, the maximum radius of the droplet R_{C_1} just before it snaps and jumps to the sidewall is obtained. A detailed derivation of R_{C_1} is given in Appendix II.

$$R_{C_1} = \frac{a\, sin\, 2\alpha}{1 - (cos\, \theta\, cos\, 2\alpha)} \qquad [5.2]$$

Figure 5.3 shows two images from the experimental video, where point D acts as the midpoint around which the droplet hangs when it is pulled towards the sidewall. The droplet jumping condition is dependent on the distance x. Detailed derivation of x is given in Appendix II.

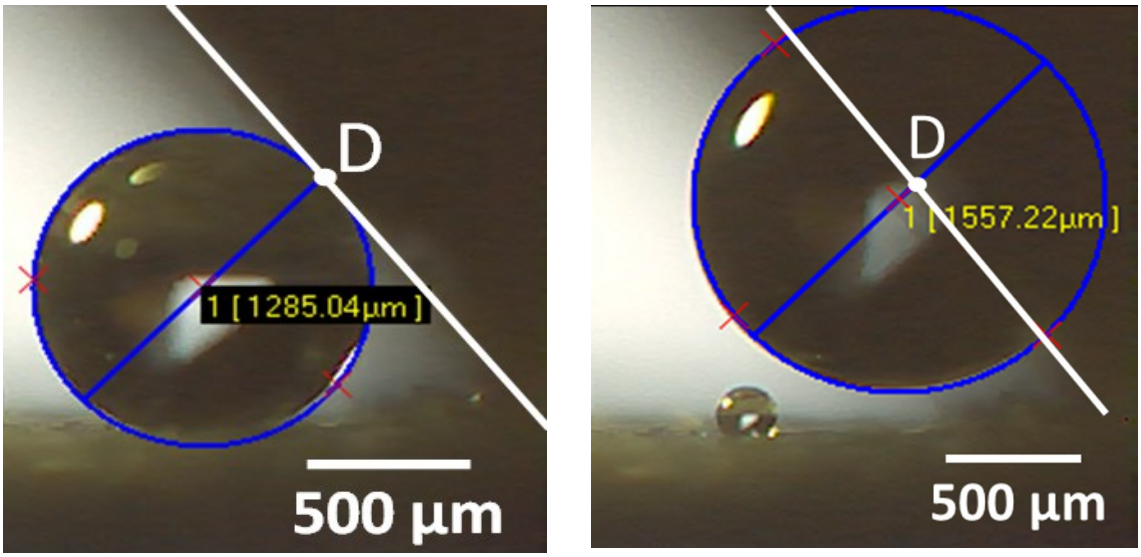

(a) (b)

Figure 5.3: (a) Image of a droplet right before it jumps to the sidewall (b) Image of a droplet hanging from the sidewall right after it jumped. Point D is the midpoint of where the droplet hangs after it jumps to the sidewall

$$x = \left[R_{C_1}{}^2(cos\ 2\alpha - cos\ \theta)^2 + \left(a - R_{C_1}\ sin\ 2\alpha\right)^2\right]^{1/2} \quad [5.3]$$

The next step is to find the actual radius R_2 of the droplet when the droplet hangs from the sidewall after it jumps.

5.1.2 **Condition 2: Droplet Hanging from the Sidewall After the Jump**

To find the radius R_2 when the droplet hangs from the sidewall, the volume of the droplet right before it jumped (V_1), and the volume of the droplet just after it jumped (V_2) are equated. The volume of the droplet while sitting on the base right before the jump as shown in Figure 5.2 is given as:

$$V_1 = \frac{\pi\left(2{R_{C_1}}^3 - 3\,{R_{C_1}}^3 cos\,\theta + {R_{C_1}}^3\,cos^3\theta\right)}{3} \quad [5.4]$$

The volume of the droplet while hanging from the sidewall is given as

$$V_2 = \frac{\pi}{3}{R_2}^3(2 - \,3\,cos\,\emptyset + cos^3\emptyset\,) \quad [5.5]$$

where $\emptyset$ is the static contact angle of the sidewall. Detailed derivations for V_1 and V_2 are given in Appendix II.

Equating both the volumes V_1 and V_2, R_2 is found to be

$$R_2 = \left(\frac{a\,sin\,2\alpha}{1-(cos\,\theta\,cos\,2\alpha)}\right)\left[\frac{2-3\,cos\,\theta + cos^3\theta}{2-3\,cos\,\emptyset + cos^3\emptyset}\right]^{1/3} \quad [5.6]$$

5.1.3 **Droplet Jumping Criterion Analysis from Geometrical Considerations**

The next step in the derivation process is to determine the maximum radius R_{C_2} as shown in Figure 5.4. The following parameters shown in Figure 5.4 are defined as:

O is the center of the hanging droplet.

x is the distance from the channel corner to the midpoint D around which the droplet hangs from the sidewall.

g is the vertical distance from the center of a droplet with radius R_{C_2} to the channel sidewall.

η is the angle made by line g with the sidewall at point C.

f is the distance between the points D and C.

z is the distance from the center of the droplet to the midpoint D on the sidewall.

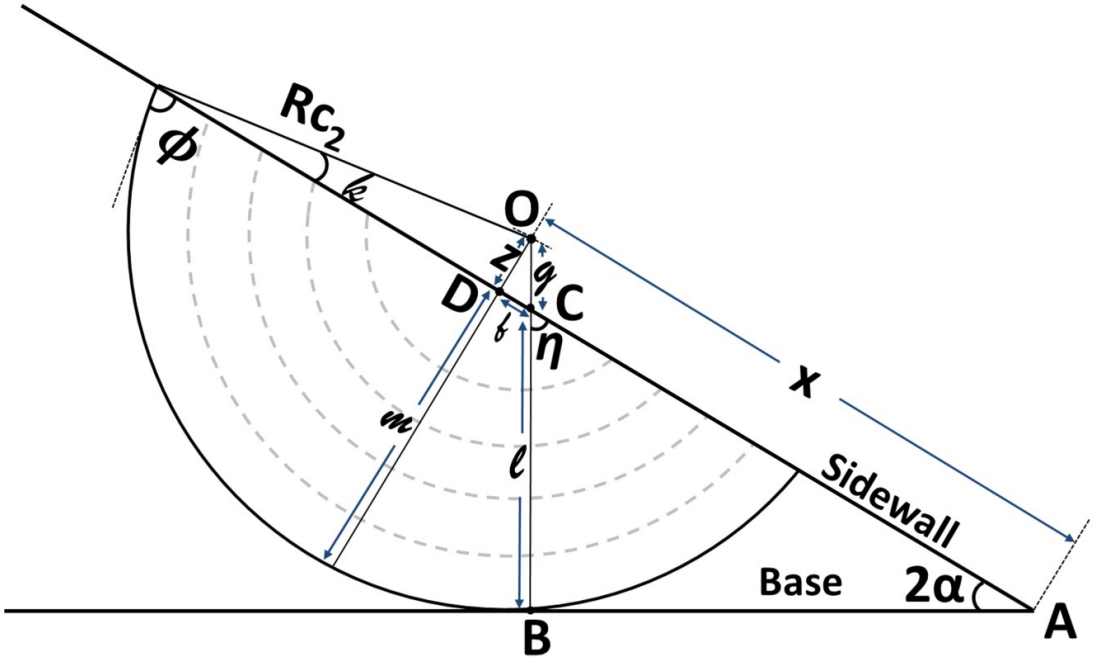

Figure 5.4: Representation of a droplet having the maximum radius (R_{C_2}) while hanging from the sidewall such that the droplet just touches the base of the channel. It is assumed that the droplet is a part of a sphere and also neglecting the gravitational effect on the droplet since the droplet sizes used are very small.

$$sin\,2\alpha = \frac{R_{C_2} - \left(\frac{R_{C_2}\,cos\,\phi}{cos\,2\alpha}\right)}{x - R_{C_2}\,cos\,\phi\,tan\,2\alpha} \qquad [5.7]$$

Derivation for Eq. 5.7 is given in Appendix II.

Therefore, by rearranging Eq. 7, R_{C_2} in terms of 2α and φ is found.

$$R_{C_2} = \frac{\left[{R_{C_1}}^2\,(\,cos\,2\alpha - cos\,\theta\,)^2 + \left(a - R_{C_1}\,sin\,2\alpha\right)^2\right]^{1/2}\,sin\,2\alpha}{(1 - cos\,\phi\,cos\,2\alpha)} \qquad [5.8]$$

Substituting R_{C_1} in Eq. 5.8

$$R_{C_2} = \frac{\left[\left(\frac{a\ sin\ 2\alpha}{1-(cos\ \theta\ cos\ 2\alpha)}\right)^2 (\ cos\ 2\alpha - cos\ \theta\ )^2 + \left(a - \left(\frac{a\ sin^2 2\alpha}{1-(cos\ \theta\ cos\ 2\alpha)}\right)\right)^2\right]^{1/2} sin\ 2\alpha}{(1-cos\ \phi\ cos\ 2\alpha)} \quad [5.9]$$

It can be seen from Eq. 5.8 that R_{C_2} is a function of R_{C_1}, the distance of the droplet emergence location from the channel corner *a*, the channel open angle *2α*, and the base and sidewall contact angles θ and $\emptyset$, respectively. The droplet jumping condition is thus defined as follows.

(a) $R_2 \leq R_{C_2}$ – Droplet jumps to the sidewall

(b) $R_2 > R_{C_2}$ – Droplet bridges the base and channel wall

Equating Eq. 5.6 and 5.9, the criterion for droplet jumping is obtained

$$\frac{R_2}{R_{C_2}} = \frac{\left(\frac{a\ sin\ 2\alpha}{1-(cos\ \theta\ cos\ 2\alpha)}\right)\left[\frac{2-3\ cos\ \theta + cos^3\theta}{2-3\ cos\ \emptyset + cos^3\emptyset}\right]^{1/3} (1-cos\ \phi\ cos\ 2\alpha)}{\left[\left(\frac{a\ sin\ 2\alpha}{1-(cos\ \theta\ cos\ 2\alpha)}\right)^2 (\ cos\ 2\alpha - cos\ \theta\ )^2 + \left(a - \left(\frac{a\ sin^2 2\alpha}{1-(cos\ \theta\ cos\ 2\alpha)}\right)\right)^2\right]^{1/2} sin\ 2\alpha} \leq 1 \quad [5.10]$$

Eq. 5.10 gives the condition to determine whether the droplet jumps to the sidewall or not. For any given material at a given channel open angle and droplet emergence location, the droplet behavior in the channel can be identified using this criterion.

The Concus–Finn condition is able to predict the channel corner filling and non–filling behavior. However, it is not able to predict the droplet jumping behavior. Therefore, to understand how a droplet will behave in a system for a given material pair,

first check if $R_2/R_{C_2} \leq 1$. If this criterion is satisfied, then the droplet will jump to the sidewall. If this condition is not satisfied, then the droplet will enter a corner filling or non–filling condition, which could be predicted using the Concus–Finn condition.

5.1.4 **Experimental Results**

To validate the criterion derived for determining the droplet jumping behavior, experiments were performed on different base and wall materials. A preferential pore of 100 μm was made on the base material for the droplet to emerge at a known location. The distance between the preferential pore and the channel corner was varied between 0.5 and 2.5 mm during the experiments and the droplet dynamics were observed. The channel open angle was varied from 25° – 90°. In these experiments, only one side of the channel wall was used with the GDL base for easier visualization. The experiments were performed such that the droplet size did not exceed 1.5 mm in diameter while sitting on the GDL without touching the walls. The videos were captured using a high–speed Keyence VW–6000 camera at 125 fps, and the droplet dynamics were evaluated. Different set of material pairs used for the base and channel wall, and their theoretical transition angles based on the Concus–Finn condition are given in Table X. The experimental results for the droplet behavior near the channel corners for different material pairs and different open angles are summarized in Table XI. Fig. 5 shows the plot of R_2/R_{C_2} versus the channel open angle for different tests performed. Fig. 5 validates the use of the proposed jumping criterion with the experimental data for different sets of

materials used. Around 180 experimental data points were collected and analyzed. In the plot, points show experimental data and a dotted line shows the theoretical prediction. The droplet jumping criteria for 6 different material pairs were calculated using Eq. 5.10.

Table X: Transition angles calculated using Concus–Finn condition for different material pairs used for the base and sidewall of the channel

Base Material	Sidewall Material	Transition Angle
SGL–25BC	Polycarbonate	54°
SGL–25BC	PTFE (PolyTetraFluoroEthylene)	82°
PTFE	Polycarbonate	20°
PTFE	Aluminum	29°
SGL–25BC	Aluminum	63°
SGL–25BC	Rough Polycarbonate	51°

Table XI: Comparison of the experimental results for corner filling and non–filling with the Concus–Finn condition

Material Pair	Droplet Emergence Location	Channel Angle	Concus–Finn based Transition Angle	Experimental Results
SGL–25BC Base and Polycarbonate Sidewall	2.1	25	54°	No Fill
	2.5	30		No Fill
	2.0	30		No Fill
	3.45	30		No Fill
	5.6	30		No Fill
	6.5	30		No Fill
	1.4	40		Jump
	1.6	45		No Fill
	1.7	45		No Fill
	3.0	45		No Fill
	4.2	45		No Fill
	4.0	45		No Fill
	1.6	50		Jump
	1.4	52		Jump
	1.7	50		No Fill
	2.5	50		No Fill
	4.0	50		No Fill
	5.2	50		No Fill
	2.4	60		Jump
	1.0	60		Jump
	1.5	60		Jump
	2.9	60		Fill
	3.5	60		Fill
	1.5	90		Fill
	1.7	90		Fill
	2.0	90		Fill
	2.9	90		Fill
	3.4	90		Fill

SGL–25BC Base and PTFE Sidewall	1.7	30	82°	No Fill
	3.0	30		No Fill
	2.0	30		No Fill
	5.4	30		No Fill
	4.8	30		No Fill
	1.5	45		No Fill
	2.4	45		No Fill
	4.3	45		No Fill
	6.3	45		No Fill
	3.4	45		No Fill
	2.3	50		No Fill
	3.1	50		No Fill
	3.7	50		No Fill
	5.2	50		No Fill
	4.56	50		No Fill
	2.5	60		No Fill
	3.4	60		No Fill
	2.0	60		No Fill
	4.2	60		No Fill
	5.0	60		No Fill
	1.6	90		Fill
	2.0	90		Fill
	2.5	90		Fill
	2.9	90		Fill
	3.3	90		Fill

PTFE Base and Polycarbonate Sidewall	1.1	30	20°	Fill
	2.6	30		Fill
	2.5	30		Jump
	2.3	30		Fill
	3.5	30		Fill
	1.7	45		Fill
	2.1	45		Fill
	2.6	45		Fill
	3.1	45		Fill
	2.4	45		Fill
	1.4	50		Fill
	2.6	50		Fill
	2.5	50		Fill
	4.0	50		Fill
	1.89	50		Fill
	0.7	60		Fill
	2.3	60		Fill
	1.3	60		Fill
	2.0	60		Fill
	3.4	60		Fill
	0.5	90		Fill
	0.9	90		Fill
	1.5	90		Fill
	1.9	90		Fill
	0.6	90		Fill

PTFE Base and Aluminum Sidewall	2.5	30	29°	Fill
	5.0	30		Fill
	4.8	30		Fill
	4.0	30		Fill
	2.8	30		Fill
	3.4	45		Fill
	5.0	45		Fill
	2.7	45		Fill
	3.3	45		Fill
	2.5	45		Fill
	3.5	50		Fill
	2.5	50		Fill
	2.4	50		Fill
	1.5	50		Fill
	2.0	50		Fill
	2.4	60		Fill
	2.6	60		Fill
	2.0	60		Fill
	1.5	60		Fill
	3.0	60		Fill
	1.5	90		Fill
	2.7	90		Fill
	3.0	90		Fill
	3.2	90		Fill
	3.5	90		Fill

SGL–25BC Base and Aluminum Sidewall	3.3	30	63°	No Fill
	4.6	30		No Fill
	5.6	30		No Fill
	2.5	30		No Fill
	1.0	30		No Fill
	3.1	45		No Fill
	2.5	45		No Fill
	3.5	45		No Fill
	5.6	45		Jump
	2.4	45		No Fill
	1.7	50		No Fill
	2.4	50		No Fill
	3.4	50		Jump
	3.6	50		No Fill
	2.0	50		No Fill
	2.0	60		No Fill
	1.5	60		No Fill
	3.0	60		No Fill
	3.5	60		Jump
	1.0	60		Jump
	0.5	90		Fill
	1.0	90		Fill
	1.3	90		Fill
	2.0	90		Fill
	2.8	90		Fill

SGL–25BC Base and Rough Polycarbonate Sidewall	0.2	30	51°	No Fill
	1.0	30		No Fill
	1.9	30		No Fill
	3.0	30		No Fill
	3.5	30		No Fill
	1.7	45		No Fill
	1.0	45		No Fill
	3.0	45		No Fill
	4.3	45		No Fill
	2.0	45		No Fill
	1.35	50		No Fill
	2.2	50		No Fill
	2.9	50		Jump
	3.0	50		Jump
	3.5	50		Jump
	1.3	60		Fill
	0.4	60		Fill
	1.0	60		Fill
	2.0	60		Fill
	2.5	60		Fill
	1.5	90		Fill
	2.0	90		Fill
	2.9	90		Fill
	3.5	90		Fill
	1.0	90		Fill

Figure 5.5(a) shows the experimental values and the theoretical predictions for an SGL–25BC base and polycarbonate sidewall. All three behaviors (droplet jumping, corner filling and non–filling) were observed during experiments for different channel open angles used. It was observed that the theoretical value of R_2/R_{C_2} for 40°, 50°, 52° and

60° channel corner angles also fell below 1 indicating that the droplet would jump to the sidewall. The proposed model is thus seen to predict the droplet jumping behavior accurately.

Similar experiments were performed with a SGL–25BC GDL base and a PTFE (PolyTetraFluoroEthylene) sidewall, and the results of which are shown in Figure 5.5(b). Here, only corner filling and non–filling behaviors were observed during the experiments. For an open angle below 60°, no corner filling of the channel corners was observed. At a 90° open angle, the droplet filled the channel corners. It can be seen from Table XI that for this material pair, the transition angle from non–filling to filling is at 82°. This means that the droplet will fill the channel corners for open angles above 82° and thus matches with the experimental results.

Figure 5.5(c) is the plot for a PTFE base and a polycarbonate sidewall. Since the transition angle for this material pair is 20°, the entire range of open angles used for experiments should show corner filling. It was seen that corner filling behavior occurred for most of the open angles used in the experiment. However, at a 30° open angle, the droplet jumped to the channel sidewall. Using the proposed jumping criterion, the R_2/R_{C_2} value for this case was calculated and it was observed that the value was below 1, indicating that the droplet should jump.

Similarly, for a PTFE base and aluminum sidewall, no jumping behavior was observed for any channel angles used. Only corner filling behavior was observed

experimentally for open angles greater than 30°, as shown in Figure 5.5(d). None of the points fell below the proposed criterion, suggesting that the droplet would not jump under any conditions. Hence, the experimental results matched with the theoretical prediction. Also, according to the Concus–Finn condition, channel corner filling should occur for open angles greater than 29°. Thus, experimental results match with the Concus–Finn predictions as well.

Figure 5.5(e) shows the results for a SGL–25BC base and aluminum sidewall. All three possible behaviors (droplet jumping, corner filling and non–filling of the channel corners) were observed for different open angles used. Droplet jumping behavior was observed at 45°, 50° and 60° open angles, which are not near the transition angle for this material pair. However, using the proposed criterion, droplet jumping was predicted accurately. From the experiments, it was seen that the droplet filled the channel corners for open angles above 60° and did not fill the channel corners for angles below 60°. The experimental results were in accordance with Concus–Finn condition.

Similar results were also obtained for a SGL–25BC base and rough polycarbonate sidewall. Experimental results are shown in Figure 5.5(f). Again all the three possible behaviors, droplet jumping, corner filling and non–filling of the channel corners, were observed for different channel open angles used. Droplets showed jumping behavior at a 50° channel angle. Using the proposed criterion, droplet jumping behavior was predicted accurately. Droplets showed corner filling behavior at angles above 60° and no corner filling at angles below 50°, which are in accordance with the Concus–Finn condition.

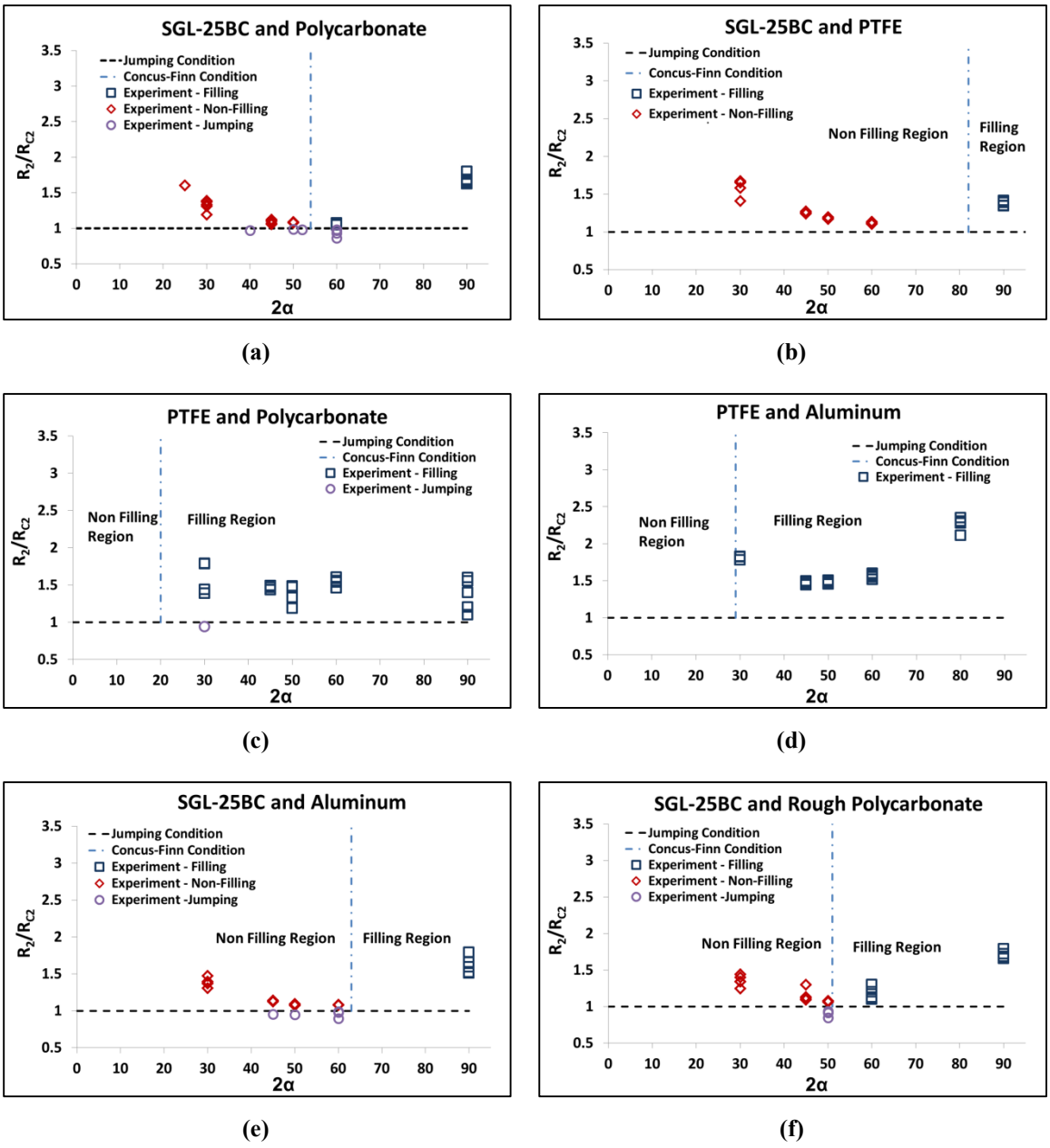

Figure 5.5: Graphical representation of the proposed criterion to predict the droplet jumping behavior in a PEMFC gas channel. The experimental points falling below the proposed criterion shown by a dashed line, led to droplet jumping. Droplet transition from non–filling to filling of the channel corner based on the Concus–Finn condition is plotted by the dot–dash line. Any points falling on the right side of the dot–dash line showed corner filling of the channel and points falling on the left side of the dot–dash line showed no corner filling behavior by the droplet. 96% of the experimental data matched the theoretically predicted behavior.

Comparing the R_2/R_{C_2} data results for all the material pairs used it was seen that the proposed theoretical model was able to predict the droplet-corner interaction for more than 96% of the cases. To understand why the droplet jumps to the sidewall an energy balance on the droplet while sitting on the base wall and while hanging from the sidewall was performed. This is similar to the droplet spreading analysis performed on a surface to understand the wetting behavior of a droplet [31, 145, 162-170]. Detailed explanation of the energy balance and the results are presented in Section 5.1.5.

It is noted from the proposed criterion that the droplet jumping behavior depends on the channel open angle, material properties and droplet emergence location in the channel. Among these parameters, droplet emergence location plays a major role in the droplet behavior near the channel corner. When the droplet emerges very close to the channel corner, the droplet does not have enough room to jump and hang from the sidewall. Instead, it touches the sidewall and forms a bridge between the sidewall and the base as shown in Figure 5.6.

Figure 5.6 shows the droplet jumping image sequence for an SGL–25BC base and aluminum sidewall with a 45° corner angle where the droplet emergence is very close to the channel corner. Figure 5.6(a) shows the emergence of a droplet from the GDL base very close to the channel corner. Figure 5.6(b) shows the image of the droplet when it contacts the sidewall right before it jumps. Once contact is made with the sidewall, the droplet quickly moves towards the sidewall, as shown in Figure 5.6(c), and then jumps, as shown in Figure 5.6 (d). However, due to the small clearance between the base and the

sidewall near the channel corner, the droplet bridges between the two walls as shown in Figure 5.6 (e). When a droplet emerges near the channel corner (less than 0.1 mm away from the corner) or under the land area, it leads to corner filling behavior [91]. Corner filling is an important issue in a PEMFC gas channels and determines the two–phase flow patterns and the oxygen transport resistance at the GDL–channel interface. in light of this, PEMFC gas channel design needs to be modified so that the water emerging from the GDL surface into the channel is removed efficiently.

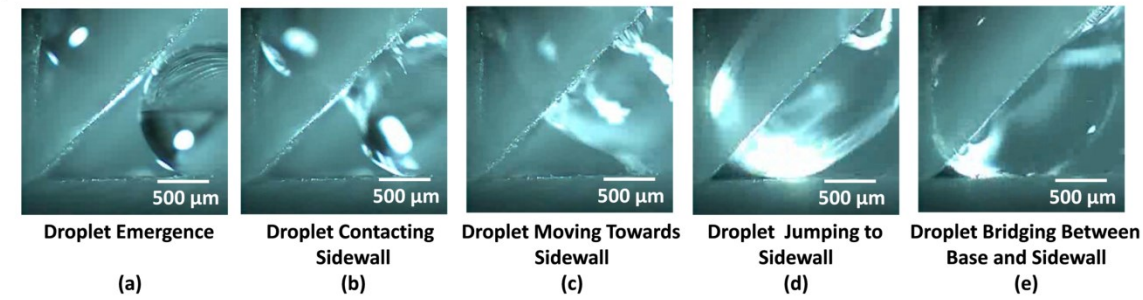

Figure 5.6: Image sequence for a SGL–25BC base and aluminum sidewall showing droplet jumping behavior in a 45° channel. The droplet radius R_2 while hanging from the sidewall is greater than maximum radius that droplet could have while hanging from sidewall (R_{C_2}) which leads to bridging between the base and sidewall.

5.1.5 **Explanation of Droplet Jumping Through Energy Considerations**

At any given time, a droplet's preference is to remain in a lower energy state. Therefore, for the droplet to jump to the sidewall, the energy of the droplet while it sits on the base should be higher than when it hangs from the sidewall. To understand how the surface energies affect the droplet jumping behavior, the Gibbs free energy for the droplet under states (a) just before the jump, and (b) the final hanging position was

calculated for the experimental data that showed droplet jumping behavior. The total surface energy of the droplet is expressed as follows.

$$G_0 = \sigma_{LV} A_{LV} - A_{SL} \cos\theta_r \quad [5.11]$$

$$cos\,\theta_r = \frac{(\sigma_{SV} - \sigma_{SL})^{eff}}{\sigma_{LV}} \quad [5.12]$$

where σ_{LV} , σ_{SL} and σ_{SV} represents the surface tension of the liquid–vapor interface, solid–liquid interface and solid–vapor interface respectively. A_{LV} and A_{SL} represent the surface area of the liquid–vapor interface and the solid–liquid interface of the droplet, respectively [145, 157]. For a composite surface $\theta_r = {\theta_r}^C$, and for a wetted contact surface $\theta_r = {\theta_r}^W$. As the experiments were performed at room temperature, the corresponding surface tension σ_{LV} value used was 72.8 x 10^{-3} N/m. Using Eq. 5.11 and 5.12, the surface energies for conditions 1 and 2 were found. The effect of deformation due to gravity was neglected due to the small droplet size, as shown in Fig 3 [132].

For the droplet to jump from the base to the sidewall there is some amount of work done against gravity. An energy balance for the two states is given by the following Eq.

$$G_{0,Droplet\ \ On\ Base} = G_{0,Hanging\ \ Droplet} + E_{Gravity} + Losses \quad [5.13]$$

where $G_{O,\ Droplet\ On\ Base}$ = Gibbs free energy when the droplet is sitting on the base.

$G_{O,\ Hanging\ \ Droplet}$ = Gibbs free energy when the droplet is hanging from the sidewall.

$E_{Gravity}$ = Energy required by the droplet to move against gravity from the base to the sidewall (Potential Energy).

$Losses$ = Losses mainly due to viscous dissipation.

To calculate $E_{Gravity}$, the centers of mass of the droplet while sitting on the base and while hanging from the sidewall are determined. The vertical distance between the two centers of mass is then calculated and used as the height the droplet moved against gravity. Equating all the different energy terms, the energy loss due to viscous dissipation is calculated. The different energy values calculated for different test conditions where the droplet jumped to the sidewall are shown in Table XII. The radii for different material pairs when the droplet is sitting on the base surface and when it is hanging from the sidewall are given by R_{C_1} and R_2 respectively. Using these radii, the surface area of the liquid–vapor interface of the droplet is found. From the surface area values, the Gibbs free energy of the droplet while sitting on the base and while hanging from the sidewall is determined. It can be seen from Table XII that the energy while sitting on the base was almost 1.5 times greater than when the droplet was hanging from the sidewall. This shows that the droplet jumps to the sidewall because it prefers the lower energy state. The loss terms are positive and quite small, indicating that the energy approach provides a good explanation for the droplet jumping condition. The maximum energy losses are around 15% of the Gibbs free energy when the droplet is sitting on the base. These losses are mainly due to the oscillations before the droplet stabilizes after jumping to the sidewall and the viscous dissipations of the droplet.

Table XII: Different energies associated with the droplet while jumping to the sidewall

No.	Material	Open Angle	Pore Distance (mm)	Droplet Radius R_{C_1} (mm)	Droplet Radius R_2 (mm)	Surface Area of Droplet on Base(mm^2)	Surface Area of Hanging Droplet (mm^2)	Droplet Jump Height (mm)	$G_{0,\text{Droplet on Base}}$ $(J)*10^{-9}$	$G_{0,\text{Hanging Droplet}}$ $(J)*10^{-9}$	$E_{Gravity}$ $(J)*10^{-9}$	Losses $(J)*10^{-9}$
1	SGL–Polycarbonate	40	1.081	0.421	0.718	0.556	0.517	4.05	42.91	18.16	13.59	11.16
2	SGL–Polycarbonate	50	1.04	0.516	0.805	0.819	0.719	4.17	55.89	28.74	23.12	4.03
3	SGL–Polycarbonate	60	1.133	0.562	0.877	1.097	0.845	4.282	93.92	39.25	30.65	24.02
4	PTFE–Polycarbonate	30	0.91	0.414	0.312	0.218	0.164	4.09	12.20	5.70	2.84	3.66
5	SGL–Aluminum	50	2.16	1.071	1.512	3.836	2.506	4.91	326.82	127.24	139.62	59.96
6	SGL–Aluminum	60	1.84	0.813	1.192	2.083	1.385	4.01	126.10	54.20	50.06	21.84

5.1.6 **Pressure Drop and Force Analysis**

The geometrical analysis done to understand the droplet jumping to the sidewall was performed in the absence of airflow in the system. However, in an actual fuel cell, there is airflow in the cell, which produces pressure drop in the presence of liquid water at a given working condition. From experiments performed to understand how the air velocity affects droplet dynamics in the gas channel it was found that the pressure drop value associated with each experimental condition was different [171]. It was observed that with very high air velocities introduced in the system, the droplet would slide off on the GDL without touching the sidewall and be removed from the channel. To encompass all the different forces acting on the liquid, a theoretical analysis was performed to incorporate airflow in the system. Correlations were obtained to understand the minimum velocity and pressure force required in a microchannel system to remove the droplet before it touches the sidewall and after it touches the wall, leading to non–filling or filling of the channel corner. Experimental data shown in Section 4.7 for the 0.4 x 0.7 mm cross section experiments were used for this.

To predict the pressure drop in a trapezoidal channel as a function of air velocity and the channel open angle, a surface plot was developed using Matlab. Figure 5.7 and Figure 5.8 show the pressure drop plots as a function of channel open angles and air velocities for filling and non–filling cases respectively. Similar trends were observed for both.

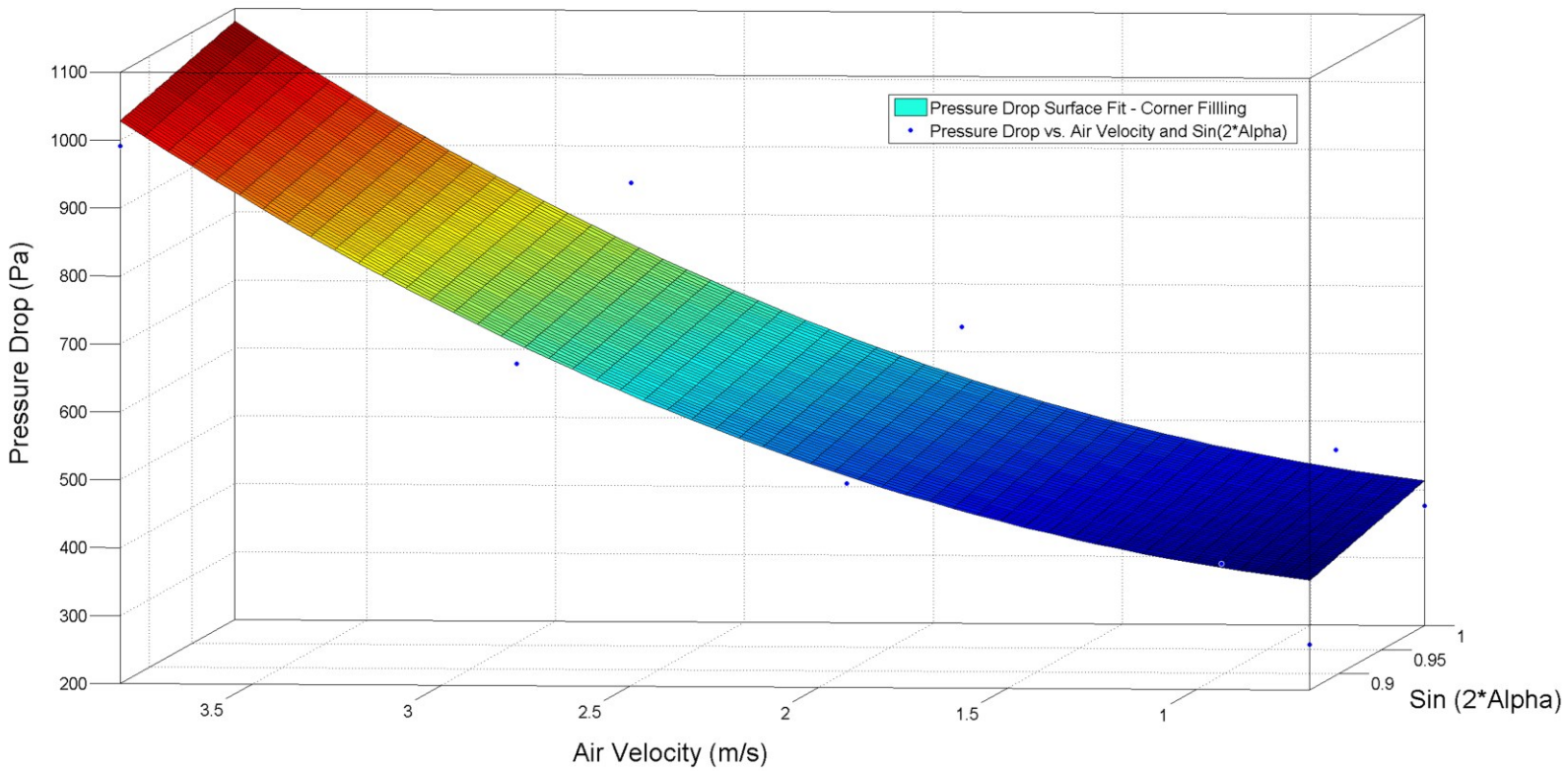

Figure 5.7: Pressure drop surface curve in the gas channel as a function of channel open angle and air velocities for corner filling cases

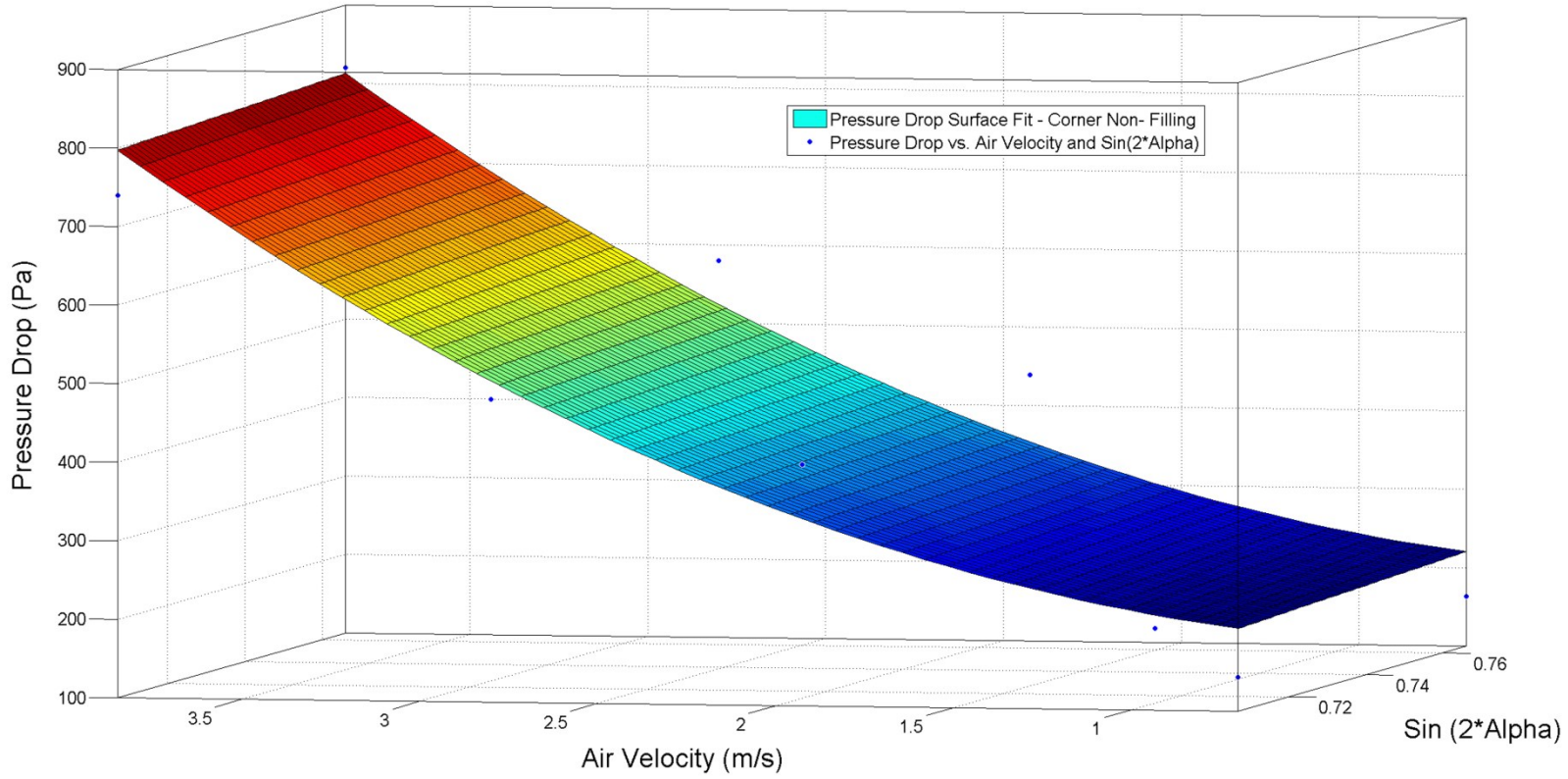

Figure 5.8: Pressure drop surface curve in the gas channel as a function of channel open angle and air velocities for corner non–filling cases

As the air velocity and open angle increase, the pressure drop in the channel goes up. Eq. 5.14 and 5.15 give the correlations obtained for pressure drop in terms of air velocity (v) and channel open angle (2α) for channel corner filling and non–filling cases respectively.

$$\Delta P = 46.56\, sin\, 2\alpha + 390.6\, v^2 - Filling \quad [5.14]$$

$$\Delta P = 41.33\, sin\, 2\alpha + 261.4\, v^2 - Non–Filling \quad [5.15]$$

These correlations provide the minimum pressure drop required in a trapezoid channel for the droplet to be removed when it interacts with the channel walls at air velocities below 4 m/s. The correlations for filling and non–filling cases have $R^2 = 0.96$ and 0.95, respectively. These correlations are specific to the channel geometries investigated.

Droplet dynamics in the gas channel were completely different when the air velocity was increased above 4 m/s. Figure 5.9 shows an image of the droplet removal from a 50° channel at an air velocity of 6.26 m/s. At very high air velocities between 4.1 and 7.23 m/s introduced in channels with different open angles, it was observed that the droplets slid off the GDL surface without touching the sidewalls and were removed from the channel. This was mainly because the air velocities were so high that the drag force on the droplet was considerably higher than to the surface tension force with which the droplet was held on the GDL. To encompass all the forces acting on the droplet at higher air velocities (4.1 – 7.23 m/s), a theoretical analysis was performed to determine the

minimum velocity required in a microchannel for removing the droplet before it touched the sidewall.

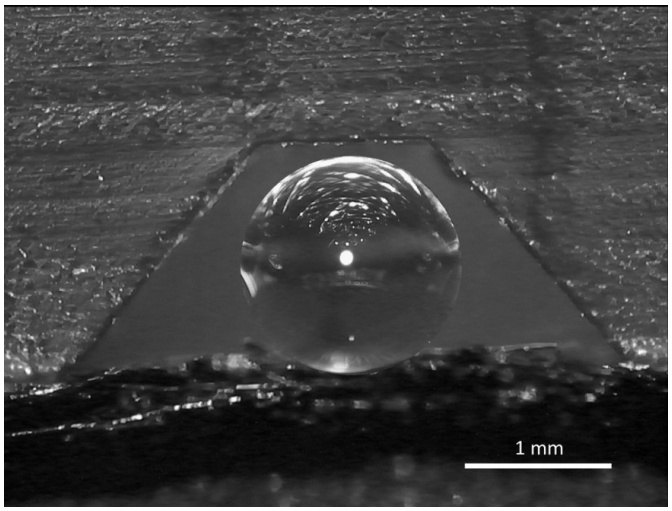

Figure 5.9: Image of a droplet sliding on the GDL and getting removed from the 50° channel without touching the walls of the channel

The analysis consisted of a force balance on the droplet just before it was moved from the GDL surface. Different forces acting on the droplet in a gas channel are shown in Figure 5.10. The gravitational force was neglected in this analysis. As discussed earlier, this assumption is valid for droplets with a B_o less than 0.1 [132]. For water droplets at standard earth gravity, this result in a limiting droplet radius of 1.5 mm. The droplet sizes in this study were observed to be less than 0.4 mm. Since the *Re* used for the experiments was below 250, the airflow in the channel was assumed to be laminar. In addition, the air inside the gas channel was considered to be incompressible. For a fluid to be considered incompressible, the Mach number should be smaller than 0.3. Mach number (*M*) is defined as

$$M = \frac{v}{v_{Sound}} \qquad [5.16]$$

Where v is the velocity of the airflow used in the channel and v_{sound} is the speed of the sound. In dry air at 20 °C, the speed of sound is 343.2 m/s. The maximum velocity of air used in our experiments was 7.23 m/s. Furthermore, all the experiments were performed at room temperature and at 0% RH. Therefore, the M for all the experimental cases used in this analysis was below 0.021. Therefore, the airflow in the gas channel can be considered incompressible.

It can be seen from Figure 5.10 that the drag force (F_D) acts on the droplet in the direction of air flow whereas the surface tension force (F_s) which holds the droplet on the GDL acts in the opposite direction. It was also assumed that the drag force, which is the combination of shear force and the pressure force acting on the droplet, was equal and opposite to the net surface tension force at the instant of droplet removal.

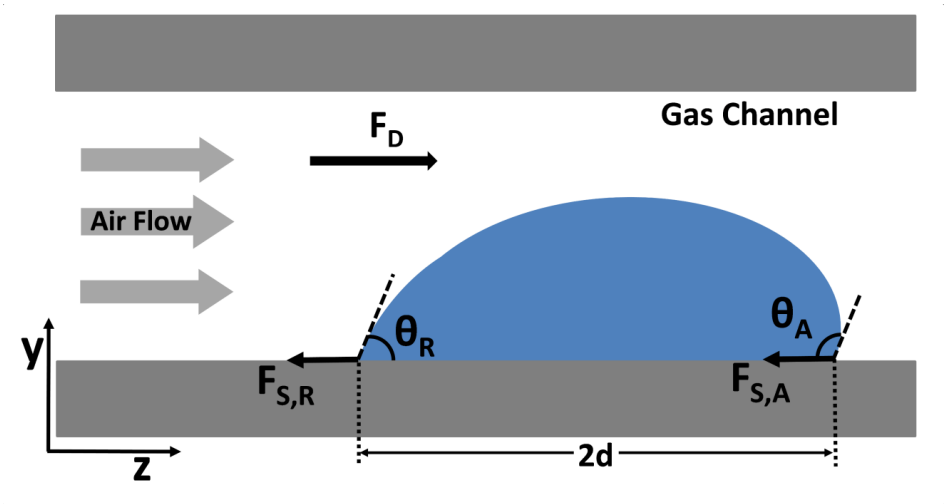

Figure 5.10: Representation of different forces acting on a droplet inside a PEMFC gas channel

$$F_D + F_S = 0 \quad [5.17]$$

Eq. 5.18 gives the drag force acting on the droplet

$$F_D = \frac{1}{2} C_D \rho v^2 A \quad [5.18]$$

where ρ is the density of the air, v is the air velocity, A is the area of the droplet on which the drag force is applied and C_D is the drag coefficient on the droplet which can be estimated using following empirical correlation [120, 172].

$$C_D = \frac{24}{Re} (1 + 0.1925\, Re^{0.63}) \quad [5.19]$$

where, Re is the Reynolds number for the airflow over the droplet.

The area of the droplet on which the drag force is applied was calculated from Figure 5.10 using the front view of the droplet. Figure 5.11 shows only one of the sidewalls of the gas channel for simplicity. The different parameters shown in Figure 5.11 are defined as follows:

θ is the static contact angle of the base wall.

2α is the open angle between the wall and the base.

a is the distance of the droplet emergence location from the channel corner.

β is the inner open angle made by the radius R_{C_1} with the base of the channel.

b is the vertical distance from the center of the sphere which constitutes the droplet to the base of the channel.

γ is the angle made by the radius R_{C_1} with the line b passing through the droplet center to the midpoint of the base where the droplet touches.

c is the distance from the center of the droplet to the sidewall such that it makes an angle δ with the radius of the droplet.

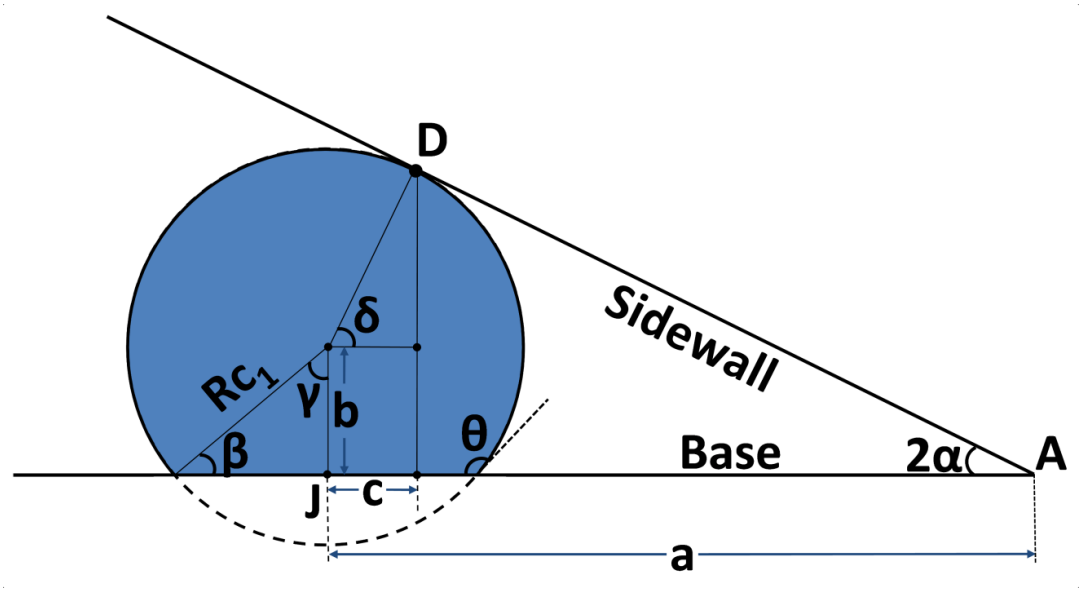

Figure 5.11: Representation of a droplet seen from the front view used for calculating the area on which the drag force is being applied

The base area of the droplet on the GDL surface was calculated as

$$A = R_{C_1}{}^2 \left(\theta - \frac{sin\ 2\theta}{2} \right) \qquad [5.20]$$

The trapezoid channel open angle is related to the droplet critical radius (maximum radius of the droplet before it touches the sidewall) by

$$tan\,2\alpha = \frac{R_{C_1}\,sin\,\beta + R_{C_1}\,sin\,\delta}{a - R_{C_1}\,cos\,\delta} \quad [5.21]$$

From Eq. 5.21, R_{C_1}, the maximum radius of the droplet just before it interacts with the sidewall was obtained.

$$R_{C_1} = \frac{a\,sin\,2\alpha}{1-(cos\,\theta\,cos\,2\alpha)} \quad [5.22]$$

Substituting the area of the droplet and R_{C_1} into Eq. 5.19, the drag force applied on the droplet was obtained.

$$F_D = \frac{1}{2}\,C_D\,\rho\,v^2\,\left(\frac{a\,sin\,2\alpha}{1-(cos\,\theta\,cos\,2\alpha)}\right)^2\left(\theta - \frac{sin\;2\theta}{2}\right) \quad [5.23]$$

Eq. 5.23 gives the total drag force applied on the droplet by the airflow in a trapezoidal gas channel.

The surface tension forces due to advancing ($F_{S,\,A}$) and receding ($F_{S,\,R}$) contact angles are given by

$$F_{S,A} = \sigma.2d.cos\,\theta_A \quad [5.24]$$

$$F_{S,R} = \sigma.2d.cos\,\theta_R \quad [5.25]$$

where σ is the surface tension coefficient and *2d* is the width of the contact line (normal to the air flow direction) of the droplet on the GDL surface.

The net surface tension force F_S and the width 2*d* are given by

$$F_S = F_{S,A} - F_{S,R} \quad [5.26]$$

$$F_S = \sigma . 2d . (\cos\theta_A - \cos\theta_R) \quad [5.27]$$

$$2d = 2R_{C_1} \sin\gamma = 2R_{C_1} \sin\theta \quad [5.28]$$

Substituting 2d values in Eq. 5.27

$$F_S = 2\sigma R_{C_1} \sin\theta (\cos\theta_A - \cos\theta_R) \quad [5.29]$$

Substituting the R_{C_1} value from Eq. 5.22 in Eq. 5.29 gives

$$F_S = 2\sigma \left(\frac{a \sin 2\alpha}{1-(\cos\theta \cos 2\alpha)}\right) \sin\theta (\cos\theta_A - \cos\theta_R) \quad [5.30]$$

Eq. 5.30 gives the net surface tension force holding the droplet on the GDL surface. To find the minimum velocity required to remove the droplet from the gas channel before it interacts with the channel walls, the drag force was equated to the surface tension force.

Since the drag coefficient used in this analysis (Eq. 5.19) is applicable for a spherical droplet and the droplet in this study was not completely spherical, this Eq. cannot be used directly. In addition, Eq. 5.19 is applicable for a uniform velocity profile in the channel whereas in this work, the effect of sidewall also needs to be taken into account. In addition, the radius of the droplet used for this analysis was assumed to be the maximum radius of the droplet before it touched the sidewall. However, in the experiments it was seen that the droplet size varied when it was removed. Therefore, to account for all these assumptions, a rectification factor, K, was introduced in the analysis.

$$F_D = K\, F_S \qquad [5.31]$$

$$\frac{1}{2}\, C_D\, \rho\, v^2 \left(\frac{a \sin 2\alpha}{1-(\cos\theta \cos 2\alpha)}\right)^2 \left(\theta - \frac{\sin 2\theta}{2}\right) = K\left[2\sigma \left(\frac{a \sin 2\alpha}{1-(\cos\theta \cos 2\alpha)}\right) \sin\theta\, (\cos\theta_A - \cos\theta_R)\right] \qquad [5.32]$$

$$v = \sqrt{\frac{K\, 4\, \sigma\, \sin\theta (\cos\theta_A - \cos\theta_R)}{C_D\, \rho \left(\frac{a \sin 2\alpha}{1-(\cos\theta \cos 2\alpha)}\right)\left(\theta - \frac{\sin 2\theta}{2}\right)}} \qquad [5.33]$$

Using the experimental data for droplet removal from the gas channel, a *K* value was determined for MRC–105 with 5% PTFE. It was seen that the *K* value varied from 0.7 to 2 for different trapezoidal channel open angles and the superficial air velocity in the gas channel.

$$K = (0.65 \sin 2\alpha - 0.87) * v + (-6.3 \sin 2\alpha + 8.4) : MRC-105 \qquad [5.34]$$

This *K* value was found to be dependent on the GDL material used in the system. This is mainly because the radius of the droplet used for the analysis was dependent on the contact angle of the base material and hence the *K* was dependent on the GDL material as well. Therefore, different GDL materials were also tested in our experiment (TGP–H–060 and SGL–25BC) and their surface wettability properties such as θ, θ_A, θ_R and $\Delta\theta$ are given in Table III. The *K* values for these GDL materials were also found and are given by Eq. 5.35 and 5.36 respectively. The *K* values found for different GDL materials as a function of air velocity and channel open angle. The surface plot for K values for MRC-105, SGL-25BC and TGP-H-060 as a function of superficial air velocity and channel open angle is shown in Figure 5.12.

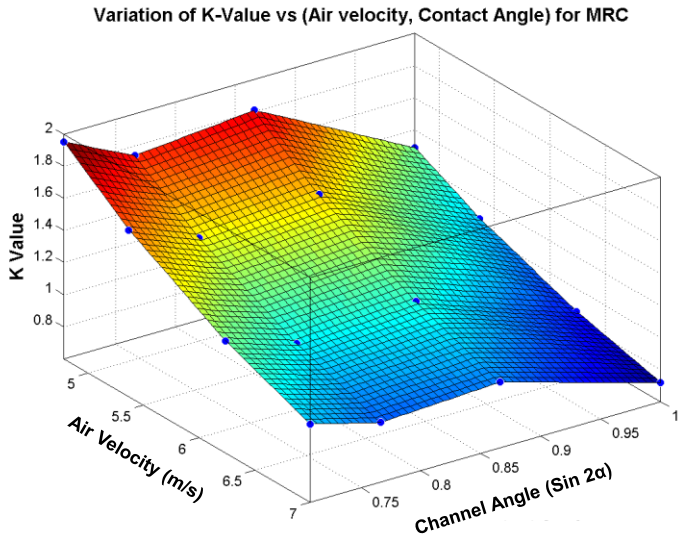
Variation of K-Value vs (Air velocity, Contact Angle) for MRC
K Value
2
1.8
1.6
1.4
1.2
1
0.8
Air Velocity (m/s)
5
5.5
6
6.5
7
Channel Angle (Sin 2α)
0.75
0.8
0.85
0.9
0.95
1

(a)

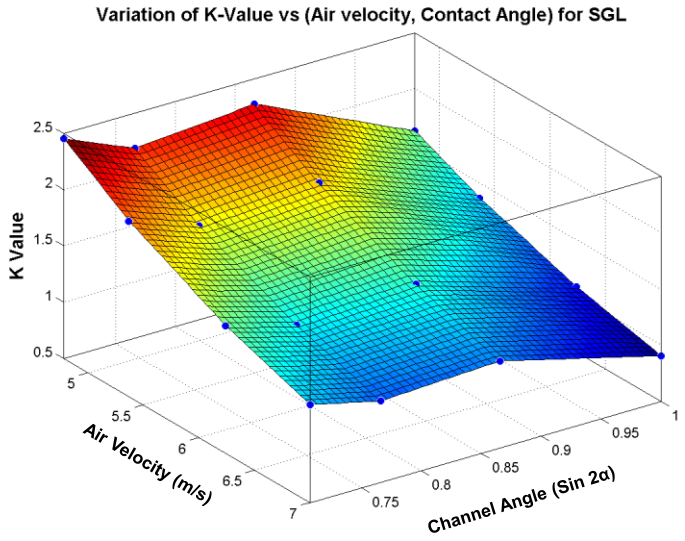
Variation of K-Value vs (Air velocity, Contact Angle) for SGL
K Value
2.5
2
1.5
1
0.5
Air Velocity (m/s)
5
5.5
6
6.5
7
Channel Angle (Sin 2α)
0.75
0.8
0.85
0.9
0.95
1

(b)

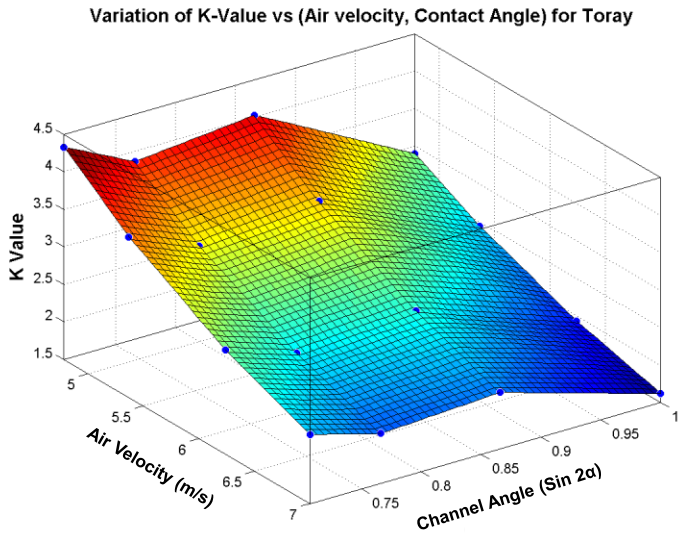

(c)

Figure 5.12: Surface plot of K value as a function of superficial air velocity and sin (2*α*) for different GDL material (a) MRC-105 (b) SGL-25BC (c) TGP-H-060.

To show clearly how the air velocity and channel open angle affect the *K* value separately for different GDL materials, *K* values for different GDL materials were plotted against superficial air velocity for different channel open angles (Figure 5.13(a)) and against channel open angle for different superficial air velocities (Figure 5.13(b)). It is seen from the graph that the *K* value increases linearly with increase in air velocity for all GDL materials. However, the *K* value is similar for SGL-25BC and MRC-105 but for TGP-H-060 the *K* value is slightly higher. This increase in *K* for TGP-H-060 can be attributed to the $\Delta\theta$ of the GDL material. The $\Delta\theta$ for TGP-H-060 is around 17° whereas for SGL-25BC and MRC-105 it is around 10°. Therefore, it requires larger drag force for it to remove the droplet from the gas channel.

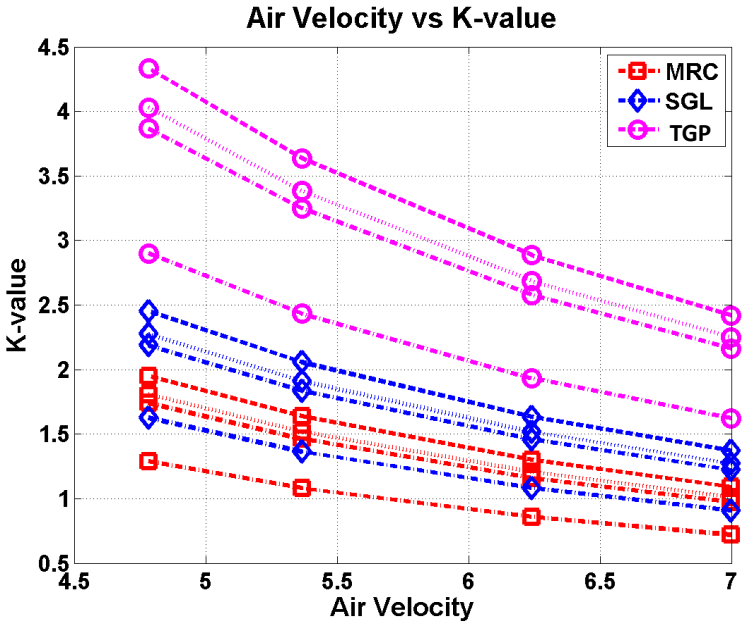

(a)

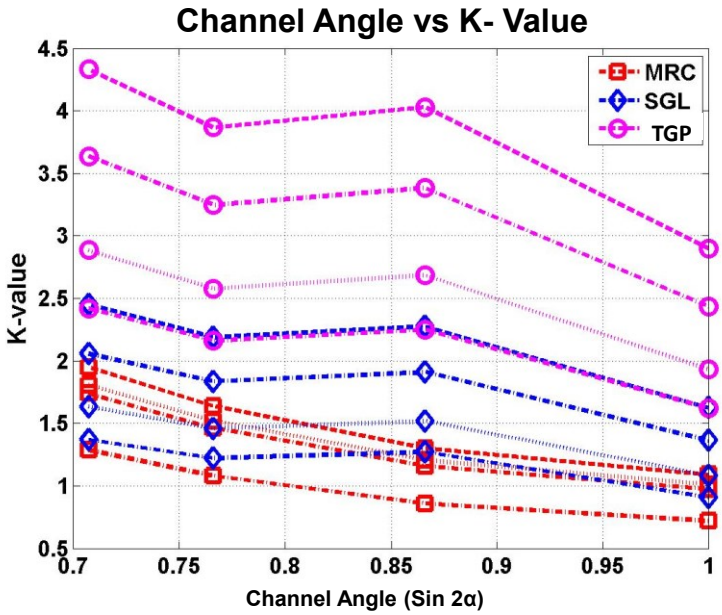

(b)

Figure 5.13: K values plotted for different GDL materials as a function of (a) air velocity and (b) channel angle

Based on this, correlations were proposed for the rectification factor for TGP-H-060 and SGL-25 BC and are given by Eq. 5.35 and 5.36.

$$K = (0.4\,sin\,2\alpha - 0.66) * v + (-3.88\,sin\,2\alpha + 6.47) : TGP\text{–}H\text{–}060 \quad [5.35]$$

$$\mathrm{K} = (0.88\,\sin 2\alpha - 1.5) * \mathrm{v} + (-8.3\,\sin 2\alpha + 14.3) : \mathrm{SGL\text{–}25BC} \quad [5.36]$$

To validate the correlation proposed for different GDL material, the experimental data and the theoretical prediction were plotted together as shown in Figure 5.14. It can be seen from the figure that the correlation value was within an error of 12% for all the different *K* values.

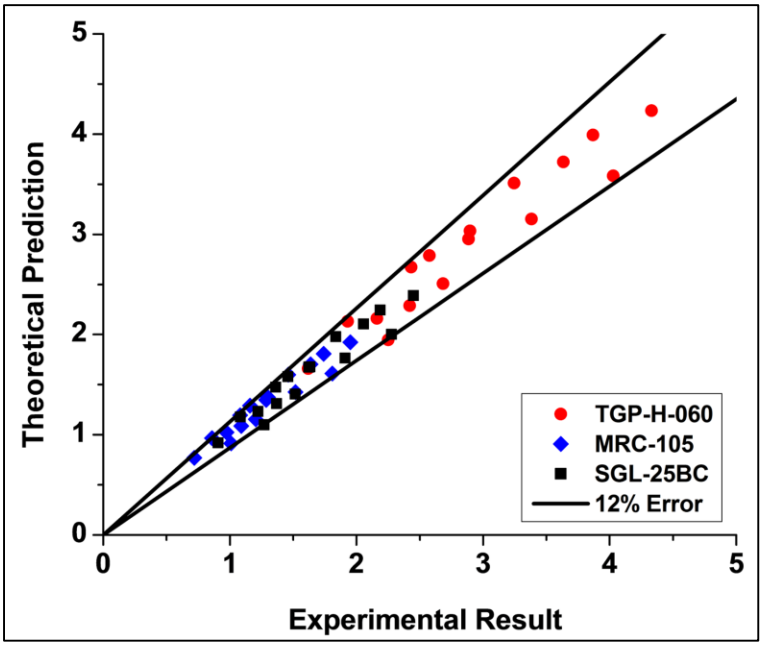

Figure 5.14: *K* values found for different GDL materials based on experimental data and from theoretical prediction. The black line in the plot indicates the 12% error boundary. The data points fall within the 12% error boundary between the experimental and theoretical prediction.

In this study, a semi-empirical correlation was obtained to find the minimum velocity required in a given trapezoidal gas channel to remove the liquid water before the touches the channel sidewall. The correlation for K obtained in this analysis is specific to the experiments performed in this study. For channels with different aspect ratio or hydraulic diameter, the constant K would change and that needs to be found experimentally.

This study clearly indicates the important role played by the channel sidewalls and the channel angle on water transport characteristics. Knowing the previously mentioned parameters (contact angle of the base and the sidewall material, channel open angle and droplet emergence location) for a given system, the minimum velocity required to remove the droplet from the channel before it touches the channel walls can be found using Eq. 5.33. In addition, if the inlet gas velocity in the channel is known, the minimum pressure drop required to remove the droplet from the gas channel when the droplet touches the channel walls can be found out using Eq. 5.14 or 5.15.

Chapter 6 Conclusions

In a PEMFC, efficient water removal from the gas channel is one of the key issues that needs to be addressed. In this study, *ex situ* experiments were conducted to study water droplet dynamics in a gas channel from a fundamental perspective. High–speed videos revealed that droplet dynamics at the gas channel corner are significantly affected by the changes in (i) the trapezoid channel angle, (ii) air velocities, (iii) channel material, and (iv) droplet inlet location. Therefore, experiments were conducted to understand the effect of each parameter separately on droplet behavior. Experiments were also conducted to understand the effect of channel scaling on the droplet behavior. It was also seen from the experiments that in the absence of airflow, a droplet emerging from the channel base jumped to the sidewall such that it completely lost contact with the base and hung from the sidewall. Therefore, theoretical models were developed to understand this jumping mechanism and to characterize droplet behavior inside PEMFC gas channels as a function of the above four parameters. The effects of different parameters on droplet dynamics are summarized below.

- **Effect of Channel Angle** – It was observed from the experiments that for channel open angles of 50° and below, the droplet did not fill the channel corners, and did fill the corners for higher open angles. The surface energies of the channel wall and base material influence the corner filling behavior of the channel at a given channel open angle. Experimental results confirmed the Concus–Finn theoretical

predictions regarding the corner filling behavior. However, near the transition angle based on the Concus–Finn condition, droplet behavior changed due to oscillations in the droplet created by the air velocity inside the channel. It was noted that using the instantaneous dynamic contact angle was necessary while applying the Concus–Finn condition.

- **Effect of Air Velocity** – Airflow inside the channel introduces oscillations in the droplet before it touches the channel sidewall, and significantly affects the instantaneous dynamic contact angle the droplet makes with the channel sidewall. This dynamic contact angle determines the corner filling and non–filling criteria for a given channel angle. For the channel open angles that fall near the transition angle, the airflow has significant effect in determining the channel corner filling behavior. At the transition angle, lower air velocities result in channel corner filling while higher ones do not.

- **Effect of Channel Material –** Different channel materials used in PEMFC applications were observed to have similar characteristic behavior in terms of droplet pinning and transport resistance in the channel. For all the material pairs used in this study, the transition angle was noted to be 50°. Any channel having an open angle of 50° or smaller did not fill the channel corners when run at higher air velocities corresponding to higher current densities. No noticeable difference

was observed for different GDL materials tested in terms of the corner filling behavior.

- **Effect of GDL Degradation –** GDL samples that had run longer showed lower advancing and receding contact angles. This clearly shows that the GDL loses its hydrophobicity with use. This loss in hydrophobicity affects the corner filling behavior and hence shifts the transition angle according to the Concus–Finn condition.

- **Effect of Scaling of the Channel –** Scaling of the channel did not affect the droplet behavior in the PEMFC gas channel. Smaller channels (0.4 mm × 0.7 mm) showed the same droplet dynamics in terms of corner filling behavior as observed in a larger dimension channel (3 mm × 3 mm). The liquid flow pattern observed in the gas channel changed from slug to film to droplet flow depending upon the trapezoid channel angle and the air velocity inside the channel.

- **Effect of Droplet Location** – Droplet dynamics in the channel were also dependent on the liquid emergence location within the channel. Predicting the filling and non–filling criteria of the channel based on Concus–Finn condition works well only when the droplet emerges in the middle of the channel. When the droplet emerges close to the channel corners or under the land areas, the Concus–Finn condition based on static contact angle fails to predict the droplet behavior

near the channel corners. Instead, it was noted that using the instantaneous dynamic contact angle while applying the Concus–Finn condition predicted the droplet behavior in the channel accurately.

- **Theoretical Model –** To incorporate all the different droplet behaviors due to the different parameters mentioned above, a geometrical analysis as well as a force balance analysis was performed. Geometrical analysis was helpful in understanding the droplet jumping behavior observed in the gas channel while there was no airflow in the gas channel. A correlation was obtained to predict the droplet jumping behavior in terms of the channel open angle, material surface properties and droplet inlet location. In the presence of airflow, the droplet showed corner filling or non–filling behavior at lower air velocities whereas the droplet slid off the GDL surface at higher air velocities. For these cases, a semi-empirical correlation was obtained to predict the minimum pressure drop as well as minimum velocity required to remove the droplet from the gas channel. All of these models were validated by experimental results.

Chapter 7 Future Work

Some of the areas where this work could be extended to better understand droplet behavior in PEMFC gas channels are as follows:

7.1 Capillary Grooves – Prevent Spreading of Liquid on the GDL

From the experimental results, it was found that corner filling is a serious issue with PEMFCs, especially when the droplets are introduced from the land or channel wall regions, and hence design modifications are warranted. Possible suggestions to address this issue include the incorporation of additional microchannel grooves on the sidewall that act as capillary channels to draw liquid from the land area and transport it to the top wall from where it would be removed by the airflow. The proposed design was validated and results were shown in Section 4.8.1. However, the width of the grooves used in that design was around 200 – 250 μm, which is quite large to provide good capillary rise action. Therefore, this work could be extended further to incorporate smaller width grooves on the sidewall to see how it helps in the removal of the water from the gas channel. A relation between the channel width and the capillary rise in the grooves in the presence of airflow could be investigated which would help the designer incorporate the optimum groove size in automotive fuel cell designs. Secondly, the grooves tested in this work were straight. The grooves could be made inclined on the sidewall such that they

are in the direction of the airflow. This will also aid in the removal of the liquid from the gas channel.

7.2 Compression of the GDL and its Effect on Droplet Dynamics

Compression of the GDL leads to larger intrusion of GDL in the channel, and affects the droplet dynamics in the gas channel. In this work, compression effects were not studied. Further work can be pursued to investigate the intrusion effect due to GDL compression. In addition, a study is recommended to investigate the plastic deformation near the corners due to compression and its effect on the droplet dynamics.

7.3 Study the Effect of the Different Droplet Dynamics Observed on Mass Transport Resistance inside the Gas Channel

The experimental work pursued in this dissertation, aimed only to understand droplet behavior in terms of its interaction with the sidewall and its removal. The effect of droplet dynamics on the mass transport resistance for oxygen transport to the reactant sites was not studied. A numerical study is suggested to determine the mass transport resistance in the gas channel under different airflow conditions.

7.4 Study the Effect of Temperature, Pressure and Humidity on Droplet Behavior

The study undertaken here was performed at room temperature under atmospheric pressure and no humidity conditions. However, a PEMFC works at temperature between 25° and 80°C, and at different humidity conditions. The droplet dynamics in the gas channel would change at different temperature and relative humidity (RH) conditions due to evaporation effects [173-177]. Therefore, the study could be extended to understand how droplet dynamics would be affected due to changes in temperature, pressure and RH.

7.5 Analysis of the Oscillations Produced in the Droplet Due to the Airflow

It was observed that near the transition angles, the oscillations introduced in the droplet by the airflow in the gas channel changed the IDCA the droplet made with the channel wall. This actually determines the corner filling and non–filling behavior. Therefore, a numerical study could be conducted to understand the streamlines of the airflow over the droplet or film under different airflow conditions. This study could be helpful in understanding how the airflow streamlines produce the oscillations in the droplet and change the IDCA the droplet makes with the channel walls.

Appendix I

1. Water Flow Rate Calculation

The channel dimensions used for these calculations were according to an active area of 50 cm^2 in a typical fuel cell that meets the Department of Energy specifications [133].

$$Length\ of\ channel\ (L_C) = 183\ mm$$

$$Channel\ width\ (C_w) = 0.7\ mm$$

$$Land\ Width\ (L_w) = 0.5\ mm$$

$$Active\ Area = (L_w + C_w) * L_C$$

$$Active\ Area = (0.5 + 0.7) * 183\ mm$$

$$Active\ Area\ (A) = 219.6\ mm^2 = 2.916\ cm^2$$

$$Current\ Density\ (i) = 0.3\ A/cm^2$$

$$Number\ of\ moles\ of\ water\ (n) = 2$$

$$Faraday\ constant = 96485$$

According to the Nernst Eq.

$$Water\ Generation\ (Q_g) = \frac{iA}{nF}\ mol/sec$$

$$Water\ Generation\ (Q_g) = \frac{(0.3 * 2.916\ )}{(2 * 96485)}\ \frac{mol}{sec} = 4.533 * 10^{-6}\ mol/sec$$

$$Water\ Generation\ (g/sec)\ =\ (Qg)\ *\ Molecular\ weight\ of\ Water\ (g/mol)$$

$$Water\ Generation\ (g/\ sec)\ =\ 4.533 * 10^{-6}\ mol/sec\ *\ 18.0153\ g/mol$$

$$=\ 8.167 * 10^{-5}\ g/sec$$

$$Mass\ flow\ rate\ (cm/sec) = \frac{Q_g}{\rho_{water}} *\ 10^6$$

$$Mass\ flow\ rate\ (cm/sec) = \frac{8.167\ *\ 10^{-5}}{996.95\ *\ 10^3} *\ 10^6 = 8.192 *\ 10^{-5}\ (cm/sec)$$

$$Mass\ flow\ rate\ (sccm) =\ Mass\ flow\ rate\ (cm/sec) * 60$$

$$Mass\ flow\ rate\ (sccm) =\ 8.192 *\ 10^{-5} * 60 =\ 0.005\ sccm$$

2. Superficial Airflow Rate Calculation

The channel dimensions used for these calculations were according to an active area of 50 cm^2 in a typical fuel cell that meets the Department of Energy specifications [51].

$$Active\ Area\ (A)\ =\ (\mathrm{L_w}\ +\ C_w)\ *\ \mathrm{L}_C *\ 22\ channel$$

$$Active\ Area\ (A) = 500\ mm^2 = 50\ cm^2$$

$$Current\ Density\ (i) = 1.5\ A/cm^2$$

$$Number\ of\ moles\ of\ air = 4$$

$$Faraday\ Constant\ (F) = 96485$$

$$Molecular\ Weight\ of\ Air\ (MW_{air}) = 28.96\ g/mole$$

$$Density\ of\ Air\ (\rho_{air})\ at\ 20℃ = 1.2041\ kg/m^3$$

$$Mass\ Flow\ rate\ of\ air = Stoich * \frac{MW_{air}}{\rho_{air}} \left(\frac{iA}{0.21nF}\right)$$

$$Air\ flow\ rate\ (\dot{Q}_{air}) = Stoich * \left(\frac{iA}{0.21nF}\right)\ mol/sec$$

$$Air\ flow\ rate\ (\dot{Q}_{air}) = \frac{2 * 1.5 * 50}{0.21 * 4 * 96485} mol/sec = 0.00185\ mol/sec$$

$$Air\ flow\ rate\ (\dot{Q}_{air})\ (g/sec) = (\dot{Q}_{air}) * Molecular\ Weight\ of\ Air\ (g/mol)$$

$$Air\ flow\ rate\ (\dot{Q}_{air})\ (g/sec) = 0.00185\ mol/sec * 28.96\ g/mol = 0.054\ g/sec$$

$$Mass\ flow\ rate\ (cm/sec) = \frac{\dot{Q}_{air}\ (g/sec)}{\rho_{air}\ (g/m^3)} * 10^6$$

$$Mass\ flow\ rate\ (cm/sec) = \frac{0.054}{1.2041 * 10^3} * 10^6 = 44.5\ (cm/sec)$$

$$Mass\ flow\ rate(sccm) = \ Mass\ flow\ rate\ (cm/sec) * 60$$

$$Mass\ flow\ rate(sccm) = \ 44.5 * 60 = 2670\ sccm$$

$$Mass\ flow\ rate\ per\ channel\ (sccm) \ = \ \frac{Mass\ flow\ rate(sccm)}{22}$$

$$Mass\ flow\ rate\ per\ channel\ (sccm) \ = \ 121.36\ sccm$$

$$Velocity\ of\ Air\ (V_{Air}) = \ \frac{Mass\ Flow\ Rate\ Per\ Channel * \ 10^{-6}}{60 * L_c * \ C_W * 10^{-6}}$$

$$V_{Air} = \ \frac{121.36 * \ 10^{-6}}{60 * 0.4 * 0.7 * 10^{-6}} = 7.23\ m/s$$

Appendix II

a. Geometrical Relationships

The following Eqs. are derived from the geometrical relationships as shown in Figure 5.2 and Figure 5.4.

$$\beta = \theta - \frac{\pi}{2} \quad [9.1]$$

$$\cos\beta = \cos\left(\theta - \frac{\pi}{2}\right) = \sin\theta \quad [9.2]$$

$$\delta = \frac{\pi}{2} - 2\alpha \quad [9.3]$$

$$\cos\delta = \cos\left(\frac{\pi}{2} - 2\alpha\right) = \sin 2\alpha \quad [9.4]$$

$$d = R_{C_1} \sin\delta \quad [9.5]$$

$$e = R_{C_1} \cos\delta \quad [9.6]$$

$$b = R_{C_1} \sin\beta \quad [9.7]$$

$$h = R_{C_1} - b = R_{C_1}(1 - \sin\beta) = R_{C_1}\left(1 - \sin\left(\theta - \frac{\pi}{2}\right)\right) \quad [9.8]$$

$$h = R_{C_1}(1 + \cos\theta) \quad [9.9]$$

$$\eta = \frac{\pi}{2} - 2\alpha \quad [9.10]$$

$$k = \frac{\pi}{2} - \phi \quad [9.11]$$

$$z = R_{C_2} \sin k = R_{C_2} \cos \phi \quad [9.12]$$

$$f = z \tan 2\alpha = R_{C_2} \cos \phi \tan 2\alpha \quad [9.13]$$

$$\sin \eta = \frac{z}{g} \quad [9.14]$$

$$g = \frac{z}{\sin \eta} = \frac{R_{C_2} \cos \phi}{\cos 2\alpha} \quad [9.15]$$

$$m = R_2 - z = R_2 - R_2 \cos \emptyset \quad [9.16]$$

i. To Find the Maximum Radius R_{C_1} Right Before it Jumps

The open angle 2α is related to the R_{C_1} and is given by Eq. 5.1

$$\tan 2\alpha = \frac{R_{C_1} \sin \beta + R_{C_1} \sin \delta}{a - R_{C_1} \cos \delta} \quad [5.1]$$

Rearranging Eq. 5.1, the maximum radius of the droplet just before it snaps and jumps to the sidewall is obtained.

$$R_{C_1} = \frac{a \tan 2\alpha}{\sin \beta + \sin \delta + \cos \delta \tan 2\alpha} \quad [9.17]$$

Substituting β and δ in terms of θ and 2α, the critical radius R_{C_1} can be obtained.

$$R_{C_1} = \frac{\mathrm{a} \tan 2\alpha}{\sin\left(\theta - \frac{\pi}{2}\right) + \sin\left(\frac{\pi}{2} - 2\alpha\right) + \cos\left(\frac{\pi}{2} - 2\alpha\right) \tan 2\alpha} \quad [9.18]$$

Solving Eq. 9.18, R_{C_1} is obtained as below

$$R_{C_1} = \frac{a \sin 2\alpha}{1-(\cos\theta \cos 2\alpha)} \quad [5.2]$$

ii. To Find the Distance of the Point of Contact of the Droplet on the Sidewall (*x*) from the Channel Corner Before it Jumps.

From Figure 5.3

$$x = [(b+d)^2 + (a-e)^2]^{1/2} \quad [9.19]$$

Substituting values of *b, d* and *e* in Eq. 5.23

$$x = \left[\left(R_{C_1} \sin\beta + R_{C_1} \sin\delta\right)^2 + \left(a - R_{C_1} \cos\delta\right)^2\right]^{1/2} \quad [9.20]$$

Substituting β and δ in terms of θ and 2α,

$$x = \left[{R_{C_1}}^2 \left(\cos 2\alpha - \cos\theta\right)^2 + \left(a - R_{C_1} \sin 2\alpha\right)^2\right]^{1/2} \quad [5.3]$$

iii. To Find the Volume (V_1) of the Droplet Sitting on the GDL

Volume of the droplet when it is sitting on the base surface right before it touches the sidewall as shown in Figure 5.2 is given as

Volume of the droplet for case 1 as shown in Figure 5.4 is given as

$$V_1 = V_{sphere} - V_{chord} \quad [9.21]$$

$$V_{sphere} = \frac{4\pi {R_{C_1}}^3}{3} \quad [9.22]$$

$$V_{chord} = \frac{\pi h^2 (3R_{C_1} - h)}{3} \quad [9.23]$$

Where *h* is the height of the spherical cap as shown in Figure 5.2

Substituting Eq. 9.22 and 9.23 in Eq. 9.21

$$V_1 = \frac{4\pi {R_{C_1}}^3}{3} - \frac{\pi h^2 (3R_{C_1} - h)}{3} \quad [9.24]$$

$$V_1 = \frac{4\pi {R_{C_1}}^3 - 3\pi R_{C_1} h^2 + \pi h^3}{3} \quad [9.25]$$

Substituting *h* in Eq. 9.25

$$V_1 = \frac{4\pi {R_{C_1}}^3 - 3\pi R_{C_1} \left(R_{C_1} + R_{C_1} \cos\theta\right)^2 + \pi \left(R_{C_1} + R_{C_1} \cos\theta\right)^3}{3} \quad [9.26]$$

$$V_1 = \frac{4\pi {R_{C_1}}^3 - 3\pi R_{C_1} \left({R_{C_1}}^2 + {R_{C_1}}^2 \cos^2\theta + 2\,{R_{C_1}}^2 \cos\theta\right) + \pi \left({R_{C_1}}^3 + {R_{C_1}}^3 \cos^3\theta + 3\,{R_{C_1}}^3 \cos\theta + 3\,{R_{C_1}}^3 \cos^2\theta\right)}{3} \quad [9.27]$$

Rearranging Eq. 9.27

$$V_1 = \frac{\pi \left(4{R_{C_1}}^3 - 3{R_{C_1}}^3 - 3{R_{C_1}}^3 \cos^2\theta - 6\,{R_{C_1}}^3 \cos\theta + {R_{C_1}}^3 + {R_{C_1}}^3 \cos^3\theta + 3\,{R_{C_1}}^3 \cos\theta + 3{R_{C_1}}^3 \cos^2\theta\right)}{3} \quad [9.28]$$

$$V_1 = \frac{\pi \left(2{R_{C_1}}^3 - 3\,{R_{C_1}}^3 cos\,\theta + {R_{C_1}}^3 cos\,\theta^3\right)}{3} \quad [5.4]$$

iv. To Find the Volume (V_2) of the Droplet Hanging from the Sidewall

Volume of the droplet when it jumps to the wall as shown in Figure 5.4 is given as

$$V_2 = \frac{\pi}{3} m^2 (3R_2 - m) \quad [9.28]$$

Substituting m in Eq. 9.28

$$V_2 = \frac{\pi}{3} (R_2 - R_2 \cos \emptyset)^2 \left(3R_2 - (R_2 - R_2 \cos \emptyset)\right) \quad [9.29]$$

$$V_2 = \frac{\pi}{3} \left({R_2}^2 + {R_2}^2 \cos^2 \emptyset - 2{R_2}^2 \cos \emptyset\right)(2R_2 + R_2 \cos \emptyset) \quad [9.30]$$

$$V_2 = \frac{\pi}{3} {R_2}^3 (1 + \cos^2 \emptyset - 2 \cos \emptyset)(2 + \cos \emptyset) \quad [9.31]$$

$$V_2 = \frac{\pi}{3} {R_2}^3 (2 + 2\cos^2 \emptyset - 4 \cos \emptyset + \cos \emptyset + \cos^3 \emptyset - 2 \cos^2 \emptyset) \quad [9.32]$$

$$V_2 = \frac{\pi}{3} {R_2}^3 (2 - 3 \cos \emptyset + \cos^3 \emptyset) \quad [5.5]$$

v. To Find the Maximum Radius R_{C2} While Hanging from the Sidewall Before Bridging

Figure 5.4 shows the triangle made by point A, B and C from which the relationship between the radius$^{R_{C_2}}$, midpoint x around which the droplet hangs and the open angle 2α is found.

$$\sin 2\alpha = \frac{R_{C_2} - g}{x - f} \quad [9.33]$$

Substituting Eq. 9.13 and 9.15 in Eq. 9.33

$$sin\,2\alpha = \frac{R_{C_2} - \left(\frac{R_{C_2}\,cos\,\phi}{cos\,2\alpha}\right)}{x - R_{C_2}\,cos\,\phi\,tan\,2\alpha} \qquad [5.7]$$

Eq. 5.7 is rearranged to get R_{C_2} in terms of open angle and sidewall contact angle

$$R_{C_2} = \frac{x\ sin\,2\alpha}{(1 - cos\,\phi\,cos\,2\alpha)} \qquad [9.34]$$

Substituting *x* in Eq. 9.34

$$R_{C_2} = \frac{\left[{R_{C_1}}^2\,(\,cos\,2\alpha - cos\,\theta\,)^2 + \left(a - R_{C_1}\,sin\,2\alpha\right)^2\right]^{1/2}\,sin\,2\alpha}{(1 - cos\,\phi\,cos\,2\alpha)} \qquad [5.8]$$

Therefore, Eq. 5.8 gives R_{C_2} in terms of the open angle, droplet emergence location, and base and sidewall contact angles.

b. Uncertainty Analysis

Theoretical Equations for Uncertainty Analysis
$$R_{C_1} = \frac{a\,sin\,2\alpha}{1 - (cos\,\theta\,cos\,2\alpha)}$$
$$\frac{R_2}{R_{C_2}} = \frac{R_{C_1}\left[\frac{2 - 3\cos\theta + \cos^3\theta}{2 - 3\cos\emptyset + \cos^3\emptyset}\right]^{1/3}(1 - cos\,\phi\,cos\,2\alpha)}{\left[{R_{C_1}}^2\,(\,cos\,2\alpha - cos\,\theta\,)^2 + \left(a - \left(R_{C_1} * \sin 2\alpha\right)\right)^2\right]^{1/2}\,sin\,2\alpha}$$

$$v = \sqrt{\frac{4\,\sigma \sin\theta\,(\cos\theta_A - \cos\theta_R)}{K\,C_D\,\rho\left(\frac{a\sin 2\alpha}{1-(\cos\theta\cos 2\alpha)}\right)\left(\theta - \frac{\sin 2\theta}{2}\right)}}$$

$$K = (0.65\sin 2\alpha - 0.87)v + \ (-6.3\sin 2\alpha + 8.4)\ - MRC - 105$$

$$K = (0.4\sin 2\alpha - 0.66)v + \ (-3.88\sin 2\alpha + 6.47)\ - TGP - H - 060$$

$$K = (0.88\sin 2\alpha - 1.5)v + \ (-8.3\sin 2\alpha + 14.3)\ - SGL - 25BC$$

$$C_D = \frac{24}{Re}\,(1 + 0.1925\,Re^{0.63})$$

Uncertainty Analysis

$$R_{C_1} = \frac{a\,sin\,2\alpha}{1-(cos\,\theta\,cos\,2\alpha)}$$

Let $B = 1 - (cos\,\theta\,cos\,2\alpha)$

$$R_{C_1} = \frac{a\,sin\,2\alpha}{B}$$

$$\frac{U_{R_{C_1}}}{R_{C_1}} = \left[\left(\frac{U_a}{a}\right)^2 + \left(\frac{U_{\sin 2\alpha}}{\sin 2\alpha}\right)^2 + \left(\frac{U_B}{B}\right)^2\right]^{1/2}$$

$$\left[\frac{U_B}{B}\right]^2 = \left(\frac{U_1}{1-(cos\,\theta\,cos\,2\alpha)}\right)^2 + \left(\frac{U_{\cos\theta}}{1-(cos\,\theta\,cos\,2\alpha)}\right)^2 + \left(\frac{U_{\cos 2\alpha}}{1-(cos\,\theta\,cos\,2\alpha)}\right)^2$$

$$U_{Constant} = 0$$

$$\left[\frac{U_B}{B}\right]^2 = \left(\frac{U_{\cos\theta}}{1-(\cos\theta\cos 2\alpha)}\right)^2 + \left(\frac{U_{\cos 2\alpha}}{1-(\cos\theta\cos 2\alpha)}\right)^2$$

$$\frac{U_{R_{C_1}}}{R_{C_1}} = \left[\left(\frac{U_a}{a}\right)^2 + \left(\frac{U_{\sin 2\alpha}}{\sin 2\alpha}\right)^2 + \left(\frac{U_{\cos\theta}}{1-(\cos\theta\cos 2\alpha)}\right)^2 + \left(\frac{U_{\cos 2\alpha}}{1-(\cos\theta\cos 2\alpha)}\right)^2\right]^{1/2}$$

$$\frac{R_2}{R_{C_2}} = \frac{R_{C_1}\left[\frac{2-3\cos\theta+\cos^3\theta}{2-3\cos\emptyset+\cos^3\emptyset}\right]^{1/3}(1-\cos\phi\cos 2\alpha)}{\left[{R_{C_1}}^2(\cos 2\alpha-\cos\theta)^2+\left(a-\left(R_{C_1}*\sin 2\alpha\right)\right)^2\right]^{1/2}\sin 2\alpha}$$

$$\frac{U_{\frac{R_2}{R_{C_2}}}}{\frac{R_2}{R_{C_2}}} = \left[\left(\frac{U_{R_{C_1}}}{R_{C_1}}\right)^2 + \left(\frac{U\left[\frac{2-3\cos\theta+\cos^3\theta}{2-3\cos\emptyset+\cos^3\emptyset}\right]^{1/3}}{\left[\frac{2-3\cos\theta+\cos^3\theta}{2-3\cos\emptyset+\cos^3\emptyset}\right]^{1/3}}\right)^2 + \left(\frac{U_{(1-\cos\phi\cos 2\alpha)}}{1-\cos\phi\cos 2\alpha}\right)^2 + \left(\frac{U\left(\left[{R_{C_1}}^2(\cos 2\alpha-\cos\theta)^2+\left(a-\left(R_{C_1}*\sin 2\alpha\right)\right)^2\right]^{1/2}\right)}{\left[{R_{C_1}}^2(\cos 2\alpha-\cos\theta)^2+\left(a-\left(R_{C_1}*\sin 2\alpha\right)\right)^2\right]^{1/2}}\right)^2 + \left(\frac{U_{sin\,2\alpha}}{sin\,2\alpha}\right)^2\right]^{1/2}$$

$$\frac{U_{R_{C_1}}}{R_{C_1}} = \left[\left(\frac{U_a}{a}\right)^2 + \left(\frac{U_{\sin 2\alpha}}{\sin 2\alpha}\right)^2 + \left(\frac{U_{\cos\theta}}{1-(\cos\theta\cos 2\alpha)}\right)^2 + \left(\frac{U_{\cos 2\alpha}}{1-(\cos\theta\cos 2\alpha)}\right)^2\right]^{1/2}$$

Let $C = 2 - 3\cos\theta + \cos^3\theta$

Let $D = 2 - 3\cos\emptyset + \cos^3\emptyset$

$$\frac{U_{\left[\frac{C}{D}\right]^{1/3}}}{\left[\frac{C}{D}\right]} = \left[1/3\left\{\left(\frac{U_C}{C}\right)^2 + \left(\frac{U_D}{D}\right)^2\right\}\right]^{1/2}$$

$$\frac{U_C}{C} = \left[\left(\frac{U_{cos\,\theta}}{2-3\cos\theta+\cos^3\theta}\right)^2 + 3\left(\frac{U_{cos\,\theta}}{2-3\cos\theta+\cos^3\theta}\right)^2\right]^{1/2} = 2\left(\frac{U_{cos\,\theta}}{2-3\cos\theta+\cos^3\theta}\right)$$

$$\frac{U_D}{D} = \left[\left(\frac{U_{cos\,\emptyset}}{2-3\cos\emptyset+\cos^3\emptyset}\right)^2 + 3\left(\frac{U_{cos\,\emptyset}}{2-3\cos\emptyset+\cos^3\emptyset}\right)^2\right]^{1/2} = 2\left(\frac{U_{cos\,\emptyset}}{2-3\cos\emptyset+\cos^3\emptyset}\right)$$

$$\frac{U_{\left[\frac{2-3\cos\theta+\cos^3\theta}{2-3\cos\emptyset+\cos^3\emptyset}\right]^{1/3}}}{\left[\frac{2-3\cos\theta+\cos^3\theta}{2-3\cos\emptyset+\cos^3\emptyset}\right]^{1/3}} = \left[1/3\left\{\left(2\left(\frac{U_{cos\,\theta}}{2-3\cos\theta+\cos^3\theta}\right)\right)^2 + \left(2\left(\frac{U_{cos\,\emptyset}}{2-3\cos\emptyset+\cos^3\emptyset}\right)\right)^2\right\}\right]^{1/2}$$

$$\frac{U_{(1-cos\,\phi\,cos\,\phi)}}{1-cos\,\phi\,cos\,2\alpha} = \left[\left(\frac{U_{cos\,\phi}}{1-cos\,\phi\,cos\,2\alpha}\right)^2 + \left(\frac{U_{cos\,\phi}}{1-cos\,\phi\,cos\,2\alpha}\right)^2\right]^{1/2}$$

Let $E = (\,cos\,2\alpha - \,cos\,\theta\,)^2$

Let $F = \left(a - \left(R_{C_1} * \sin 2\alpha\right)\right)^2$

Let $G = {R_{C_1}}^2$

$$\frac{U_{(GE+F)^{1/2}}}{(GE+F)^{1/2}} = \left[1/2\left\{\left(\frac{U_{GE}}{GE+F}\right)^2 + \left(\frac{U_F}{GE+F}\right)^2\right\}\right]^{1/2}$$

$${U_{GE}}^2 = (GE)^2\left[\left(\frac{U_G}{G}\right)^2 + \left(\frac{U_E}{E}\right)^2\right]$$

$$\left(\frac{U_E}{E}\right)^2 = \left[2\left\{\left(\frac{U_{\cos 2\alpha}}{\cos 2\alpha - \cos\theta}\right)^2 + \left(\frac{U_{\cos\theta}}{\cos 2\alpha - \cos\theta}\right)^2\right\}\right]$$

$$\left(\frac{U_F}{F}\right)^2 = 2\left\{\left(\frac{U_a}{a-\left(R_{C_1}*\sin 2\alpha\right)}\right)^2 + \left(\frac{\left(R_{C_1}*\sin 2\alpha\right)^2\left[\left(\frac{U_{R_{C_1}}}{R_{C_1}}\right)^2 + \left(\frac{U_{\sin 2\alpha}}{\sin 2\alpha}\right)^2\right]}{a-\left(R_{C_1}*\sin 2\alpha\right)}\right)^2\right\}$$

$$\frac{U_{(GE+F)^{1/2}}}{(GE+F)^{1/2}} = \left[1/2\left\{\frac{(GE)^2\left[\left(\frac{U_G}{G}\right)^2+\left(\frac{U_E}{E}\right)^2\right]}{(GE+F)^2} + \left(\frac{U_F}{GE+F}\right)^2\right\}\right]^{1/2}$$

$$\frac{U\left(\left[R_{C_1}{}^2\left(\cos 2\alpha-\cos\theta\right)^2+\left(a-\left(R_{C_1}*\sin 2\alpha\right)\right)^2\right]^{1/2}\right)}{\left[R_{C_1}{}^2\left(\cos 2\alpha-\cos\theta\right)^2+\left(a-\left(R_{C_1}*\sin 2\alpha\right)\right)^2\right]^{1/2}} = \left[1/\right.$$

$$2\left\{\frac{\left(R_{C_1}{}^2\left(\cos 2\alpha-\cos\theta\right)^2\right)^2\left[\begin{array}{c}\left(\frac{U_a}{a}\right)^2+\left(\frac{U_{\sin 2\alpha}}{\sin 2\alpha}\right)^2+\left(\frac{U_{\cos\theta}}{1-(\cos\theta\cos 2\alpha)}\right)^2+\left(\frac{U_{\cos 2\alpha}}{1-(\cos\theta\cos 2\alpha)}\right)^2\\ +2\left\{\left(\frac{U_{\cos 2\alpha}}{\cos 2\alpha-\cos\theta}\right)^2+\left(\frac{U_{\cos\theta}}{\cos 2\alpha-\cos\theta}\right)^2\right\}\end{array}\right]}{\left[R_{C_1}{}^2\left(\cos 2\alpha-\cos\theta\right)^2+\left(a-\left(R_{C_1}*\sin 2\alpha\right)\right)^2\right]}+\right.$$

$$\frac{(a-(R_{C_1}*\sin 2\alpha))^4\left(2\left\{\left(\frac{U_a}{a-(R_{C_1}*\sin 2\alpha)}\right)^2+\left(\frac{(R_{C_1}*\sin 2\alpha)^2\left[\left(\frac{U_{R_{C_1}}}{R_{C_1}}\right)^2+\left(\frac{U_{\sin 2\alpha}}{\sin 2\alpha}\right)^2\right]}{a-(R_{C_1}*\sin 2\alpha)}\right)^2\right\}\right)}{\left[R_{C_1}{}^2\,(\cos 2\alpha-\cos\theta)^2+(a-(R_{C_1}*\sin 2\alpha))^2\right]}\Bigg\}^{1/2}$$

$$v=\sqrt{\frac{4\,\sigma\sin\theta\,(\cos\theta_A-\cos\theta_R)}{K\,C_D\,\rho\left(\frac{a\sin 2\alpha}{1-(\cos\theta\cos 2\alpha)}\right)\left(\theta-\frac{\sin 2\theta}{2}\right)}}$$

$$v=\sqrt{\frac{4\,\sigma\sin\theta\,(\cos\theta_A-\cos\theta_R)}{K\,C_D\,\rho R_{C_1}\left(\theta-\frac{\sin 2\theta}{2}\right)}}$$

$$C_D=\left(\frac{24}{Re}\,(1+0.1925\,Re^{0.63})\right)=\,24\,Re^{-1}+4.62Re^{-0.37}$$

Let $H=\left(\theta-\frac{\sin 2\theta}{2}\right)$

Let $J=\,(\cos\theta_A-\cos\theta_R)$

$$\frac{U_v}{v}=\,1/2\left[\left(\frac{U_\sigma}{\sigma}\right)^2+\left(\frac{U_{\sin\theta}}{\sin\theta}\right)^2+\left(\frac{U_J}{J}\right)^2+\left(\frac{U_K}{K}\right)^2+\,\left(\frac{U_{C_D}}{C_D}\right)^2+\left(\frac{U_{R_{C_1}}}{R_{C_1}}\right)^2+\left(\frac{U_\rho}{\rho}\right)^2+\left(\frac{U_H}{H}\right)^2\right]^{1/2}$$

$$\left(\frac{U_J}{J}\right)^2=\,\left(\frac{U_{\cos\theta_A}}{\cos\theta_A-\cos\theta_R}\right)^2+\left(\frac{U_{\cos\theta_A}}{\cos\theta_A-\cos\theta_R}\right)^2$$

$$\left(\frac{U_{C_D}}{C_D}\right)^2 = -\left(\frac{U_{Re}}{Re}\right)^2 - 0.37\left(\frac{U_{Re}}{Re}\right)^2 = -1.37\left(\frac{U_{Re}}{Re}\right)^2$$

$$\left(\frac{U_{R_{C_1}}}{R_{C_1}}\right)^2 = \left(\frac{U_a}{a}\right)^2 + \left(\frac{U_{\sin 2\alpha}}{\sin 2\alpha}\right)^2 + \left(\frac{U_{\cos\theta}}{1-(\cos\theta\cos 2\alpha)}\right)^2 + \left(\frac{U_{\cos 2\alpha}}{1-(\cos\theta\cos 2\alpha)}\right)^2$$

$$\left(\frac{U_H}{H}\right)^2 = \left(\frac{U_\theta}{\theta-\frac{\sin 2\theta}{2}}\right)^2 + \left(\frac{U_{\frac{\sin 2\theta}{2}}}{\theta-\frac{\sin 2\theta}{2}}\right)^2$$

$$\left(\frac{U_K}{K}\right)^2 = \frac{(0.65\,v*\sin 2\alpha)^2\left[\left(\frac{U_{\sin 2\alpha}}{\sin 2\alpha}\right)^2+\left(\frac{U_v}{v}\right)^2\right]}{\left((0.65\sin 2\alpha-0.87)v+(-6.3\sin 2\alpha+8.4)\right)^2} + \left(\frac{U_v}{(0.65\sin 2\alpha-0.87)v+(-6.3\sin 2\alpha+8.4)}\right)^2 +$$

$$\left(\frac{U_{\sin 2\alpha}}{(0.65\sin 2\alpha-0.87)v+(-6.3\sin 2\alpha+8.4)}\right)^2 - MRC-105$$

$$\left(\frac{U_K}{K}\right)^2 = \frac{(0.4\,v*\sin 2\alpha)^2\left[\left(\frac{U_{\sin 2\alpha}}{\sin 2\alpha}\right)^2+\left(\frac{U_v}{v}\right)^2\right]}{\left((0.4\sin 2\alpha-0.66)v+(-3.88\sin 2\alpha+6.47)\right)^2} + \left(\frac{U_v}{[(0.4\sin 2\alpha-0.66)v+(-3.88\sin 2\alpha+6.47)]}\right)^2 +$$

$$\left(\frac{U_{\sin 2\alpha}}{[(0.4\sin 2\alpha-0.66)v+(-3.88\sin 2\alpha+6.47)]}\right)^2 - TGP-H-060$$

$$\left(\frac{U_K}{K}\right)^2 = \frac{(0.88\,v*\sin 2\alpha)^2\left[\left(\frac{U_{\sin 2\alpha}}{\sin 2\alpha}\right)^2+\left(\frac{U_v}{v}\right)^2\right]}{\left((0.88\sin 2\alpha-1.5)v+(-8.3\sin 2\alpha+14.3)\right)^2} + \left(\frac{U_v}{[(0.88\sin 2\alpha-1.5)v+(-8.3\sin 2\alpha+14.3)]}\right)^2 +$$

$$\left(\frac{U_{\sin 2\alpha}}{[(0.88\sin 2\alpha-1.5)v+(-8.3\sin 2\alpha+14.3)]}\right)^2 - SGL-25BC$$

References

[1] Dresselhaus, M. S., and Thomas, I. L., 2001, "Alternative Energy Technologies," Nature, 414(6861), pp. 332-337.

[2] OECD, 1996, "Towards Sustainable Transportation," OECD- hosted by the Government of CanadaVancouver, British Columbia.

[3] OECD, 2010, "Reducing Transport Greenhouse Gas Emissions - Trends & Data," International Transport ForumLeipzig, Germany.

[4] UW Courses, 2007, "Improving IC Engine Efficiency," http://courses.washington.edu/me341/oct22v2.htm.

[5] Baglione, M., Duty, M., and Pannone, G., 2007, "Vehicle System Energy Analysis Methodology and Tool for Determining Vehicle Subsystem Energy Supply and Demand," SAE World Congress & ExhibitionDetroit, MI, USA.

[6] Kavya, 2012, "Car Pollution - LabSaints," http://labsaints.com/ecology-adopts-changes-to-air-quality-fees-clean-cars-standards-general-regulation-of-sources/car-pollution-2/.

[7] Hoffmann, P., 2002, Tomorrow's Energy: Hydrogen, Fuel Cells and the Prospects for a Cleaner Planet, The MIT Press, Cambridge, MA.

[8] Wen, Z., Liu, J., and Li, J., 2008, "Core/Shell Pt/C Nanoparticles Embedded in Mesoporous Carbon as a Methanol-Tolerant Cathode Catalyst in Direct Methanol Fuel Cells," Advanced Materials, 20(4), pp. 743-747.

[9] Srinivasan, S., 2006, "Fuel Cells: From Fundamentals to Applications," Springer, New York.

[10] World Energy Council, August 4, 2011, "Fuel Cell Efficiency," http://www.worldenergy.org/focus/fuel_cells/377.asp.

[11] Eberle, D. U., and von Helmolt, D. R., 2010, "Sustainable Transportation Based on Electric Vehicle Concepts: a Brief Overview," Energy & Environmental Science, 3(6), pp. 689-699.

[12] Steinbrenner, J. E., Lee, E. S., Hidrovo, C. H., Eaton, J. K., and Goodson, K. E., 2011, "Impact of Channel Geometry on Two-Phase Flow in Fuel Cell Microchannels," Journal of Power Sources, 196(11), pp. 5012-5020.

[13] Owejan, J. P., Gagliardo, J. J., Sergi, J. M., Kandlikar, S. G., and Trabold, T. A., 2009 "Water Management Studies in PEM Fuel Cells, Part I: Fuel Cell Design and *In Situ* Water Distributions," International Journal of Hydrogen Energy, 34 (8), pp. 3436–3444.

[14] Saha, M. S., Li, R., and Sun, X., 2007, "Composite of Pt-Ru Supported SnO_2 Nanowires Grown on Carbon Paper for Electrocatalytic Oxidation of Methanol," Electrochemistry Communications, 9(9), pp. 2229-2234.

[15] Mathias, M., Roth, J., Fleming, J., and Lehnert, W., 2003, "Diffusion Media Materials and Characterisation," Handbook of Fuel Cells: Fundamentals, Technology, and Applications, W. Vielstich, A. Lamm, and H. Gasteiger, eds., Wiley, Hoboken, N.J.

[16] Middelman, E., Kout, W., Vogelaar, B., Lenssen, J., and de Waal, E., 2003, "Bipolar Plates for PEM Fuel Cells," Journal of Power Sources, 118(1), pp. 44-46.

[17] Mench, M. M., 2008, "Basic Electrochemical Principles," Fuel Cell Engines, John Wiley & Sons, Inc., pp. 29-61.

[18] Jiang, Z., and Jiang, Z.-J., 2011, "Carbon Nanotubes Supported Metal Nanoparticles for the Applications in Proton Exchange Membrane Fuel Cells (PEMFCs)," Carbon Nanotubes - Growth and Applications, D. M. Naraghi, ed., InTech.

[19] Wang, L., and Liu, H., 2004, "Performance Studies of PEM Fuel Cells with Interdigitated Flow Fields," Journal of Power Sources, 134(2), pp. 185-196.

[20] Kowal, J. J., Turhan, A., Heller, K., Brenizer, J., and Mench, M. M., 2006, "Liquid Water Storage, Distribution, and Removal from Diffusion Media in PEFCS," Journal of Electrochemical Society, 153(10), pp. A1971-A1978.

[21] Li, H., Tang, Y., Wang, Z., Shi, Z., Wu, S., Song, D., Zhang, J., Fatih, K., Zhang, J., Wang, H., Liu, Z., Abouatallah, R., and Mazza, A., 2008, "A Review of Water Flooding Issues in the Proton Exchange Membrane Fuel Cell," Journal of Power Sources, 178, pp. 103–117.

[22] Barbir, F., Gorgun, H., and Wang, X., 2005, "Relationship Between Pressure Drop and Cell Resistance as a Diagnostic Tool for PEM Fuel Cells," Journal of Power Sources, 141, pp. 96–101.

[23] Nguyen, T. V., and Knobbe, M. W., 2003, "A Liquid Water Management Strategy for PEM Fuel Cell Stacks," Journal of Power Sources, 114 pp. 70-79.

[24] Owejan, J. P., Trabold, T. A., Gagliardo, J. J., Jacobson, D. L., Carter, R. N., Hussey, D. S., and Arif, M., 2007, "Voltage Instability in a Simulated Fuel Cell Stack Correlated to Cathode Water Accumulation," Journal of Power Sources, 171, pp. 626-633.

[25] He, W., Lin, G., and Van Nguyen, T., 2003, "Diagnostic Tool to Detect Electrode Flooding in Proton Exchange Membrane Fuel Cells," AIChE Journal, 49, pp. 3221-3228.

[26] Cha, S. W., O‟Hayre, R., Lee, S. J., Saito, Y., and Prinz, F. B., 2004, "Geometric Scale Effect of Flow Channels on Performance of Fuel Cells," Jounal of The Electrochemical Society, pp. A1856-A1864.

[27] Whyman, G., Bormashenko, E., and Stein, T., 2008, "The Rigorous Derivation of Young, Cassie-Baxter and Wenzel Equations and the Analysis of the Contact Angle Hysteresis Phenomenon," Chemical Physics Letters, 450(4-6), pp. 355-359.

[28] Carey, V. P., 1992, "Liquid-Vapor Phase-Change Phenomena," Taylor and Francis, Bristol, PA.

[29] Fang, C., Hidrovo, C., Wang, F. M., Eaton, J., and Goodson, K., 2008, "3-D Numerical Simulation of Contact Angle Hysteresis for Microscale Two Phase Flow," International Journal of Multiphase Flow, 34(7), pp. 690-705.

[30] Wenzel, R. N., 1949, "Surface Roughness and Contact Angle," The Journal of Physical and Colloid Chemistry, 53(9), pp. 1466-1467.

[31] Quéré, D., Di Meglio, J.-M., and Brochard-Wyart, F., 1988, "Wetting of Fibers : Theory and Experiments," Revue de Physique Appliquée, 23(6), pp. 1023-1030.

[32] Bhushan, B., Nosonovsky, M., and Chae Jung, Y., 2007, "Towards Optimization of Patterned Superhydrophobic Surfaces," Journal of The Royal Society Interface, 4, pp. 643-648.

[33] Quéré, D., 2008, "Wetting and Roughness," Annual Review of Materials Research, 38(1), pp. 71-99.

[34] Cassie, A. B. D., 1948, "Contact Angles," Discussions of the Faraday Society, 3, pp. 11-16.

[35] Wray, P., 2011, "Ceramic Tech Today (AcerS Ceramic Materials, Applications and Business Blog)," http://ceramics.org/ceramictechtoday/2011/01/20/extreme-caution-suggested-superhydrophobic-surfaces-may-have-weak-icephobic-properties/.

[36] Drelich, J., and Miller, J. D., 1994, "The Effect of Solid Surface Heterogeneity and Roughness on the Contact Angle/Drop (Bubble) Size Relationship," Journal of Colloid and Interface Science, 164(1), pp. 252-259.

[37] Kwon, Y., Patankar, N., Choi, J., and Lee, J., 2009, "Design of Surface Hierarchy for Extreme Hydrophobicity," Langmuir, 25(11), pp. 6129-6136.

[38] Shirtcliffe, N. J., McHale, G., Newton, M. I., Chabrol, G., and Perry, C. C., 2004, "Dual-Scale Roughness Produces Unusually Water-Repellent Surfaces," Advanced Materials, 16(21), pp. 1929-1932.

[39] Patankar, N. A., 2004, "Mimicking the Lotus Effect: Influence of Double Roughness Structures and Slender Pillars," Langmuir, 20(19), pp. 8209-8213.

[40] Gao, X., Yan, X., Yao, X., Xu, L., Zhang, K., Zhang, J., Yang, B., and Jiang, L., 2007, "The Dry-Style Antifogging Properties of Mosquito Compound Eyes and Artificial Analogues Prepared by Soft Lithography," Advanced Materials, 19(17), pp. 2213-2217.

[41] Gao, L., and McCarthy, T. J., 2007, "How Wenzel and Cassie Were Wrong," Langmuir, 23(7), pp. 3762-3765.

[42] Gao, and McCarthy, T. J., 2007, "Reply to “Comment on How Wenzel and Cassie Were Wrong by Gao and McCarthy”," Langmuir, 23(26), pp. 13243-13243.

[43] Chang-Hwan, C., and Chang-Jin, K., 2006, "Fabrication of a Dense Array of Tall Nanostructures over a Large Sample Area with Sidewall Profile and Tip Sharpness Control," Nanotechnology, 17(21), p. 5326.

[44] Dorrer, C., and Rühe, J., 2008, "Wetting of Silicon Nanograss: From Superhydrophilic to Superhydrophobic Surfaces," Advanced Materials, 20(1), pp. 159-163.

[45] Autumn, K., and Hansen, W., 2006, "Ultrahydrophobicity Indicates a Non-Adhesive Default State in Gecko Setae," Journal of Comparative Physiology A: Neuroethology, Sensory, Neural, and Behavioral Physiology, 192(11), pp. 1205-1212.

[46] Gao, L., and McCarthy, T. J., 2006, "Contact Angle Hysteresis Explained," Langmuir, 22(14), pp. 6234-6237.

[47] Extrand, C. W., 2003, "Contact Angles and Hysteresis on Surfaces with Chemically Heterogeneous Islands," Langmuir, 19(9), pp. 3793-3796.

[48] Extrand, C. W., and Kumagai, Y., 1997, "An Experimental Study of Contact Angle Hysteresis," Journal of Colloid and Interface Science, 191(2), pp. 378-383.

[49] Bartell, F. E., and Shepard, J. W., 1953, "Surface Roughness as Related to Hysteresis of Contact Angles. II. The Systems Paraffin–3 Molar Calcium Chloride Solution–Air and Paraffin–Glycerol–Air," The Journal of Physical Chemistry, 57(4), pp. 455-458.

[50] Nosonovsky, M., 2007, "Multiscale Roughness and Stability of Superhydrophobic Biomimetic Interfaces," Langmuir, 23(6), pp. 3157-3161.

[51] Drelich, J., and Miller, J. D., 1993, "Modification of the Cassie Equation," Langmuir, 9(2), pp. 619-621.

[52] Milne, A. J. B., Elliott, J. A. W., Zabeti, P., Zhou, J., and Amirfazli, A., 2011, "Model and Experimental Studies for Contact Angles of Surfactant Solutions on Rough and Smooth Hydrophobic Surfaces," Physical Chemistry Chemical Physics, 13(36), pp. 16208-16219.

[53] Choi, W., Tuteja, A., Mabry, J. M., Cohen, R. E., and McKinley, G. H., 2009, "A Modified Cassie–Baxter Relationship to Explain Contact Angle Hysteresis and Anisotropy on Non-Wetting Textured Surfaces," Journal of Colloid and Interface Science, 339(1), pp. 208-216.

[54] Cheng, Y.-T., and Rodak, D. E., 2005, "Is the Lotus Leaf Superhydrophobic?," Applied Physics Letters, 86(14), pp. 144101-144103.

[55] Bico, J., Thiele, U., and Quéré, D., 2002, "Wetting of Textured Surfaces," Colloids and Surfaces A: Physicochemical and Engineering Aspects, 206(1–3), pp. 41-46.

[56] Nosonovsky, M., 2007, "On the Range of Applicability of the Wenzel and Cassie Equations," Langmuir, 23(19), pp. 9919-9920.

[57] Li, W., and Amirfazli, A., 2007, "Microtextured Superhydrophobic Surfaces: A Thermodynamic Analysis," Advances in Colloid and Interface Science, 132(2), pp. 51-68.

[58] Marmur, A., 2006, "Soft Contact: Measurement and Interpretation of Contact Angles," Soft Matter, 2(1), pp. 12-17.

[59] Yoshimitsu, Z., Nakajima, A., Watanabe, T., and Hashimoto, K., 2002, "Effects of Surface Structure on the Hydrophobicity and Sliding Behavior of Water Droplets," Langmuir, 18(15), pp. 5818-5822.

[60] McHale, G., Aqil, S., Shirtcliffe, N. J., Newton, M. I., and Erbil, H. Y., 2005, "Analysis of Droplet Evaporation on a Superhydrophobic Surface," Langmuir, 21(24), pp. 11053-11060.

[61] Shirtcliffe, N. J., McHale, G., Newton, M. I., and Perry, C. C., 2005, "Wetting and Wetting Transitions on Copper-Based Super-Hydrophobic Surfaces," Langmuir, 21(3), pp. 937-943.

[62] Thiele, U., Brusch, L., Bestehorn, M., and Bär, M., 2003, "Modelling Thin-Film Dewetting on Structured Substrates and Templates: Bifurcation Analysis and Numerical Simulations," The European Physical Journal E: Soft Matter and Biological Physics, 11(3), pp. 255-271.

[63] Herminghaus, S., 2000, "Roughness-Induced Non-Wetting," Europhysics Letter, 52(2), pp. 165-170.

[64] Shibuichi, S., Onda, T., Satoh, N., and Tsujii, K., 1996, "Super Water-Repellent Surfaces Resulting from Fractal Structure," The Journal of Physical Chemistry, 100(50), pp. 19512-19517.

[65] He, B., Lee, J., and Patankar, N. A., 2004, "Contact Angle Hysteresis on Rough Hydrophobic Surfaces," Colloids and Surfaces A: Physicochemical and Engineering Aspects, 248(1–3), pp. 101-104.

[66] Barthlott, W., and Neinhuis, C., 1997, "Purity of the Sacred Lotus, or Escape from Contamination in Biological Surfaces," Planta, 202(1), pp. 1-8.

[67] Patankar, N. A., 2004, "Transition Between Superhydrophobic States on Rough Surfaces," Langmuir, 20(17), pp. 7097-7102.

[68] Liu, B., and Lange, F. F., 2006, "Pressure Induced Transition Between Superhydrophobic States: Configuration Diagrams and Effect of Surface Feature Size," Journal of Colloid and Interface Science, 298(2), pp. 899-909.

[69] Jeong, H. E., Lee, S. H., Kim, J. K., and Suh, K. Y., 2006, "Nanoengineered Multiscale Hierarchical Structures with Tailored Wetting Properties," Langmuir, 22(4), pp. 1640-1645.

[70] Bormashenko, E., Bormashenko, Y., Stein, T., Whyman, G., Pogreb, R., and Barkay, Z., 2007, "Environmental Scanning Electron Microscopy Study of the Fine Structure of the Triple Line and Cassie−Wenzel Wetting Transition for Sessile Drops Deposited on Rough Polymer Substrates," Langmuir, 23(8), pp. 4378-4382.

[71] Bormashenko, E., Pogreb, R., Whyman, G., Bormashenko, Y., and Erlich, M., 2007, "Vibration-Induced Cassie-Wenzel Wetting Transition on Rough Surfaces," Applied Physics Letters, 90(20), pp. 201917-201912.

[72] Bormashenko, E., Stein, T., Whyman, G., Bormashenko, Y., and Pogreb, R., 2006, "Wetting Properties of the Multiscaled Nanostructured Polymer and Metallic Superhydrophobic Surfaces," Langmuir, 22(24), pp. 9982-9985.

[73] Nosonovsky, M., 2007, "Model for Solid-Liquid and Solid-Solid Friction of Rough Surfaces with Adhesion Hysteresis," The Journal of Chemical Physics, 126(22), pp. 224701-224706.

[74] Ishino, C., and Okumura, K., 2008, "Wetting Transitions on Textured Hydrophilic Surfaces," The European Physical Journal E: Soft Matter and Biological Physics, 25(4), pp. 415-424.

[75] Lafuma, A., and Quere, D., 2003, "Superhydrophobic States," Nature Mater, 2(7), pp. 457-460.

[76] Koishi, T., Yasuoka, K., Fujikawa, S., Ebisuzaki, T., and Zeng, X. C., 2009, "Coexistence and Transition Between Cassie and Wenzel State on Pillared Hydrophobic Surface," Proceedings of the National Academy of Sciences, pp. 8435-8440.

[77] He, B., Patankar, N. A., and Lee, J., 2003, "Multiple Equilibrium Droplet Shapes and Design Criterion for Rough Hydrophobic Surfaces," Langmuir, 19(12), pp. 4999-5003.

[78] Jung, Y. C., and Bhushan, B., 2008, "Dynamic Effects of Bouncing Water Droplets on Superhydrophobic Surfaces," Langmuir, 24(12), pp. 6262-6269.

[79] Forsberg, P., Nikolajeff, F., and Karlsson, M., 2011, "Cassie-Wenzel and Wenzel-Cassie Transitions on Immersed Superhydrophobic Surfaces Under Hydrostatic Pressure," Soft Matter, 7(1), pp. 104-109.

[80] Bahadur, V., and Garimella, S. V., 2009, "Preventing the Cassie−Wenzel Transition Using Surfaces with Noncommunicating Roughness Elements," Langmuir, 25(8), pp. 4815-4820.

[81] Daniel, S., Chaudhury, M. K., and de Gennes, P. G., 2005, "Vibration-Actuated Drop Motion on Surfaces for Batch Microfluidic Processes," Langmuir, 21(9), pp. 4240-4248.

[82] Celestini, F., and Kofman, R., 2006, "Vibration of Submillimeter Size Supported Droplets," Physical Review E, 73(4), p. 041602.

[83] Noblin, X., Buguin, A., and Brochard-Wyart, F., 2004, "Vibrated Sessile Drops: Transition Between Pinned and Mobile Contact Line Oscillations," The European Physical Journal E: Soft Matter and Biological Physics, 14(4), pp. 395-404.

[84] Meiron, T. S., Marmur, A., and Saguy, I. S., 2004, "Contact Angle Measurement on Rough Surfaces," Journal of Colloid and Interface Science, 274(2), pp. 637-644.

[85] Concus, P., and Finn, R., 1969, "On the Behavior of a Capillary Surface In a Wedge," Proceedings of the National Academy of Sciences, 63(2), pp. 292-299.

[86] Concus, P., and Finn, R., 1994, "Capillary Surfaces in a Wedge—Differing Contact Angles," Microgravity Science and Technology, 7(2), pp. 152-155.

[87] Concus, P., and Finn, R., 1996, "Capillary Wedges Revisited," SIAM Journal on Mathematical Analysis, 27(1), pp. 56-69.

[88] Owejan, J. P., Gagliardo, J. J., Falta, S. R., and Trabold, T. A., 2009, "Accumulation and Removal of Liquid Water in Proton Exchange Membrane Fuel Cells," Journal of The Electrochemical Society, 156(12), pp. B1475-B1483.

[89] Rath, C. D., and Kandlikar, S. G., 2011, "Effct of Channel Geometry on Two-Phase Flow Structure in Fuel Cell Gas Channels," Proceedings of the ASME 2011 9th International Conference on Nanochannels, Microchannels, and MinichannelsEdmonton, Alberta, CANADA.

[90] Rath, C. D., and Kandlikar, S. G., 2011, "Liquid Filling in a Corner with a Fibrous Wall—An Application to Two-Phase Flow in PEM Fuel Cell Gas Channels," Colloids and Surfaces A: Physicochemical and Engineering Aspects, 384(1-3), pp. 653-660.

[91] Gopalan, P., and Kandlikar, S. G., 2012, "Droplet-Sidewall Dynamic Interactions in PEMFC Gas Channels," Journal of The Electrochemical Society, 159(8), pp. F468-F475.

[92] Gopalan, P., and Kandlikar, S. G., 2013, "Effect of Channel Material on Water Droplet Dynamics in a PEMFC Gas Channel," Journal of The Electrochemical Society, 160(6), pp. F487-F495.

[93] Gopalan, P., and Kandlikar, S. G., 2012, "Effect of Channel Materials on the Behavior of Water Droplet Emerging from GDL into PEMFC Gas Channels," ECS Transactions, 50(2), pp. 503-512.

[94] Gopalan, P., and Kandlikar, S. G., 2011, "Investigation of Water Droplet Interaction with the Sidewalls of the Gas Channel in a PEM Fuel Cell in the Presence of Gas Flow," ECS Transactions, 41(1), pp. 479-488.

[95] Das, S., Waghmare, P. R., Fan, M., Gunda, N. S. K., Roy, S. S., and Mitra, S. K., 2012, "Dynamics of Liquid Droplets in an Evaporating Drop: Liquid Droplet "Coffee Stain" Effect," RSC Advances, 2(22), pp. 8390-8401.

[96] Owejan, J. P., Trabold, T. A., Jacobson, D. L., Baker, D. R., Hussey, D. S., and Arif, M., 2006, "*In Situ* investigation of Water Transport in an Operating PEM Fuel Cell Using Neutron Radiography: Part 2 – Transient Water Accumulation in an Interdigitated Cathode Flow Field," International Journal of Heat and Mass Transfer, 49(25–26), pp. 4721-4731.

[97] Satija, R., Jacobson, D. L., Arif, M., and Werner, S. A., 2004, "*In Situ* Neutron Imaging Technique for Evaluation of Water Management Systems in Operating PEM Fuel Cells," Journal of Power Sources, 129(2), pp. 238-245.

[98] Bellows, R. J., Lin, M.Y., Arif, M., Thompson, A.K., and Jacobson, D.L., 1999, "Neutron Imaging Technique for In Situ Measurement of Water Transport Gradients within Nafion in Polymer Electrolyte Fuel Cells," Journal of The Electrochemical Society, 146(3), pp. 1099-1103.

[99] Chuang, P. A., Turhan, A., Heller, A. K., Brenizer, J. S., Trabold, T. A., and Mench, M. M., 2005, "The Nature of Flooding and Drying in Polymer Electrolyte Fuel Cells," ASME Conference Proceedings, 2005(37645), pp. 31-37.

[100] Manke, I., Hartnig, C., Grunerbel, M., Lehnert, W., Kardjilov, N., Haibel, A., Hilger, A., Banhart, J., and Riesemeier, H., 2007, "Investigation of Water Evolution and Transport in Fuel Cells with High Resolution Synchrotron X-Ray Radiography," Applied Physics Letters, 90(17), pp. 174105-174103.

[101] Bazylak, A., Sinton, D., and Djilali, N., 2008, "Dynamic Water Transport and Droplet Emergence in PEMFC Gas Diffusion Layers," Journal of Power Sources, 176(1), pp. 240-246.

[102] Feindel, K. W., Bergens, S. H., and Wasylishen, R. E., 2007, "The Influence of Membrane Electrode Assembly Water Content on the Performance of a Polymer Electrolyte Membrane Fuel Cell as Investigated by 1H NMR Microscopy," Physical Chemistry Chemical Physics, 9(15), pp. 1850-1857.

[103] Tsushima, S., Nanjo, T., Nishida, K., and Hirai, S., 2006, "Investigation of the Lateral Water Distribution in a Proton Exchange Membrane in Fuel Cell Operation by 3D-MRI," ECS Transactions, 1(6), pp. 199-205.

[104] Tsushima, S., Teranishi, K., and Hirai, S., 2004, "Magnetic Resonance Imaging of the Water Distribution within a Polymer Electrolyte Membrane in Fuel Cells," Electrochemical and Solid-State Letters, 7(9), pp. A269-A272.

[105] Dunbar, Z., and Masel, R. I., 2007, "Quantitative MRI Study of Water Distribution During Operation of a PEM Fuel Cell Using Teflon® Flow Fields," Journal of Power Sources, 171(2), pp. 678-687.

[106] Litster, S., Sinton, D., and Djilali, N., 2006, "*Ex Situ* Visualization of Liquid Water Transport in PEM Fuel Cell Gas Diffusion Layers," Journal of Power Sources, 154(1), pp. 95-105.

[107] Pasaogullari, U., and Wang, C. Y., 2004, "Liquid Water Transport in Gas Diffusion Layer of Polymer Electrolyte Fuel Cells," Journal of The Electrochemical Society, 151(3), pp. A399-A406.

[108] Daino, M. M., and Kandlikar, S. G., 2009, "Evaluation of Imaging Techniques Applied to Water Management Research in PEMFCs," ASME 2009 7th International Conference on Nanochannels, Microchannels, and Minichannels, ASME, Pohang, South Korea, pp. 467-479.

[109] Kandlikar, S. G., Lu, Z., Domigan, W. E., White, A. D., and Benedict, M. W., 2009, "Measurement of Flow Maldistribution in Parallel Channels and its Application to *Ex Situ* and *In Situ* Experiments in PEMFC Water Management Studies," International Journal of Heat and Mass Transfer, 52(7–8), pp. 1741-1752.

[110] Kandlikar, S. G., Lu, Z., Lin, T. Y., Cooke, D., and Daino, M., 2009, "Uneven Gas Diffusion Layer Intrusion in Gas Channel Arrays of Proton Exchange Membrane Fuel Cell and its Effects on Flow Distribution," Journal of Power Sources, 194(1), pp. 328-337.

[111] Tuber, K., Pocza, D., and Hebling, C., 2003, "Visualization of Water Buildup in the Cathode of a Transparent PEM Fuel Cell," Journal of Power Sources, 124(2), pp. 403-414.

[112] Metz, T., Paust, N., Müller, C., Zengerle, R., and Koltay, P., 2008, "Passive Water Removal in Fuel Cells by Capillary Droplet Actuation," Sensors and Actuators A: Physical, 143(1), pp. 49-57.

[113] Ous, T., and Arcoumanis, C., 2009, "The Formation of Water Droplets in an Air-Breathing PEMFC," International Journal of Hydrogen Energy, 34(8), pp. 3476-3487.

[114] Esposito, A., Montello, A. D., Guezennec, Y. G., and Pianese, C., 2010, "Experimental Investigation of Water Droplet–Air Flow Interaction in a Non-Reacting PEM Fuel Cell Channel," Journal of Power Sources, 195(9), pp. 2691-2699.

[115] Lu, Z., White, A. D., Pelaez, J., Hardbarger, M., Domigan, W., Sergi, J. M., and Kandlikar, S. G., 2008, "Investigation of Water Transport in an *Ex Situ* Experimental Facility Modelled on an Actual DOE Automotive Target Complient Fuel Cell," ASME 2008 6th International Conference on Nanochannels, Microchannels, and Minichannels Darmstadt, Germany, pp. 1295-1303.

[116] Kandlikar, S. G., Lu, Z., Domigan, W. E., White, A. D., and Benedict, M. W., 2009, "Measurement of flow maldistribution in parallel channels and its application to ex-situ and in-situ experiments in PEMFC water management studies," International Journal of Heat and Mass Transfer, 52(7–8), pp. 1741-1752.

[117] Lu, Z., Kandlikar, S. G., Rath, C., Grimm, M., Domigan, W., White, A. D., Hardbarger, M., Owejan, J. P., and Trabold, T. A., 2009, "Water Management Studies in PEM Fuel Cells, Part II: *Ex Situ* Investigation of Flow Maldistribution, Pressure Drop and Two-Phase Flow Pattern in Gas Channels," International Journal of Hydrogen Energy, 34(8), pp. 3445-3456.

[118] Lu, Z., Daino, M. M., Rath, C., and Kandlikar, S. G., 2010, "Water Management Studies in PEM Fuel Cells, Part III: Dynamic Breakthrough and Intermittent Drainage Characteristics from GDLs with and without MPLs," International Journal of Hydrogen Energy, 35(9), pp. 4222-4233.

[119] Lu, Z., Rath, C., Zhang, G., and Kandlikar, S. G., 2011, "Water Management Studies in PEM Fuel Cells, Part IV: Effects of Channel Surface Wettability, Geometry and Orientation on the Two-Phase Flow in Parallel Gas Channels," International Journal of Hydrogen Energy, 36(16), pp. 9864-9875.

[120] Zhang, F. Y., Yang, X. G., and Wang, C. Y., 2006, "Liquid Water Removal from a Polymer Electrolyte Fuel Cell," Journal of The Electrochemical Society, 153(2), pp. A225-A232.

[121] Wang, C.-Y., 2004, "Fundamental Models for Fuel Cell Engineering," Chemical Reviews, 104(10), pp. 4727-4766.

[122] Gostick, J. T., Fowler, M. W., Ioannidis, M. A., Pritzker, M. D., Volfkovich, Y. M., and Sakars, A., 2006, "Capillary Pressure and Hydrophilic Porosity in Gas Diffusion Layers for Polymer Electrolyte Fuel Cells," Journal of Power Sources, 156(2), pp. 375-387.

[123] Wang, K., Lu, Y. C., Xu, J. H., and Luo, G. S., 2009, "Determination of Dynamic Interfacial Tension and its Effect on Droplet Formation in the T-Shaped Microdispersion Process," Langmuir, 25(4), pp. 2153-2158.

[124] Cho, S. C., Wang, Y., and Chen, K. S., 2012, "Droplet Dnamics in a Polymer Electrolyte Fuel Cell Gas Flow Channel: Forces, Deformation and Detachment. II: Comparisons of Analytical Solution with Numerical and Experimental Results," Journal of Power Sources, 210, pp. 191-197.

[125] Cho, S. C., Wang, Y., and Chen, K. S., 2012, "Droplet Dynamics in a Polymer Electrolyte Fuel Cell Gas Flow Channel: Forces, Deformation, and Detachment. I: Theoretical and Numerical Analyses," Journal of Power Sources, 206, pp. 119-128.

[126] Nam, J. H., and Kaviany, M., 2003, "Effective Diffusivity and Water-Saturation Distribution in Single- and Two-Layer PEMFC Diffusion Medium," International Journal of Heat and Mass Transfer, 46(24), pp. 4595-4611.

[127] Weber, A. Z., and Newman, J., 2004, "Modeling Transport in Polymer-Electrolyte Fuel Cells," Chemical Reviews, 104(10), pp. 4679-4726.

[128] Chen, K. S., Hickner, M. A., and Noble, D. R., 2005, "Simplified Models for Predicting the Onset of Liquid Water Droplet Instability at the Gas Diffusion Layer/Gas Flow Channel Interface," International Journal of Energy Research, 29(12), pp. 1113-1132.

[129] Golpaygan, A., and Ashgriz, N., 2005, "Effects of Oxidant Fluid Properties on the Mobility of Water Droplets in the Channels of PEM Fuel Cell," International Journal of Energy Research, 29(12), pp. 1027-1040.

[130] Theodorakakos, A., Ous, T., Gavaises, M., Nouri, J. M., Nikolopoulos, N., and Yanagihara, H., 2006, "Dynamics of Water Droplets Detached from Porous Surfaces of Relevance to PEM Fuel Cells," Journal of Colloid and Interface Science, 300(2), pp. 673-687.

[131] Kumbur, E. C., Sharp, K. V., and Mench, M. M., 2006, "Liquid Droplet Behavior and Instability in a Polymer Electrolyte Fuel Cell Flow Channel," Journal of Power Sources, 161(1), pp. 333-345.

[132] Das, P. K., Grippin, A., Kwong, A., and Weber, A. Z., 2012, "Liquid-Water-Droplet Adhesion-Force Measurements on Fresh and Aged Fuel-Cell Gas-Diffusion Layers," Journal of The Electrochemical Society, 159(5), pp. B489-B496.

[133] Owejan, J. P., Trabold, T. A., Jacobson, D. L., Arif, M., and Kandlikar, S. G., 2007, "Effects of Flow Field and Diffusion Layer Properties on Water Accumulation in a PEM Fuel Cell," International Journal of Hydrogen Energy, 32(17), pp. 4489-4502.

[134] Kimball, E., Whitaker, T., Kevrekidis, Y. G., and Benziger, J. B., 2008, "Drops, Slugs, and Flooding in Polymer Electrolyte Membrane Fuel Cells," AIChE Journal, 54(5), pp. 1313-1332.

[135] Lee, J., Hinebaugh, J., and Bazylak, A., 2013, "Visualizing Liquid Water in PEM Fuel Cells Using X-ray Based Radiography in through-and In-Planes," ECS MeetingToronto, ON, p. 125.

[136] Allen, J. S., Son, S. Y., and Collicott, S. H., 2010, "Proton Exchange Membrane Fuel Cell (PEMFC) Flow-Field Design for Improved Water Management," Handbook of Fuel Cells, John Wiley & Sons, Ltd.

[137] Kimball, E. E., Benziger, J. B., and Kevrekidis, Y. G., 2010, "Effects of GDL Structure with an Efficient Approach to the Management of Liquid Water in PEM Fuel Cells," Fuel Cells, 10(4), pp. 530-544.

[138] Yi, Y., Zheng-kai, T., Zhi-gang, Z., and Mu, P., 2012, "Gravity Effect on the Performance of PEM Fuel Cell Stack with Different Gas Manifold Positions," International Journal of Energy Research, 36(7), pp. 845-855.

[139] Chen, S., and Wu, Y., 2010, "Gravity Effect on Water Discharged in PEM Fuel Cell Cathode," International Journal of Hydrogen Energy, 35(7), pp. 2888-2893.

[140] Cheah, M. J., Kevrekidis, I. G., and Benziger, J. B., 2013, "Water Slug Formation and Motion in Gas Flow Channels: The Effects of Geometry, Surface Wettability, And Gravity," Langmuir, 29(31), pp. 9918-9934.

[141] Hao, L., and Cheng, P., 2010, "An Analytical Model for Micro-Droplet Steady Movement on the Hydrophobic Wall of a Micro-Channel," International Journal of Heat and Mass Transfer, 53(5–6), pp. 1243-1246.

[142] Hao, L., and Cheng, P., 2009, "Lattice Boltzmann Simulations of Liquid Droplet Dynamic Behavior on a Hydrophobic Surface of a Gas Flow Channel," Journal of Power Sources, 190(2), pp. 435-446.

[143] Ha, T., Kim, B., Kim, H.-S., and Min, K., 2008, "Investigation on the Liquid Water Droplet Instability in a Simulated Flow Channel of PEM Fuel Cell," J Mech Sci Technol, 22(5), pp. 1030-1036.

[144] De Luca, G., Di Maio, F. P., Di Renzo, A., and Drioli, E., 2008, "Droplet Detachment in Cross-Flow Membrane Emulsification: Comparison Among Torque and Force Based Models," Chemical Engineering and Processing: Process Intensification, 47(7), pp. 1150-1158.

[145] Yang, J.-T., Yang, Z.-H., Chen, C.-Y., and Yao, D.-J., 2008, "Conversion of Surface Energy and Manipulation of a Single Droplet across Micropatterned Surfaces," Langmuir, 24(17), pp. 9889-9897.

[146] He, G., Ming, P., Zhao, Z., Abudula, A., and Xiao, Y., 2007, "A Two-Fluid Model for Two-Phase Flow in PEMFCs," Journal of Power Sources, 163(2), pp. 864-873.

[147] Spernjak, D., Advani, S., and Prasad, A. K., 2006, "Experimental Investigation of Liquid Water Formation and Transport in a Transparent Single-Serpentine PEM Fuel Cell," ASME Conference Proceedings, ASME, pp. 453-461.

[148] Zhu, X., Sui, P. C., and Djilali, N., 2008, "Three-Dimensional Numerical Simulations of Water Droplet Dynamics in a PEMFC Gas Channel," Journal of Power Sources, 181(1), pp. 101-115.

[149] Polverino, P., Esposito, A., and Pianese, C., 2013, "Experimental Validation of a Lumped Model of Single Droplet Deformation, Oscillation and Detachment on the GDL Surface of a PEM Fuel Cell," International Journal of Hydrogen Energy, 38(21), pp. 8934-8953.

[150] Wang, Z. H., Wang, C. Y., and Chen, K. S., 2001, "Two-phase Flow and Transport in the Air Cathode of Proton Exchange Membrane Fuel Cells," Journal of Power Sources, 94(1), pp. 40-50.

[151] Sergi, J. M., Lu, Z., and Kandlikar, S. G., "*In Situ* Characterization of Two-Phase Flow in the Cathode Channels of an Operating PEM Fuel Cell with Visual Access," Proc. Proceeding of the seventh international conference on nanochannels, microchannels, and minichannels, pp. 303-311.

[152] Cai, Y. H., Hu, J., Ma, H. P., Yi, B. L., and Zhang, H. M., 2006, "Effects of Hydrophilic/Hydrophobic Properties on the Water Behavior in the Microchannels of a Proton Exchange Membrane Fuel Cell," Journal of Power Sources, 161(2), pp. 843-848.

[153] Quan, P., and Lai, M.-C., 2007, "Numerical Study of Water Management in the Air Flow Channel of a PEM Fuel Cell Cathode," Journal of Power Sources, 164(1), pp. 222-237.

[154] Zhu, X., Liao, Q., Sui, P. C., and Djilali, N., 2010, "Numerical Investigation of Water Droplet Dynamics in a Low-Temperature Fuel Cell Microchannel: Effect of Channel Geometry," Journal of Power Sources, 195(3), pp. 801-812.

[155] Akhtar, N., Qureshi, A., Scholta, J., Hartnig, C., Messerschmidt, M., and Lehnert, W., 2009, "Investigation of Water Droplet Kinetics and Optimization of Channel Geometry for PEM Fuel Cell Cathodes," International Journal of Hydrogen Energy, 34(7), pp. 3104-3111.

[156] Hwang, C.-C., Ho, J.-R., and Lee, S.-C., 1999, "Molecular Dynamics of a Liquid Drop Spreading in a Corner Formed by Two Planar Substrates," Physical Review E, 60(5), pp. 5693-5698.

[157] Patankar, N. A., 2003, "On the Modeling of Hydrophobic Contact Angles on Rough Surfaces," Langmuir, 19(4), pp. 1249-1253.

[158] Kalinin, Y. V., Berejnov, V., and Thorne, R. E., 2009, "Contact Line Pinning by Microfabricated Patterns: Effects of Microscale Topography," Langmuir, 25(9), pp. 5391-5397.

[159] Gopalan, P., and Kandlikar, S. G., "Contact Line Characteristics of Liquid-Gas Interfaces Over Confined/Structured Surfaces," Proc. Proceedings of the 3rd European Conference on Microfluidics - Microfluidics 2012.

[160] Gopalan, P., and Kandlikar, S. G., 2013, "Contact Line Characteristics of Liquid-Gas Interfaces Over Confined/Structured Surfaces," Microfluidics and Nanofluidics, p. In Press.

[161] Gopalan, P., and Kandlikar, S. G., 2014, "Modeling Dynamic Interaction Between an Emerging Water Droplet and the Sidewall of a Trapezoidal Channel," Colloids and Surfaces A: Physicochemical and Engineering Aspects, 441, pp. 262-274.

[162] Voinov, O. V., 2000, "Wetting Line Dynamics in the Process of Drop Spreading," Journal of Colloid and Interface Science, 226(1), pp. 22-28.

[163] de Gennes, P. G., 1985, "Wetting: Statics and Dynamics," Reviews of Modern Physics, 57(3), pp. 827-863.

[164] Bonn, D., Eggers, J., Indekeu, J., Meunier, J., and Rolley, E., 2009, "Wetting and Spreading," Reviews of Modern Physics, 81(2), pp. 739-805.

[165] Kalin, M., and Polajnar, M., 2013, "The Correlation Between the Surface Energy, the Contact Angle and the Spreading Parameter, and their Relevance for the Wetting Behaviour of DLC with Lubricating Oils," Tribology International, 66(0), pp. 225-233.

[166] Cazabat, A. M., and Stuart, M. A. C., 1989, "The Dynamics of Wetting," Physicochemical Hydrodynamics NATO ASI Series, 174, pp. 709-720.

[167] Cazabat, A.-M., 1987, "How Does a Droplet Spread?," Contemporary Physics, 28(4), pp. 347-364.

[168] Ball, P., 1989, "Spread it About," Nature, 338, pp. 624-625.

[169] Leger, L., and Joanny, J. F., 1992, "Liquid Spreading," Reports on Progress in Physics, 55(4), p. 431.

[170] Forcada, M. L., and Mate, C. M., 1993, "Molecular Layering During Evaporation of Ultrathin Liquid Films," Nature, 363, pp. 527-529.

[171] Gopalan, P., and Kandlikar, S. G., 2014, "Effect of Channel Materials and Trapezoidal Corner Angles on Emerging Droplet Behavior in Proton Exchange Membrane Fuel Cell Gas Channels," Journal of Power Sources, 248, pp. 230-238.

[172] Clift, R., Grace, J., and Weber, M., 1978, "Bubbles, Drops and Particles Academic," New York, p. 346.

[173] Banerjee, R., and Kandlikar, S. G., 2014, "Liquid Water Quantification in the Cathode Side Gas Channels of a Proton Exchange Membrane Fuel Cell through Two-Phase Flow Visualization," Journal of Power Sources, 247, pp. 9-19.

[174] Pérez-Page, M., and Pérez-Herranz, V., 2011, "Effect of the Operation and Humidification Temperatures on the Performance of a Pem Fuel Cell Stack on Dead-End Mode," International Journal of Electrochemical Science, 6, pp. 492-505.

[175] Murthy, M., Esayian, M., Lee, W.-k., and Van Zee, J. W., 2003, "The Effect of Temperature and Pressure on the Performance of a PEMFC Exposed to Transient CO Concentrations," Journal of Electrochemical Society, 150(1), pp. A-29-A34.

[176] Belkhiri, Z., Zeroual, M., Ben Moussa, H., and Zitouni, B., 2011, "Effect of Temperature and Water Content on the Performance of PEM Fuel Cell," Revue des Energies Renouvelables, 14(1), pp. 121-130.

[177] Kim, S., and Hong, I., 2008, "Effects of Humidity and Temperature on a Proton Exchange Membrane Fuel Cell (PEMFC) Stack," Journal of Industrial and Engineering Chemistry, 14(3), pp. 357-364.